

Experimental and Theoretical Analysis of Closed-Flow Column Experiments

An Alternative Approach for the Investigation of
Solute Transport on the Continuum Scale

Dissertation

zur Erlangung des akademischen Grades doctor rerum naturalium
(Dr. rer. nat.)

vorgelegt dem Rat der Chemisch-Geowissenschaftlichen Fakultät der
Friedrich-Schiller-Universität Jena

von Thomas Ritschel

geboren am 02.08.1984 in Neuhaus am Rennweg

Gutachter:

1. Prof. Dr. Kai Uwe Totsche, Universität Jena
2. Prof. Dr. Bernd Huwe, Universität Bayreuth

Tag der Verteidigung: 08.08.2016

Abstract

Research of solute transport fundamentally contributes to our understanding of soil functions as most processes in soils are dynamically driven and related to the transient conditions produced by the transport of solutes. For this reason, especially the transport of contaminants is frequently studied with laboratory scale column outflow experiments in an open-flow mode. This thesis presents a complementary approach of conducting saturated column experiments that is characterized by the recirculation of the column effluent into the inflow via a mixing vessel and is therefore referred to as closed-flow mode column experiment. Depending on the ratio of the volume of the mixing vessel and the water-filled pore space, a damped oscillating concentration emerges in the effluent and in the mixing vessel. Oscillation frequency, damping and amplitude are thereby governed by the properties of the porous medium and the target substance. These characteristics permit the analysis of transport processes in soils in a similar fashion as known for classical open-flow column experiments. However, the experimental design maintains feedbacks of liquid solid interactions by providing a closed loop. In this way, solute and porous medium can equilibrate with respect to all physicochemical parameters as known for completely mixed batch reactor experiments, also permitting a convenient consideration of mass balances. To unravel the information provided by experiments run in closed-flow mode, the features emerging in the breakthrough curve are presented in dependence of decisive boundary conditions and are thoroughly discussed. It was shown by column experiments with quartz sand that the appearance of oscillations can be controlled very precisely by using different mixing vessel solute volumes. The breakthrough data obtained within these experiments was then used to validate a numerical model that was derived by coupling the numerical solution of the advection dispersion equation with the model describing the mixing vessel in a loop. This model was used for a comprehensive sensitivity analysis to illustrate the response of the breakthrough curve to changes in the dispersion and the parameters describing adsorption with respect to strength, rate and nonlinearity. Each process thereby produced unique responses that confirm the high information content of closed-flow breakthrough data, which has shown to intrinsically contain information on the water content and the pumping rate as well. To assess the performance of the experimental design with respect to the inverse determination of transport parameters from closed-flow breakthrough data, an extensive numerical analysis was conducted. Under optimal conditions, a massive decrease in parameter uncertainty was revealed for closed-flow mode experiments, which renders the approach highly relevant for practical applications. In addition, theoretical considerations on the mixing process and the mass balances implied further evaluation methods, e.g. the comparison to a damped harmonic oscillator and the Fourier transform, that are presented in order to maximize the information retrieval from breakthrough data.

Conclusively, the presented design combines advantages from different classical approaches and therefore complements the set of experimental setups by providing indicative and sensitive data on transport processes under packing and flow conditions comparable to natural soils.

Kurzzusammenfassung

Die Erforschung von Stofftransport trägt fundamental dazu bei, die den Bodenfunktionen zugrundeliegenden Prozesse zu verstehen, da diese dynamisch von den durch Transport erzeugten transienten Bedingungen abhängig sind. Daher wird insbesondere der Transport von Kontaminanten häufig in laborskaligen Säulenexperimenten im Durchfluss untersucht. In dieser Dissertation wird ein komplementärer Ansatz für die Durchführung von gesättigten Säulenexperimenten vorgestellt, welcher sich dadurch auszeichnet, dass die Effluentlösung zurück in das Vorratsgefäß für den Influenten geführt und somit ein geschlossener Kreislauf erzeugt wird. Abhängig vom Verhältnis der Volumina von Vorratsgefäß und Porenraum entsteht eine gedämpfte Oszillation der Konzentration im Effluenten und dem Vorratsgefäß. Die Frequenz, Dämpfung und Amplitude dieser Schwingung werden durch die Eigenschaften des Fließ- und Transportregimes bestimmt. Auf diese Weise lassen sich analog zu bekannten experimentellen Ansätzen Rückschlüsse auf Transportprozesse ziehen. Zudem bleiben im Kreislauf Rückkopplungen des Systems auf den Transport erhalten. Das bedeutet, dass sich zwischen Lösung und porösem Medium in Bezug auf alle hydrochemischen Parameter ein Gleichgewicht einstellt. Diese Situation ist vergleichbar mit Schüttelexperimenten und erlaubt damit eine einfache Betrachtung von Massenbilanzen. Um das typische Verhalten von Kreislaufexperimenten zu durchleuchten, wurden in dieser Arbeit die Merkmale der Durchbruchkurve in Abhängigkeit entscheidender Randbedingungen vorgestellt. Dabei hat sich durch Experimente mit Quarzsand gezeigt, dass sich das Auftreten von Oszillationen durch die Auswahl eines passenden Vorratsgefäßvolumens präzise steuern lässt. Die dabei erhaltenen Durchbruchkurven wurden dann verwendet, um ein numerisches Modell zu validieren, welches auf der Kopplung der Stofftransportgleichung mit einem Modell für den zeitlichen Verlauf der Konzentration im Vorratsgefäß beruht. Mithilfe dieses Modells wurde anschließend eine umfassende Sensitivitätsanalyse durchgeführt, welche das Verhalten der Durchbruchkurve bei Änderungen von sowohl Dispersion als auch von Stärke, Kinetik und Nichtlinearität der Adsorption zeigt. Jeder Transportprozess erzeugt dabei ein einzigartiges Signal in der Durchbruchkurve, welche zudem zur Bestimmung des Wassergehaltes sowie zur Bestimmung der Pumprate genutzt werden kann. Um die Eignung des experimentellen Ansatzes bei der inversen Modellierung von Transportparametern zu untersuchen, wurde eine Reihe systematischer Sensitivitätsanalysen durchgeführt. Diese zeigten im Vergleich zu klassischen Durchbruchexperimenten eine massive Verringerung der Parameterunsicherheit unter günstigen Rahmenbedingungen und zeichnen damit das Kreislaufexperiment als höchst relevant für den praktischen Einsatz aus. Zusätzlich wurden weitere theoretische Ansätze wie der Vergleich mit dem gedämpften harmonischen Oszillator und die Fourier-Transformation zur Auswertung der Durchbruchkurve untersucht, um deren Informationsgehalt maximal herauszuarbeiten.

Zusammenfassend präsentiert sich das Kreislaufexperiment als Kombination von Vorteilen klassischer Durchbruchs- und Schüttelexperimente. Es erweitert somit den Fundus an Transportexperimenten um ein vielversprechendes Design, das robuste Informationen über den Stofftransport unter ungestörten Lagerungsbedingungen liefert.

Contents

Abstract	I
Kurzzusammenfassung	II
Contents	III
List of Figures	VII
List of Tables	IX
Nomenclature	XI
Symbols	XIII
1 Introduction	1
1.1 Motivation	1
1.2 Classical Column Experiments	3
1.2.1 Description of the Experimental Design	3
1.2.2 Porous Media used in Column Experiments	5
1.2.3 Tracers in Column Experiments	6
1.3 Limitations of Classical Approaches	8
1.4 The Closed-Flow Design	10
1.4.1 Concept	10
1.4.2 Emergence of Concentration Oscillations	11
1.5 Main Hypotheses	14
2 Theoretical Considerations	15
2.1 Transport Equation	15
2.1.1 Fluxes and Continuity Equation	15
2.1.2 Chemical Interactions	16
2.1.3 The Retardation Coefficient	18
2.1.4 Immobile Pore Water	19
2.1.5 Two-Site Two-Region Model	20

2.1.6	Comparison to Interaction Kinetics in Completely Mixed Batch Reactors	21
2.2	Dimensionless Parameters	22
2.3	Evaluation of Mass Balances	24
2.3.1	General Mass Balance in Column Experiments	24
2.3.2	The Volumetric Dilution Factor	24
2.3.3	Intrinsic Determination of the Water Content	26
2.3.4	Intrinsic Characterization of Sorption	26
2.3.5	Hypotheses Emerging from the Mass Balance	27
2.4	The Mixing Process in the Mixing Vessel	29
2.4.1	Derivation of the Constitutive Equation	29
2.4.2	Approximations for Special Cases	30
2.4.3	Hypotheses Emerging from the Mixing Process	34
2.5	Comparison to a Damped Harmonic Oscillator	35
2.5.1	Conceptual Approach	35
2.5.2	Hypotheses Emerging from the Harmonic Oscillator	37
2.6	Evaluation of Measured BTCs	38
2.6.1	Concept of Transfer Functions	38
2.6.2	Fitting of Models to Measurements	41
2.6.3	Shape Measures of the Breakthrough Curve	46
2.6.4	Fourier Transform	47
2.6.5	Hypotheses Emerging from the BTC analysis	48
3	Material and Methods	49
3.1	Experimental Procedures	49
3.1.1	Columns and Substrate	49
3.1.2	Conservative Tracer Experiments	52
3.1.3	Reactive Tracer Experiments	53
3.2	Numerical Aspects	54
3.2.1	Explicit Solution	54
3.2.2	Implicit Solution	55
3.2.3	Numerical Implementation	56
3.3	Software Development	59
3.3.1	Design Paradigms and Features	59
3.3.2	Model verification	60
3.3.3	Illustration of Sensitivity Analyses	61

4	Results and Discussion	63
4.1	Experiment A: Different Mixing Vessel Volumes	63
4.1.1	Effect on the Breakthrough Behavior	64
4.1.2	Determination of the Water-Filled Pore Space	65
4.1.3	Determination of the Breakthrough of the Center of Mass	67
4.2	Experiment B: Different Flow Velocities	69
4.3	Model Validation for Closed-Flow Experiments	72
4.4	Experiment C: Reactive Breakthrough	74
4.5	Sensitivity Analyses	77
4.5.1	Volumetric Dilution Factor	77
4.5.2	Dispersion	79
4.5.3	Linear Liquid Solid Interaction	85
4.5.4	Nonlinear Liquid Solid Interaction	90
4.5.5	Damköhler Number	91
4.5.6	Equifinality of Dispersion and Kinetic Interaction	93
4.6	Comparison to a Damped Harmonic Oscillator	98
4.6.1	Application to Experimental Results	98
4.6.2	Application to Numerical Results	98
4.7	Transfer Functions	101
4.8	Fourier Transform	102
5	Final Assessment of Hypotheses	105
5.1	Minor Hypotheses	105
5.1.1	Hypotheses Emerging from the Mass Balance	105
5.1.2	Hypotheses Emerging from the Mixing Process	106
5.1.3	Hypotheses Emerging from the Harmonic Oscillator	108
5.1.4	Hypotheses Emerging from the BTC analysis	109
5.2	Main Hypotheses	111
6	Outlook and Implications	115
6.1	Application to Unsaturated Experiments	116
7	Conclusions	117
	References	119
	Acknowledgment	133
	Tabellarischer Lebenslauf	135
	Selbstständigkeitserklärung	137

List of Figures

1.1	Schematic setup of a laboratory scale open-flow column experiment with saturated flow.	4
1.2	Schematic setup of a laboratory scale open-flow column experiment with unsaturated flow.	5
1.3	Schematic setup of a laboratory scale closed-flow column experiment.	11
1.4	BTC of a conservative tracer measured in the effluent of a closed-flow experiment	12
2.1	Scheme of the derivation of the analytical description of the first oscillation maximum of the BTC in the mixing vessel at $R = 1$ and $k = 2$	33
3.1	SEM images of artificial soil material	50
4.1	BTCs measured in the mixing vessel of a closed-flow setup with $V_m = 100$ mL, $V_m = 30$ mL and $V_m = 20$ mL (a) and backward BTCs measured in the mixing vessel of a closed-flow setup with $V_m = 30$ mL and $V_m = 20$ mL (b).	65
4.2	Surface of the objective function with respect to changes in the water content and the pumping rate around the optimal value of $\theta = 0.5$ and $Q = 0.02$ mL min ⁻¹ at $d_v = 0.5$ in case of closed-flow experiments (a, b) and open-flow experiments (c).	66
4.3	Illustration of the model used for the reconstruction of the BCM at $V_{mix} = 30$ mL and at $V_{mix} = 30$ mL (b).	67
4.4	Forward and backward BTCs obtained at two different pumping rates with the same mixing vessel volume of 20 mL.	70
4.5	Comparison of the model for exponential dilution (lines) and measured BTCs (dotted) obtained at different pumping rates and mixing vessel volumes for forward (a) and backward (b) breakthroughs.	70
4.6	Simulated BTCs using fitted dispersion in comparison to measurements.	73
4.7	BTCs measured in the mixing vessel with $V_{mix} = 30$ mL using NaCl and vanillic acid as tracer for column I (a) and column II (b), model simulations shown as dashed line.	75

4.8	Simulated BTCs at different d_v at $Pe = 100$ observed in the mixing vessel (a) and the effluent (b).	78
4.9	Simulated solute profiles along the column at d_v from 0.1 to 0.8 after the exchange of 0.7 pv (a), and the development of the solute profile at $d_v = 0.5$ at successive time steps (b).	78
4.10	Modeled closed-flow BTCs in effluent (a) and mixing vessel (b) at $d_v = 0.2$ with Pe numbers from 1 to 1000.	79
4.11	Surface of the objective function with respect to changes in the Pe number around the optimal value of $Pe = 10$ for d_v values from 0.001 to 1.	81
4.12	Surface of the objective function with respect to changes in the Pe number around the optimal value of $Pe = 100$ for d_v values in the interval [0.001,1].	82
4.13	Surface of the objective function with respect to changes in the Pe number around the optimal value of $Pe = 1000$ for d_v values from 0.001 to 1.	83
4.14	Simulated BTCs at different different R (a) and retardation reconstructed from the first oscillation maximum of modeled BTCs using retardations from 1 to 3 at different Pe numbers (b).	86
4.15	Surface of the objective function with respect to changes in R around the optimal value of $R = 2.0$ for d_v values in the interval [0.001,1].	88
4.16	Surface of the objective function with respect to changes in R around the optimal value of $R = 10.0$ for d_v values in the interval [0.001,1].	89
4.17	Simulated BTCs for varying degree of nonlinearity represented by the Freundlich exponent n_f for measurements in the effluent (a) and measurements in the mixing vessel (b).	90
4.18	Simulated BTCs at different Da numbers (a) and BTCs at Da numbers from 0.01 to 1 compared to expected kinetics in completely mixed batch reactor experiment (b).	92
4.19	Surface of the objective function with respect to changes in the Da number and the Pe number around the optimal value of $Pe = 100$ at $d_v = 0.1$	96
4.20	Surface of the objective function with respect to changes in the Da number and the Pe number around the optimal value of $Pe = 100$ at $d_v = 0.7$	97
4.21	Reconstruction of the effluent BTC of a typical closed-flow experiment using the concept of a harmonic oscillator.	99
4.22	Reconstruction of the effluent BTC of simulated closed-flow experiments using the concept of a harmonic oscillator.	100
4.23	Fourier transform (right column) of BTCs (left column) at $d_v = 0.7$ (first row), $d_v = 0.3$ (second, fourth and fifth row) and $d_v = 0.1$ (third row), comparing conservative (first, second and third row) with reactive transport at $R = 1.5$ (fourth row) and $R = 2$ (fifth row).	103

List of Tables

3.1	Composition of substrates used for the column experiments	49
3.2	Grain size distribution of quartz sand Haltern H33 (manufacturer's specifications)	50
3.3	Grain size distribution of quartz silt Millisil W11 after wet sieving	51
4.1	Experimental boundary conditions for the experiment with different mixing vessel volumes and water volumes reconstructed from BTC data.	64
4.2	Reconstruction of retardation from the first oscillation maximum.	68
4.3	Reconstruction of the pumping rate from the initial exponential BTC.	69
4.4	Parameters obtained from the inverse modeling of BTCs at different mixing vessel volumes.	72
4.5	Experimental parameters and values obtained from the inverse modeling of BTCs (marked with an asterisk) during the experiment with vanillic acid.	74
4.6	Fitted Pe number at $Pe = 1$, $Pe = 10$, $Pe = 100$ and $Pe = 1000$ and fitted R at $R = 2.0$ and $R = 10$ with 0.95-confidence interval from noisy artificial data in open-flow effluent mode, closed-flow effluent mode and closed-flow mixing vessel mode at $d_v = 0.1$	84
4.7	Fitted R at $R = 2.0$ and $R = 10$ with 0.95-confidence interval from noisy artificial data in open-flow effluent mode, closed-flow effluent mode and closed-flow mixing vessel mode at $d_v = 0.1$	86
4.8	Reconstructed retardation for simulated breakthroughs with different k and R	87
4.9	Fitted Pe numbers and Da numbers with 0.95-confidence interval from noisy artificial data at $Da = 1$, $Da = 10$, $Da = 100$ and $Pe = 100$ in open-flow effluent, closed-flow effluent and closed-flow mixing vessel mode at $d_v = 0.1$	94
4.10	Fitted Pe numbers and Da numbers with 0.95-confidence interval from noisy artificial data at $Da = 1$, $Da = 10$, $Da = 100$ and $Pe = 100$ in open-flow effluent, closed-flow effluent and closed-flow mixing vessel mode at $d_v = 0.7$	94
4.11	Experimental boundary conditions used for measurement of the effluent BTC.	98
4.12	Parameters used for reconstruction of BTC data with the analytical solution of a harmonic oscillator.	99
4.13	Parameters used for reconstruction of numerical BTC data at different d_v and different Pe numbers with the analytical solution of a harmonic oscillator.	100

5.1	Overview of BTC features and related transport processes.	111
7.1	Overview of suggested experimental boundary conditions to obtain an indicative closed-flow BTC.	118

Nomenclature

Notation	Description	Page List
ADE	advection dispersion equation	15, 16, 19, 23, 41, 54–57, 60, 63, 77, 98, 118
API	application programming interface	60
ASQz	non-reactive Artificial Soil	49, 63, 66
ASQzGt	reactive Artificial Soil	49, 51, 74
BCM	breakthrough of the center of mass	13, 22, 31, 47, 67, 70, 87, 107
BET	Brunauer-Emmett-Teller [method]	49, 51
BTC	breakthrough curve	7, 11–14, 19, 20, 22, 25, 28, 30–35, 37–41, 46–48, 60, 61, 63–75, 77–80, 84–87, 90–95, 98–103, 105–113, 115–118
CDF	cumulative distribution function	40, 41, 46, 47, 79
DOC	dissolved organic matter	18
GUI	graphical user interface	59, 60
PDE	partial differential equation	15, 54, 55, 57, 77, 101
PDF	probability density function	38, 41, 45–48, 79, 101, 109
PMMA	polymethylmethacrylat	49
PZC	point of zero charge, i.e. the pH value at which the net charge of a surface is zero	9, 50–52
Qz	Roth Quartz	49, 98
SEM	scanning electron microscopy	49–51, 133
XRD	X-Ray diffraction	49, 51

Symbols

Units of non-constant symbols are represented in base dimensions: length L, mass M, time T and temperature Θ . In general, small letters denote scalars, bold letters denote vectors and bold capital letters denote matrices. Superscripts define a temporal relationship and subscripts hold a spatial or descriptive definition, latter given non-italic.

Symbol	Description	Symbol	Page List
A	base area of the column	L^2	22, 24
a	acceleration	LT^{-2}	35
C	viscous damping coefficient	MT^{-1}	36
c	concentration $c = \beta c_m + \tilde{\beta} c_{im}$	ML^{-3}	15–19, 21, 24, 32, 36, 37, 56–58, 90, 91
c^{end}	final concentration	ML^{-3}	25–27, 37
c^{init}	initial concentration	ML^{-3}	21, 25–27
c_1	concentration in the mixing vessel in the beginning of the experiment	ML^{-3}	32
c_2	second phase of the breakthrough in the mixing vessel	ML^{-3}	32, 34
c_e	concentration in the effluent	ML^{-3}	29, 30, 32, 38
c_e^i	concentration in the effluent at timestep i	ML^{-3}	29, 55
c_e^{i+1}	concentration in the effluent at timestep succeeding i	ML^{-3}	55, 56, 58
c_e^{init}	initial concentration in the effluent	ML^{-3}	30
c_f	flux concentration	ML^{-3}	41
c_{im}	concentration in the immobile region	ML^{-3}	20, 21
c_{in}	concentration in the influent	ML^{-3}	38, 41
c_m	concentration in the mobile region	ML^{-3}	20, 21
c_{mix}	concentration in the mixing vessel	ML^{-3}	29, 30, 32
c_{mix}^i	concentration in the mixing vessel at timestep i	ML^{-3}	29, 55, 56, 58
c_{mix}^{i+1}	concentration in the mixing vessel at timestep succeeding i	ML^{-3}	29, 55–58
c_{mix}^{init}	initial concentration in the mixing vessel	ML^{-3}	11, 30, 32–34
c_n	concentration in the n-th phase of the breakthrough	ML^{-3}	32–34
c_r	resident concentration	ML^{-3}	41
Δc_{mix}	difference in concentration in the mixing vessel	ML^{-3}	29
D	apparent dispersion coefficient $D = D_m + D_h$	$L^2 T^{-1}$	16, 19, 21, 22, 41, 56–58, 74, 75, 98
D_h	hydromechanic dispersion coefficient	$L^2 T^{-1}$	16, 22
D_m	molecular diffusion coefficient	$L^2 T^{-1}$	16

Symbol	Description	Symbol	Page List
Da	Damköhler number, relation of mass transfer and residence time	T	23, 43, 74, 76, 91–97, 112, 113
∂_t	partial derivative with respect to time $\partial_t = \frac{\partial}{\partial t}$		15–17, 19–21, 29, 30, 56
$\partial_{t_{pv}}$	partial derivative with respect to exchanged pore volume $\partial_{t_{pv}} = \frac{\partial}{\partial t_{pv}}$		32, 34
∂_x	partial derivative with respect to space $\partial_x = \frac{\partial}{\partial x}$		15, 16, 19, 21, 41, 56, 57
d	total differential operator		24, 30, 38, 40, 41, 46, 47
d_t	total differential operator with respect to time $d_t = \frac{d}{dt}$		35, 36, 40
d	observed relative dilution	–	27
d_v	volumetric dilution factor	–	24–27, 61, 64–67, 77–103, 106, 111, 112, 117, 118
E	energy	$ML^2 T^{-2}$	45
F	force	MLT^{-2}	35, 36, 47
f	fraction of the bulk density related to equilibrium sorption	–	17, 74
F_X	cumulative distribution function of random variable X		46
f_X	probability density function of random variable X		46, 47
\tilde{f}_{pm}	impulse response function of the porous medium		38, 39, 41
\tilde{f}	fraction of the bulk density related to non-equilibrium sorption $\tilde{f} = 1 - f$	–	17
\mathbf{g}	gradient vector		43, 44
H	Heaviside step function		40
\mathbf{H}	Hessian matrix		43
\mathbf{I}	identity matrix		44
\Im	imaginary part of a complex number		48
i	running variable for temporal discretization		54, 55
i	imaginary unit		47, 48
J	total solute flux $J = J_a + J_m + J_h = J_a + J_d$	$ML^{-2} T^{-1}$	15, 16
J_a	solute flux due to advection	$ML^{-2} T^{-1}$	15, 16
J_d	solute flux due to apparent dispersion $J_d = J_m + J_h$	$ML^{-2} T^{-1}$	16
J_h	solute flux due to hydrodynamic dispersion	$ML^{-2} T^{-1}$	16
J_m	solute flux due to molecular diffusion	$ML^{-2} T^{-1}$	16

Symbol	Description	Symbol	Page List
J	Jacobian matrix		43, 44
<i>j</i>	running variable for spatial discretization		57
K_d	linear sorption/distribution coefficient	$L^3 M^{-1}$	17–19, 21, 27, 74, 75, 85
K_f	Freundlich sorption coefficient	$L^3 M^{-1}$	18, 90
K_l	Langmuir sorption coefficient	$L^3 M^{-1}$	18
<i>k</i>	relation of volumes of water-filled pore space of the column and the mixing vessel $k = \theta V_c / V_{\text{mix}} = V_p / V_{\text{mix}}$	$L^3 L^{-3}$	31–34, 67, 68, 74, 87, 90
k_s	spring constant	$M T^{-2}$	35, 36
<i>L</i>	characteristic length, length of the column	<i>L</i>	22–24, 41, 98
<i>m</i>	mass	<i>M</i>	35, 36
m_k	<i>k</i> -th moment of a random variable		46
m_{pm}	total mass of the porous medium	<i>M</i>	27
<i>n</i>	amount of substance	<i>M</i>	24
n^{end}	final amount of substance	<i>M</i>	24
n^{init}	initial amount of substance	<i>M</i>	24, 25
n_{aqu}	amount of substance in the aqueous phase	<i>M</i>	24
n_e	amount of substance carried with the effluent	<i>M</i>	29
n_f	Freundlich exponent	–	18, 74, 90, 91
n_{gas}	amount of substance in the gas phase	<i>M</i>	24
n_i	amount of substance carried with the influent	<i>M</i>	29
n_{loss}	lost amount of substance	<i>M</i>	24–26
n_{mix}^i	amount of substance in the mixing vessel at timestep <i>i</i>	<i>M</i>	29
n_{mix}^{i+1}	amount of substance in the mixing vessel at timestep succeeding <i>i</i>	<i>M</i>	29
n_{sorb}	sorbed amount of substance	<i>M</i>	24
n_{tot}	total amount of substance	<i>M</i>	24
<i>O</i>	objective function		42–45
<i>P</i>	general source/sink function	$ML^{-3} T^{-1}$	16, 17, 20
<i>Pé</i>	Péclet number, ratio of advective and diffusive transport	–	22, 23, 31, 60, 77–86, 90, 91, 93, 94, 96–102, 109
pK_a	decadic logarithm of the acidity constant	–	53, 76
<i>p</i>	partial pressure	$ML^{-1} T^{-2}$	24
<i>Q</i>	volumetric pumping rate	$L^3 T^{-1}$	22, 29–31, 34, 55, 56, 58, 64, 66, 69, 74, 98, 107, 118

Symbol	Description	Symbol	Page List
q	darcy velocity $q = Q/A$	$L T^{-1}$	15, 16, 19, 21, 22
R	retardation factor	–	19, 21–23, 32–34, 67, 68, 74–76, 84–90, 93, 103, 107
R^2	coefficient of determination	–	43, 60, 72, 99, 100
\Re	real part of a complex number		48
S	sorption coefficient	–	21, 27, 85, 106
s_{\max}	maximal sorbed concentration	MM^{-1}	18
s	sorbed concentration $s = f\sigma + \tilde{f}_c$	MM^{-1}	17, 18, 24, 27
T	duration of an experiment	T	29
t	time variable	T	21, 22, 30, 33, 36, 37, 39, 41
t_i	time at time step i	T	29
Δt	time step	T	29, 55–58
t_{pv}	time in pore volumes	–	22, 31–34, 98, 108
t_{pv}^{\max}	time of first oscillation maximum	–	34, 67, 68, 74
V	volume	L^3	24
V^{end}	final volume	L^3	24
V^{init}	initial volume	L^3	24
V_c	volume of the column	L^3	22, 25–27, 31
V_{loss}	lost volume	L^3	24
V_{mix}	solute volume of the mixing vessel	L^3	25–27, 29– 31, 55, 56, 58, 63–65, 67–69, 72, 75, 98
$V_{\text{mix}}^{\text{inc}}$	solute volume of the mixing vessel plus the flux during a discrete time step $V_{\text{mix}}^{\text{inc}} = V_{\text{mix}} + Q\Delta t$	L^3	56, 58
V_p	water-filled pore space $V_p = \theta V_c$	L^3	25, 64, 65
V_s	volume of the setup and tubing that is not part of the porous medium	L^3	25–27
V_t	total solute volume of a closed-flow experiment	L^3	25, 27
v	mean pore water velocity $v = q/\theta$	$L T^{-1}$	16, 18, 19, 22, 23, 41, 56–58
v_t	mean transport velocity	$L T^{-1}$	18, 19, 23

Symbol	Description	Symbol	Page List
X	random variable		46, 47
x_i	i-th independent variable		42, 43
\mathbf{x}	vector of independent variables		42
x	space variable	L	22, 24, 35, 36
Δx	space step	L	56–58
y_i	i-th dependent variable		42, 43
\mathbf{y}	vector of dependent variables		42, 44
Z	arbitrary substance		18
z	scaled space variable	L	22, 31, 32
Z_{aqu}	substance in aqueous phase		18
Z_{sorb}	substance adsorbed at surface		18
Greek letters			
α	first-order rate coefficient for sorption to non-equilibrium sites	T^{-1}	17, 21, 23
β	fraction of water content in mobile regions	–	20, 21
$\tilde{\beta}$	fraction of water content in immobile regions $\tilde{\beta} = 1 - \beta$	–	20, 21
Γ	initial amplitude	–	36, 37, 99, 100
γ	Levenberg-Marquardt parameter	–	44
δ	Dirac delta function		39, 40
η	volumetric fraction of the gas phase	$\text{L}^3 \text{L}^{-3}$	24
λ	dispersivity, dispersion length	L	16, 22, 72
μ	first moment of a random variable representing the expected value of random variable X		46, 47
μ_k	k -th central moment of a random variable		46
∇	nabla operator, vector containing the partial derivatives in n dimensions $\nabla = (\frac{\partial}{\partial x_1}, \dots, \frac{\partial}{\partial x_n})$		15
Ω	a region of \mathbb{R}^n , representing the n -dimensional space of the column in case of $n = 1$: $\Omega = (0, L)$		24
ω	mass transfer coefficient between mobile and immobile regions	T^{-1}	20, 21, 23
ω_0	undamped angular frequency of an harmonic oscillator	T^{-1}	36, 37, 99, 100, 109
ω_d	damped frequency of an harmonic oscillator	T^{-1}	37, 109
ϕ	isotherm of equilibrium sorption		17, 21
φ	isotherm of non-equilibrium sorption		17, 21
Φ	phase	–	36, 37, 99, 100
\mathfrak{P}	set of parameters used for a model		42–45
ρ	bulk density $\rho = \rho_{\text{eq}} + \rho_{\text{neq}}$	ML^{-3}	17, 21, 24, 27, 74, 98

Symbol	Description	Symbol	Page List
ρ_{eq}	bulk density related to equilibrium sorption $\rho_{\text{eq}} = f\rho$	ML^{-3}	17, 19, 21
ρ_{neq}	bulk density related to non-equilibrium sorption $\rho_{\text{neq}} = \tilde{f}\rho$	ML^{-3}	17, 21
σ	sorbed concentration at equilibrium sorption sites $\sigma = \beta\sigma_{\text{m}} + \tilde{\beta}\sigma_{\text{im}}$	MM^{-1}	17
σ_{im}	sorbed concentration at equilibrium sorption sites in the immobile region	MM^{-1}	21
σ_{m}	sorbed concentration at equilibrium sorption sites in the mobile region	MM^{-1}	21
σ^2	variance	L^2	44
ς	sorbed concentration at non-equilibrium sorption sites $\varsigma = \beta\varsigma_{\text{m}} + \tilde{\beta}\varsigma_{\text{im}}$	MM^{-1}	17, 21
ς_{im}	sorbed concentration at non-equilibrium sorption sites in the immobile region	MM^{-1}	21
ς_{m}	sorbed concentration at non-equilibrium sorption sites in the mobile region	MM^{-1}	21
τ	residence time in the porous medium	T	23
θ	volumetric water content $\theta = \theta_{\text{m}} + \theta_{\text{im}}$	$\text{L}^3 \text{L}^{-3}$	16, 19–22, 24–27, 31, 64, 66, 74, 98
θ_{app}	apparent volumetric water content	$\text{L}^3 \text{L}^{-3}$	26, 27
θ_{im}	immobile volumetric water content $\theta_{\text{im}} = \tilde{\beta}\theta$	$\text{L}^3 \text{L}^{-3}$	20, 21
θ_{m}	mobile volumetric water content $\theta_{\text{m}} = \beta\theta$	$\text{L}^3 \text{L}^{-3}$	20, 21
ϑ	temperature	Θ	24, 45
ζ	damping ratio of harmonic oscillator	–	36, 37, 99, 100
Constants			
e	2.718 281 828		21, 30, 32–34, 36, 37, 41, 45, 47, 48
k_{b}	$1.380\,648\,8 \times 10^{-23}$	JK^{-1}	45
π	3.141 592 654		41, 47, 48, 99
R_{m}	8.314 462 1	$\text{J mol}^{-1} \text{K}^{-1}$	24

1 Introduction

1.1 Motivation

The pedosphere is one of the most complex structures on earth. Despite the fact that its size is comparably small to other spheres, it carries functions, without whom most of the present life would not be able to survive (Blum 2005). To raise the awareness of the fundamental relevance of soil, the UN declared 2015 the “International Year of Soils” (United Nations General Assembly 2013). Soil carries multiple functions that are determined by soil structure (Peng et al. 2015; Horn et al. 1994) and soil constituents (Murphy 2014; Nannipieri et al. 2003; Wander 2004). A prominent example of major importance is the filter function (Keesstra et al. 2012). The quality of groundwater as crucial resource of society (Winter et al. 1998) is strictly dependent upon this function and thus, for generations soil research focused on the interactions of an infiltrating mobile phase, i.e. usually rainwater, with the porous medium represented by the soil (Horton 1933; Totsche et al. 2010). Yet, soil science still faces grand challenges in quantitatively understanding soil as a combination of separate underlying processes (Baveye 2015). In addition, the description of soil processes at different scales is fundamentally different and large scale effective parameters evolve from small scale parameters via “upscaling” (e.g. Samouëlian et al. 2007). To draw significant conclusions about separate processes, they have to be studied in an experimental approach that produces results that are indicative for that particular function or process. Despite the relatively simple concepts and models behind separate soil processes, their multiplicity, complex interaction and the involved feedbacks (Daly and Porporato 2005; Beatty and Smith 2013) render their unique characterization a challenging task. The development of experimental approaches that provide observations that can be uniquely attributed to these processes is therefore at the basis of soil science and applied scientist as well as engineers rely on reliable methodological innovations to study processes or determine specific parameters.

The scientific literature is filled with new experimental setups that are suited for the investigation of specific aspects of solute transport, e.g. by using micromodels to decrease the observation scale (Baumann and Werth 2004), by using multiple layers to simulate heterogeneity (Porro et al. 1993) or by setting up a network of lysimeters at the field scale to efficiently derive data that is uniquely attributable to the underlying processes (Ellsworth et al. 1996). Besides experiments with, e.g., lysimeters at the field scale and soil

in situ, the most widespread approach to study solute transport found in soil science is the laboratory scale column outflow experiment (Lewis and Sjöstrom 2010), which usually observes soil processes at the continuum scale. Their wide application is due to ease of use and the possibility to subject the soil to reproducible and defined boundary conditions. Through variation of these boundaries, a flexible adaption with regard to underlying research focus is possible to a large extent. For instance, a change in pore water velocity reveals non-equilibrium in transport (e.g. Brusseau 1992; Koch and Flühler 1993; Wehrer and Totsche 2003), affects transport of bacteria (Camesano and Logan 1998; Syngouna and Chrysikopoulos 2012) and the mobility of colloids (e.g. Bradford and Torkzaban 2008; Knappenberger et al. 2014). At the same time, soil cores can be used under almost undisturbed conditions to preserve soil structure (Lewis and Sjöstrom 2010). Despite these advantages, also the column outflow design suffers from certain drawbacks that limit their application and the interpretation of results. In these cases, the combination of different complementary experimental designs is needed to fill specific gaps in the information content of each particular approach.

For this reason, this thesis is devoted to comprehensively discuss and introduce a complementary approach of conducting column outflow experiments based on the closed-flow design presented by Totsche (2001). Following a thorough discussion on limitations found in classical approaches of studying solute transport in porous media discussed in the next sections, the closed-flow design will be presented from a theoretical, experimental and numerical point of view. With that, an exhaustive overview of prospects and limitations of this design will be given to identify all important aspects of closed-flow column experiments. This also permits the assessment of the suitability of the proposed design in cases, where the classical approaches struggle.

1.2 Classical Column Experiments

1.2.1 Description of the Experimental Design

Column experiments are the common approach to investigate solute transport in porous media (Lewis and Sjöström 2010). They are usually carried out with cylindrical columns of variable length. These columns are filled with a porous medium, e.g. an undisturbed soil core (monolithic core), a packed soil from homogenized soil samples or a mixture of minerals with well-defined grain sizes, also referred to as “artificial soil”. A detailed description of the application of these soil types is given in the next subsection. Filters are placed at the bottom of the column and build the lower boundary. In general, a column experiment can be conducted in two modes, either saturated or unsaturated.

Saturated Experiments

Saturation of soil columns is usually carried out by pumping liquid from the bottom to the top of the column. However, the process of imbibition is depending on initial saturation (Li et al. 2013, 2014), pore structure (Dawson et al. 2013) and fluid properties represented by the capillary number (Yu and Middleman 1993). As a result, full saturation is usually not achieved in natural porous media due to air that is entrapped in the pore structure (Holocher et al. 2002), especially relevant for soil showing a high hydrophobicity (Sullivan 1990). The occurrence of air bubbles in the pore structure has large influence on soil hydraulic properties (Faybishenko 1995) and is a major cause of hysteresis (Kool and Parker 1987) and therefore is also included in flow models (Parker and Lenhard 1987; Wang et al. 1997). However, if the flux is controlled via a pumping device, the effect of hysteresis is negligible (Kaluarachchi and Parker 1987).

During the actual tracer test, a steady-state flow is then achieved by the pumping device against gravity. As a result, the boundary conditions, i.e. the upper and lower filter and the flow rate, can be controlled and adjusted very precisely by the experimenter. This approach also allows for a simplified simulation of transport provided the soil is distributed homogeneously and the column covers a representative elementary volume, because

1. the influence of capillary forces can be neglected at saturation (e.g. Brooks and Corey 1964),
2. the water content can be considered stationary and homogeneous,
3. and therefore the volumetric water flow rate is constant over the profile (e.g. Bear 1988).

For the named reasons, saturated transport experiments are often used in groundwater research (e.g. Huang et al. 1995), where the pore space is almost void of air (Figure 1.1).

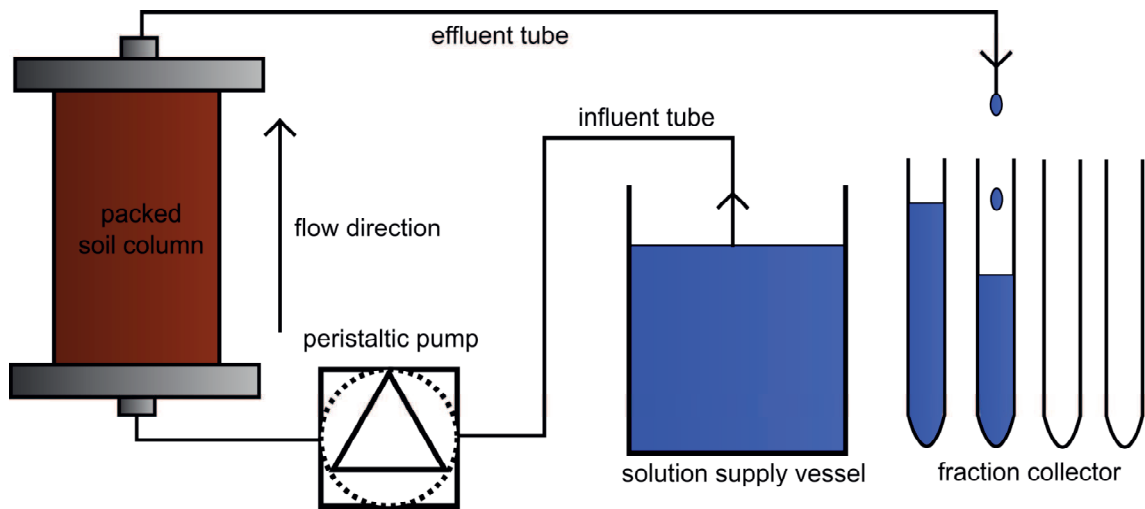


Figure 1.1: Schematic setup of a laboratory scale open-flow column experiment with saturated flow.

Unsaturated Experiments

Flow and transport especially in soils is unsaturated in most cases, i.e. part of the pore space is filled with air. This has a huge impact on the flow regime (Richards 1931) and solute transport (Nielsen et al. 1986; Wierenga and van Genuchten 1989) depending on the water retention characteristics (Brooks and Corey 1964; van Genuchten 1980). To simulate the gravity-driven infiltration process, the upper boundary of the column experiment is replaced by a headspace and a sprinkling unit (Figure 1.2). The lower boundary can be adjusted by the application of a vacuum unit to produce a defined pressure. The boundary conditions are then atmospheric pressure and the pressure provided by the applied device.

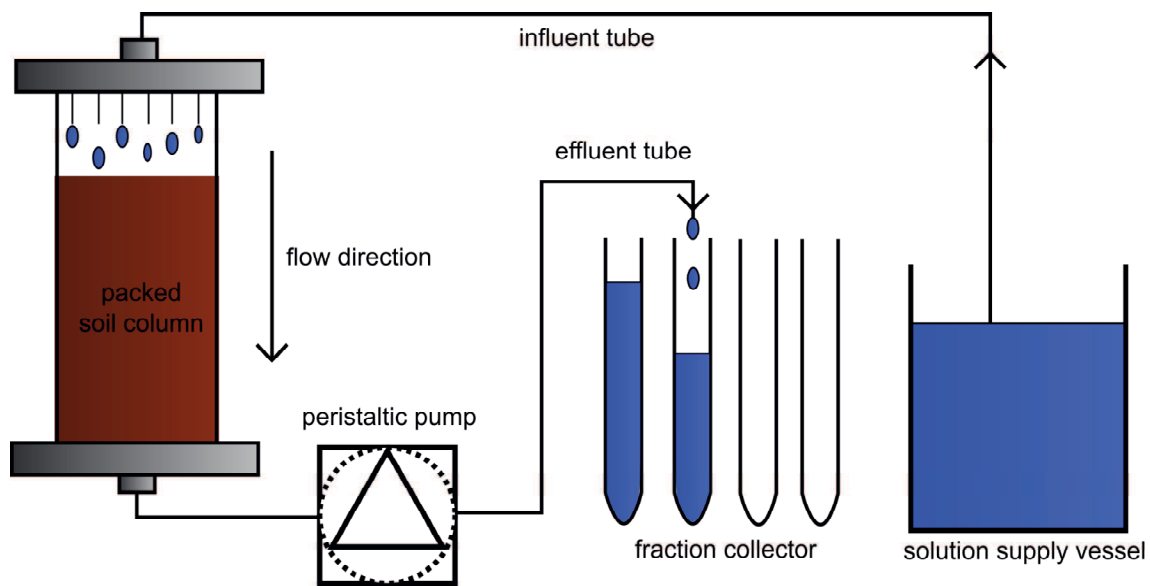


Figure 1.2: Schematic setup of a laboratory scale open-flow column experiment with unsaturated flow.

1.2.2 Porous Media used in Column Experiments

Monolithic Soil Cores

The utilization of monolithic soil cores keeps the structure and the microbial inhabitation of the soil intact. They can be used in situ for field studies with lysimeters or in the laboratory after the core is sampled. The sampling technique is crucial to minimize disturbances at the edges (Persson and Bergström 1991). Monolithic soil cores generally are as close to nature as possible and are mandatory for studies involving preferential flow (Hendrickx and Flury 2001; Flury et al. 1994), especially its quantification (Allaire et al. 2009). However, the occurrence of preferential flow is also the major drawback of undisturbed cores when the main focus of column experiments lies on chemical and biological features of the soil sample, which can be overprinted by a heterogeneous flow regime. This makes observations gathered with this kind of porous medium, although close to nature, sometimes hard to interpret. Additionally, special care has to be taken in order to sample a representative volume (Allaire et al. 2009).

Homogenized Soil

To circumvent these difficulties, the main soil structure and thus, the natural flow regime is often destroyed by homogenization, e.g. through sieving. When re-packed into columns, this has a huge impact on the physical properties of the flow regime (Bromly et al. 2007) and the microbial communities, especially if the soil is dried (Thomson et al. 2010). The sieving procedure can be optimized to maintain the internal aggregate structure (Saygin

et al. 2012). However, the chemical reactivity of minerals, the composition of organic matter, the amount of sorbed substances and the chemical milieu in equilibrium with an aqueous phase is not altered by the sieving process. Therefore, the overall reactivity is not strongly affected, but the kinetics of biological (Bach and Hofmockel 2014) and chemical interactions (ter Laak et al. 2007) can be totally different due to limitations in transport and immobile regions when using undisturbed soil cores.

Artificial Soil

For studies on isolated processes (e.g. the sorption of contaminants on specific minerals), the interference of variable soil composition and diverse microbial activity constitutes a serious issue. An approach which minimizes these unwanted artifacts is the application of artificial soils, which is made of well-defined mixtures of pure mineral phases with known grain size distribution (e.g. Hofman et al. 2014). Quartz in sand and silt fraction is often used as inert matrix and mixed with reactive minerals, e.g. goethite or montmorillonite. When incubated with bacterial communities, specific effects of microbial activity on ,e.g., transport, aggregation or mineral stability can be investigated (Pronk et al. 2012; Vogel et al. 2014).

1.2.3 Tracers in Column Experiments

A tracer is a substance that is applied to the porous medium in order to study the properties and processes that act on the aqueous phase under the given boundary conditions. Depending on the research focus, a tracer is usually selected to provide distinct information about the selected process at the same time limiting the influence of interfering processes to the largest possible extent. Generally, tracers can be divided into two main groups, i.e. conservative tracers and reactive tracers.

Conservative Tracer

A conservative tracer is a substance, whose mass is conserved in the aqueous phase in the form it is applied to the porous medium. In this way, all processes that cause a source or sink in concentration must not apply to this particular compound. Common examples are salts, non-reactive dyes or isotopes (Leibundgut et al. 2009). The exclusion of all biological processes and liquid solid interaction renders conservative tracers as perfectly suited for the investigation of physical properties of the porous medium and the flow regime. Consequently, many studies on solute dispersion, diffusion and preferential flow in porous media (Vanderborght and Vereecken 2002; Koch and Flühler 1993; Brusseau and Rao 1990) apply conservative tracers, a procedure that is also a standard preliminary step for the

investigation of reactive transport in order to characterize the non-reactive reference state (e.g. Weigand et al. 2002; Wehrer and Totsche 2005).

Reactive Tracers

Reactive tracers are affected by all processes that also act on conservative tracers since all physical aspects of solute transport naturally also apply. In addition, a reactive tracer shows a more or less specific reactivity towards further constituents of the porous medium, e.g. the solid phase or microorganisms. Breakthrough curves (BTCs) that are obtained with reactive tracers contain information on this particular reaction, e.g. sorption or microbial degradation (e.g. Angley et al. 1992; Das et al. 2004; Jaesche et al. 2006), which can then be used to derive interaction parameters, e.g. distribution coefficients or decay rates. However, in case of microbial decay, the transport of microorganisms (Ginn et al. 2002; Tufenkji 2007) as well as the dynamics of microbial populations has to be considered (Corapcioglu and Haridas 1984), frequently represented in terms of Monod kinetic (Molz et al. 1986; Cheyns et al. 2010; Wehrer et al. 2012). Generally, a reactive tracer can be considered a probe for processes of chemical and biological interactions in porous media. Due to the interference of several transport processes, the evaluation of reactive tracer BTCs should always include a comparison to the corresponding conservative tracer BTC.

1.3 Limitations of Classical Approaches

In column experiments, it is mandatory to assess major boundary conditions and soil specific properties before the actual tracer experiment in order to characterize the initial conditions. For instance, a precise determination of the volumetric water content is an important prerequisite to successfully apply transport models and draw reliable conclusions (Tang et al. 2009). The gravimetrical assessment via difference weights of soil cores before and after saturation demands a completely dry substrate usually ascertained by oven-drying. However, the process of drying impacts soil structure (Horn et al. 1994), the mineral composition (Kalkan 2011), the water repellency (Vogelmann et al. 2013; Dekker et al. 2001) and the mobility of heavy metals (Koopmans and Groenenberg 2011), particles (Majdalani et al. 2008) and PAH (Beriro et al. 2014). Furthermore, the microbial community reacts strongly on changes in soil moisture (e.g. Bottner 1985; Kieft et al. 1987; Thomson et al. 2010; Ouyang and Li 2013). As reviewed by Kaiser et al. (2015), the effect on soil organic matter is very severe even when the soil is subjected to air-drying instead of oven-drying. However, for a reliable gravimetrical determination of the water content, a complete drying is necessary, which can only be done in an oven at elevated temperature, which dramatically worsens the situation.

Classical open-flow experiments feed the inflow via a solution supply vessel. The experimenter completely decides on the chemical composition of the tracer solution inside this vessel including its temporal course. Hence, the porous medium is driven towards the solution chemistry of the influent when the solution is kept constant. A comparison to the mathematical concept of an attractor is convenient for conceptualization at this point:

An attractor is a set of states (points in the phase space), invariant under the dynamics, towards which neighboring states in a given basin of attraction asymptotically approach in the course of dynamic evolution. ... (Weisstein 2015)

The solution of the supply vessel can be considered the attractor of open-flow experiments and the set of states represent specific chemical properties, e.g. the concentration, the pH and the redox potential. Independent of the soil that is used for the experiment, the long-term state of the effluent is solely given by this attractor if no unlimited source or sink acts on the tracer solution while passing the column. The characteristics of possible interaction, e.g. the increase in pH due to anion sorption coupled to the release of OH^- (e.g. Hingston et al. 1972; Parfitt 1979), is not maintained since the solution that holds this feedback is washed out of the porous medium permanently. As a result, subsequent liquid solid interactions that are strictly dependent on the pH, e.g. cation sorption (Filius et al. 1997; McKenzie 1980; Dzombak and Morel 1990) and anion sorption (Hiemstra and Riemsdijk 1999; Ali and Dzombak 1996; Evanko and Dzombak 1999), are affected severely

due to changes in the surface charge of minerals depending on the point of zero charge (PZC) (Kosmulski 2014).

For this reason, interactions at the liquid solid interface are often investigated via completely mixed batch reactors, where the solution is allowed to equilibrate with the solid. Here, the attractor is determined by the entire system including its boundary and all involved reactions and feedbacks. The physicochemistry of the solution evolves in direction of the shared equilibrium between all phases. Interactions that are strongly dependent on the solution chemistry might be affected tremendously by this development (e.g. Wise 1993), rendering this scenario more relevant for natural conditions, where feedbacks are intrinsic. However, all aspects related to transport in a porous medium are suppressed by this experimental design. As a result, differences in sorption strength in orders of magnitude are found when both experimental approaches are compared, especially for high liquid to solid ratios (Wang et al. 2009). Additional issues that complicate the interpretation of results from batch tests are particle abrasion (Porro et al. 2000; Schweich and Sardin 1981) and non-natural liquid to solid ratios (Voice and Weber 1985; McKinley and Jenne 1991). For those reasons, interaction parameters reconstructed from batch experiments often fail in predicting the solute transport in column outflow experiments (Vereecken et al. 2011).

To conclude, completely mixed batch reactor experiments maintain feedbacks of interaction and allow an equilibration of liquid and solid phases, but neglect all aspects of transport. In contrast, classical column outflow experiments represent a transport regime comparable to natural soils, but suppress feedbacks to a large extent. In addition, the sample pretreatment in both experimental designs is a critical step, which might completely alter the properties of the sample. As a consequence of this comparison, the most suggestive approach is a combination of both experimental designs in a way the advantages prevail.

1.4 The Closed-Flow Design

1.4.1 Concept

Grolimund et al. (1995) introduced a flow-through reactor setup, where a solid sample was rinsed with solution in a closed loop until establishment of equilibrium. In this way the authors aimed at characterization of sorption while avoiding the problems linked to completely mixed batch reactor experiments. Totsche (2001) evolved the idea of solute recirculation to packed soil columns at saturated conditions. Compared to a classical open-flow experiment, the only difference of a closed-flow mode is the recirculation of effluent solution into the solution supply vessel that feeds the inflow. As a result, this vessel is subjected to the permanent mixture of solutes and is therefore referred to as “mixing vessel” in the following sections (Figure 1.3). The setup of the soil column and the tubing remains the same and every open-flow setup can be easily reconfigured into a closed-flow setup. The total volume of solutes inside the porous medium and the mixing vessel stays constant in this approach. Furthermore, two situations are possible regarding the mixing vessel (Totsche 2001):

1. The solute volume inside the mixing vessel stays constant

This is the case when the column experiment is run with a constant water content, i.e. the volume of effluent and influent solution are identical (usually in saturated experiments).

2. The solute volume inside the mixing vessel is changing

If the saturation of the column experiment changes due to a variable flow regime, the mixing vessel volume reacts accordingly.

Regardless of this distinction, a mass balance with respect to water volumes is possible and a change in mixing vessel solute volume necessarily implies a change in saturation of the porous medium.

The closed loop also causes the system to adhere to a closed mass balance with respect to the solute composition (Totsche 2001). Therefore, any tracer solution applied to a closed-flow experiment, although subjected to all involved transport processes, converges to a constant concentration due to transport processes that reduce gradients. In case of conservative tracers, the concentration to which the system is attracted to is fully determined by the water-filled volume of all compartments. This behavior can be used in order to predict the non-reactive chemical equilibrium or to determine the water content from the observation of the converging concentration. Details on the calculation are given in subsection 2.3.3. It is important to provide a reproducible boundary condition in the mixing vessel by stirring of the mixing vessel solution, which is necessary to avoid local gradients in the mixing vessel (Schmidt 2010).

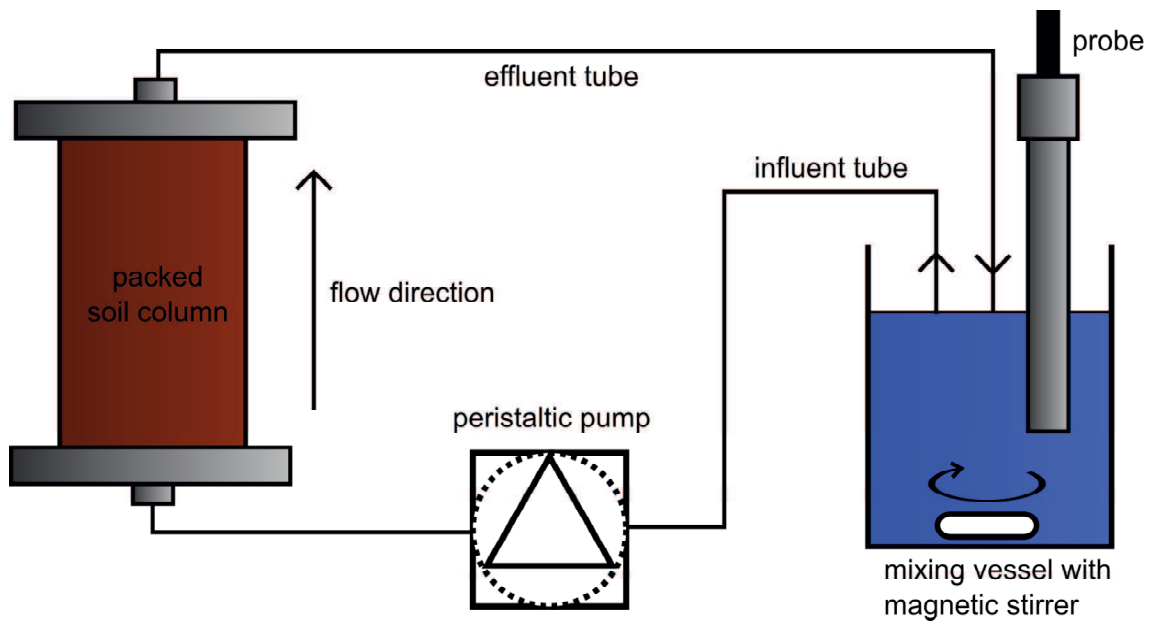


Figure 1.3: Schematic setup of a laboratory scale closed-flow column experiment.

When a reactive tracer is used, the equilibrium is also influenced by sinks due to sorption and shows differences to the non-reactive reference state (Ritschel and Totsche 2016b, 2016a). However, if decay can be ruled out and liquid solid interaction is the process that causes the sink, still a stable equilibrium is reached. This equilibration is a main feature of closed-flow experiments and is comparable to completely mixed batch reactor experiments for the investigation of sorption. Thus, also in closed-flow experiments the interactions are subjected to the feedback affecting the chemical milieu. As a result, not only the concentration converges to a stable state, but also the solution equilibrates with the porous medium with respect to redox potential, ionic strength, pH, chemical composition and solubility of minerals. This allows the solution to reach an attracting chemical equilibrium that is not permanently forced in the direction of the solution chemistry of the supply vessel and the feedback of interaction is preserved.

1.4.2 Emergence of Concentration Oscillations

Totsche (2001) discovered that closed-flow experiments in which the solute volume of the mixing vessel is smaller than the water-filled pore space result in sinusoidal concentration oscillations in the BTC. The explanation for this phenomenon is directly related to the recirculation of solution into the mixing vessel. It is assumed that the porous medium is initially water-saturated and free of tracer and the mixing vessel is filled with a tracer solution with concentration $c_{\text{mix}}^{\text{init}}$. By starting the pump, the solution of the mixing vessel is fed to the column and starts to displace the resident fluid volume that is free of tracer. The displaced fluid volume exits the column and enters the mixing vessel, thereby resulting in

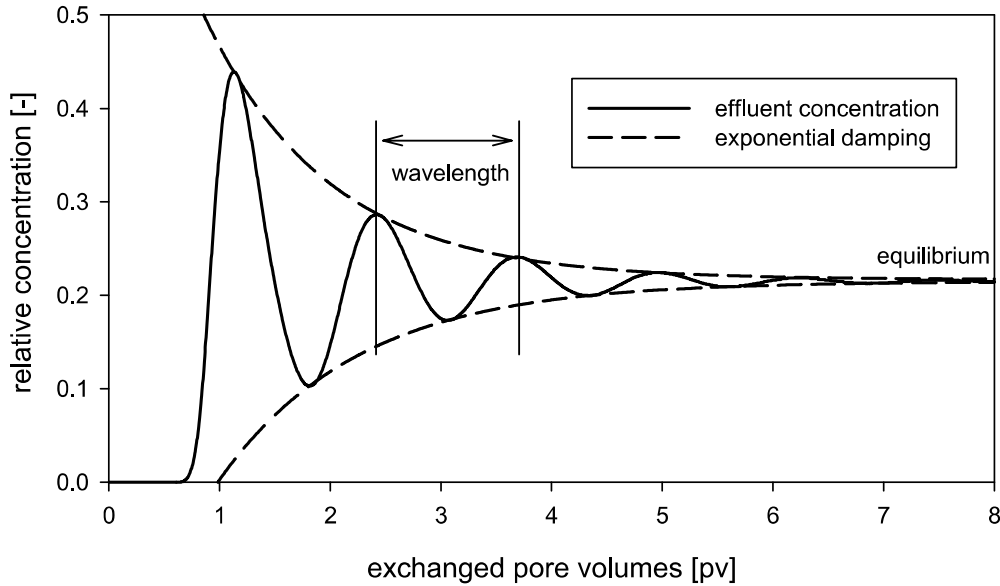


Figure 1.4: BTC of a conservative tracer measured in the effluent of a closed-flow experiment, the exponential damping was calculated assuming a damped harmonic oscillator (preliminary experiment to visualize BTC features with a column filled with quartz sand).

a dilution of solute concentration in the mixing vessel. Thus, also the inflow concentration decreases constantly over time provided that the mixing vessel is rigorously stirred. Under these conditions, a boundary condition with a negative gradient is created. Upon the first breakthrough of the tracer through the column, highly concentrated solution exits the column. Therefore, the concentration in the mixing vessel rises again and thus, the influent concentration also rises. After the pulse-like highly concentrated breakthrough has passed, the effluent solution decreases in concentration, resulting in a decrease in solute concentration in the mixing vessel. This process is repeated until concentration gradients have diminished due to diffusion, dispersion and the mixing in the mixing vessel. The cycling of tracer through the column multiple times is then seen as an oscillating concentration in both, the effluent and the mixing vessel. To get a first impression on how these oscillations are shaped, a typical breakthrough at the column outflow is depicted in Figure 1.4. The oscillation can be seen here for about five wavelength until a stable equilibrium is reached.

Under consideration of the argumentation given above, the BTC shows oscillations due to the dynamic influent solution given via the mixing vessel. For this reason, an oscillating BTC must also be present in the mixing vessel, shifted by the time needed for the passage of a tracer pulse through the column. Otherwise, no oscillating BTC could be seen in the effluent, which can be regarded a function of the influent solution convolved with

the transport phenomena in the column. A more detailed discussion of this concept also referred to as “transfer functions” is given in subsection 2.6.1. The important implication of this mixing cycle is the two modes of measuring BTCs, either classically in the effluent or alternatively in the mixing vessel.

To reconsider the shape of the BTC, the oscillations also imply the emergence of new unique features besides the equilibrium state (Ritschel and Totsche 2016b):

1. initial exponential decrease in the mixing vessel
2. wavelength
3. amplitude, extent of damping
4. asymmetry of oscillation

The transport processes inside the column manifest in these features in distinct ways, which will be analyzed and mathematically derived in the following theoretical sections. For each feature, an intuitive interpretation exists, rendering the BTC of a closed-flow setup much more indicative than a BTC obtained under comparable conditions in open-flow.

The initial exponential decrease in concentration is not seen in Figure 1.4 and only applies to BTCs measured in the mixing vessel, which is discussed in detail in section 2.4.2. This feature can be considered the rate of dilution and is related to the flow rate and the volume of the mixing vessel. A high flow rate or a small mixing vessel forces a fast dilution and thus, a decrease in concentration whereas a low flow rate or large mixing vessel results in a slow reaction of the mixing vessel solution with respect to the effluent solute composition. The wavelength is a direct indication of the breakthrough of the centre of mass (BCM) since it represents the time for the solute pulse to travel through the column and the mixing vessel exactly once. The development of the amplitude represents the influence of processes that reduce concentration gradients and hence, is connected to the mixing in the mixing vessel and dispersion/diffusion. The asymmetry of the oscillation is likely an indication of nonlinear or rate-limited processes comparable to tailing and asymmetry in open-flow BTCs (Vereecken et al. 2002; Fesch et al. 1998).

Interestingly, the oscillation is similar to the damped harmonic oscillator, which is also discussed in detail in section 2.5.

1.5 Main Hypotheses

The novel approach of solute recirculation in column experiments and the oscillating BTC suggest several hypotheses, which are to be tested and investigated in this thesis.

1. Transport parameters are reflected in distinct closed-flow BTC features and can be extracted from measurements uniquely.
2. The appearance of concentration oscillations and thus, the sensitivity of the BTC to transport parameters that imprint on the oscillations is dependent on the mixing vessel and can therefore be controlled by the experimenter.
3. Transport parameters can be determined with higher sensitivity as compared to classical approaches.
4. The kinetics of interactions can be studied directly under conditions of transport in a porous medium.

These hypotheses also represent the main focus and motivation used to structure the argumentation of this thesis. A detailed answer to the hypotheses is given in section 5.2.

2 Theoretical Considerations

2.1 Transport Equation

2.1.1 Fluxes and Continuity Equation

At the continuum scale, transport in porous media is often represented by the advection dispersion equation (ADE), a nonlinear partial differential equation (PDE) that describes the temporal change of concentration, i.e. the solute propagation. In a basic form, it was derived by Smoluchowski (1916) to extend the laws of diffusion to cases, where external forces, i.e. a moving fluid in context of solute transport, causes an additional movement of solutes. By addition of further processes, it is very flexible in reconstructing transport phenomena in laboratory scale transport experiments and is therefore used for the mathematical representation of transport in numerical or analytical simulations. The constitutive laws are derived from considerations on the continuum scale and therefore lose validity or require further attention when applied to larger or smaller scales, e.g. pore scale or field scale. However, Khan and Jury (1990) showed that solute transport in laboratory scale column outflow experiments behaves according to the ADE if the columns are repacked from sieved homogenized material. As this applies to all conducted experiments, the mathematical description of transport used in this thesis for the analysis of closed-flow experiments is based on the ADE.

In the following derivation, the one-dimensional spatial derivative ∂_x is used as representation for spatial gradients or divergence and ∂_t is used as representation for temporal gradients. For higher dimensional approaches, ∂_x has to be replaced by the Nabla operator ∇ , which is a vector of the spatial derivatives in each dimension. The ADE is based on the definition of fluxes J due to:

1. advection

$$J_a = qc \tag{2.1}$$

with q as the Darcy velocity¹.

¹Named after Henry Darcy (1803-1858), who empirically derived Darcy's law (Darcy 1856), which is now known to actually derive from the Navier–Stokes equations (Whitaker 1986).

2. molecular diffusion according to Fick's law of diffusion²

$$J_m = -D_m \partial_x \theta c = -\theta D_m \partial_x c \quad (2.2)$$

with D_m as diffusion coefficient and θ as volumetric water content.

3. hydromechanic dispersion including Taylor-Aris dispersion³ with an analogous formulation

$$J_h = -D_h \partial_x \theta c = -\theta D_h \partial_x c, \quad (2.3)$$

where $D_h = \lambda v$ and D_h is the dispersion coefficient, λ is the dispersion length and v is the mean pore water velocity.

The statements in Equation (2.2) and Equation (2.3) are often combined to an apparent dispersive flux using D as apparent dispersion coefficient

$$J_d = -\theta D_m \partial_x c + \theta D_h \partial_x c = -\theta (D_m + D_h) \partial_x c = -\theta D \partial_x c, \quad (2.4)$$

because they are phenomenologically and mathematically analogous at the scale of the experiments. These fluxes are then inserted into the continuity equation that represents a the law of mass conservation according to

$$\partial_t \theta c + \partial_x J = P, \quad (2.5)$$

which results in a basic formulation of the ADE if J is substituted with $(J_a + J_d)$

$$\partial_t \theta c = \partial_x (\theta D \partial_x c - qc) + P. \quad (2.6)$$

The general source/sink function P can be replaced by terms describing chemical interactions, biological processes and the distribution between different phases.

2.1.2 Chemical Interactions

Interactions at the liquid solid interface are characterized by an isotherm, which is defined as the function describing the concentration at the surface in relation to the concentration in the aqueous phase at constant temperature (Giles et al. 1974a, 1974b). The isotherm only describes the situation for chemical equilibrium and does not cover the kinetics of

²Named after Adolf Fick (1829-1901), who introduced this law empirically (Fick 1855) to describe the macroscopic effect of Brownian motion (Brown 1828). Later on, Einstein (1905) showed that Fick's law actually derives from theoretical considerations of thermodynamics.

³Named after Sir Geoffrey Taylor (1886-1975) and R. Aris, who studied dispersion in single tubes (Taylor 1953; Aris 1956).

adsorption. However, chemical interactions are often separated into equilibrium and kinetic reactions (van Genuchten et al. 1974; van Genuchten 1981b). In contrast to dividing the sorption coefficient K_d , the bulk density of sorption sites was divided into the fractions obeying equilibrium and rate-limited kinetics in this derivation, each given its own K_d value instead. In this way, two completely different adsorption sites can be simulated (Knabner et al. 1996). Specifically, the total bulk density ρ is divided into the part of the bulk density offering equilibrium sorption sites ρ_{eq} and the part offering sorption sites with rate limited exchange ρ_{neq} . The ratio of these sites is given by f according to

$$\rho_{\text{eq}} = f\rho \quad (2.7)$$

$$\rho_{\text{neq}} = (1 - f)\rho = \tilde{f}\rho. \quad (2.8)$$

Equilibrium sorption is defined as liquid solid interaction, where the concentrations in the liquid and the solid phase are instantaneously equilibrated according to the underlying isotherm $\sigma = \phi(c)$, where σ is the sorbed concentration at equilibrium sites. The well-established models for equilibrium sorption (Lapidus and Amundson 1952; Hashimoto et al. 1964) define P by

$$P = -\rho_{\text{eq}}\partial_t\sigma \quad (2.9)$$

$$\partial_t\sigma = \partial_t\phi(c). \quad (2.10)$$

The models for kinetic interactions introduce a rate constant α that limits the exchange between the phases. The standard approach is to include a first-order kinetic (Hougen and Marshall 1947; van Genuchten and Wierenga 1976) limited by the isotherm describing the non-equilibrium sorption sites according to $\varsigma = \varphi(c)$, where ς is the sorbed concentration at non-equilibrium sites. This results in a sink following

$$P = -\rho_{\text{neq}}\partial_t\varsigma \quad (2.11)$$

$$\partial_t\varsigma = \alpha(\varphi(c) - \varsigma). \quad (2.12)$$

To provide a fully determined model, the isotherm for the sorbed concentration s has to be specified. The most common isotherms, which also build the basis for this work, are

1. Linear isotherm

$$s = K_d c \quad (2.13)$$

2. Freundlich isotherm⁴

$$s = K_f c^{n_f} \quad (2.14)$$

3. Langmuir isotherm⁵

$$s = \frac{K_1 s_{\max} c}{1 + K_1 c} \quad (2.15)$$

A linear isotherm can be derived directly from a consideration of chemical equilibrium for the reaction of a substance Z according to $Z_{\text{aqu}} \rightleftharpoons Z_{\text{sorb}}$. The law of mass action results in a distribution coefficient K_d following

$$K_d = \frac{[Z_{\text{sorb}}]}{[Z_{\text{aqu}}]} = \frac{s}{c}. \quad (2.16)$$

However, the assumptions needed for this relationship, e.g. unlimited capacity of equivalent sorption sites that do not interfere with each other, are often not valid for adsorption and only apply to solute distribution between phases. Therefore, the Freundlich isotherm uses an extension to the linear isotherm by adding an empirical exponent n_f to the concentration to empirically describe the interactions between sorbates, resulting in a nonlinear relationship. This approach has been used to successfully describe liquid solid interactions, especially in soils via ion-exchange (Sposito 1980) and applied to, e.g., dissolved organic carbon (DOC) sorption (Kothawala et al. 2008), competitive heavy metal sorption (Gutierrez and Fuentes 1993; Vidal et al. 2009) or the adsorption of anions (Wu et al. 2002). A comprehensive overview over other possible sorption isotherms is given in Hinz (2001) or Limousin et al. (2007). As easily seen, the linear isotherm is a special case of the Freundlich isotherm for $n_f = 1$.

The Langmuir isotherm covers the aspect of limited sorption sites on the surface by a consideration of sorption and desorption kinetics (Sposito 1979). This approach is in a more mechanistic manner than the Freundlich-type equations and intuitive parameters, e.g. the sorption capacity s_{\max} can be derived. This led to an extensive use of Langmuir isotherms in soil science (Veith and Sposito 1977). However, an exhaustive consideration of interfering processes, e.g. surface precipitation (Sposito 1987), is important for a meaningful interpretation of Langmuir parameters (Harter and Baker 1977).

2.1.3 The Retardation Coefficient

Retardation is the phenomenon observed when the mean transport velocity v_t is not equal to the mean fluid velocity, which equals the mean pore water velocity v in case of column

⁴Named after Herbert Freundlich (1880-1941), who introduced this isotherm (Freundlich 1907).

⁵Named after Irving Langmuir (1881-1957), who introduced this isotherm (Langmuir 1916).

experiments with aqueous phases. The retardation factor R is defined as ratio of these velocities given by

$$R = \frac{v}{v_t}. \quad (2.17)$$

In most cases, v_t is lower than the fluid velocity due to interactions with non-aqueous phases. The dynamic removal from the aqueous phase by, e.g., distribution to a stagnant gas phase or sorption to the liquid solid interface, causes a retention inside the non-aqueous phase or at the specific interface until the substance reenters the fluid phase. During this residence time, advection does not apply to the substance, which decreases the mean transport velocity in comparison to that of the fluid.

Nonetheless, under conditions of pore size or charge exclusion, the mean transport velocity can be accelerated since transport is restricted to larger pores with a higher mean fluid velocity. Then, the substance is not accelerated with respect to the fluid in the particular pore, but with respect to the mean fluid velocity, which also accounts for low velocities in small-sized pores. This process is often described as straining and can be observed for mineral colloids (Grolimund et al. 1998; Bradford et al. 2003), microorganisms (Ginn et al. 2002; Hubbard et al. 2001) as well as viruses (Rehmann et al. 1999). Another possible reason for an observed retardation smaller unity is the presence of reactive mobile sorbents (Knabner et al. 1996; Totsche et al. 1996).

In case of equilibrium sorption following a linear isotherm, the retardation coefficient can also be mathematically defined in terms of the sorption mechanism (Hashimoto et al. 1964). To illustrate this, the combination of Equation (2.9) with Equation (2.13) is inserted into the ADE according to Equation (2.6). A subsequent rearrangement yields

$$\partial_t \theta c + \rho_{\text{eq}} \partial_t K_d c = \partial_x (\theta D \partial_x c - qc) \quad (2.18)$$

$$\partial_t \theta c \left(1 + \frac{\rho_{\text{eq}} K_d}{\theta}\right) = \partial_x (\theta D \partial_x c - qc) \quad (2.19)$$

$$R \partial_t \theta c = \partial_x (\theta D \partial_x c - qc) \quad \text{where} \quad R = 1 + \frac{\rho_{\text{eq}} K_d}{\theta}, \quad (2.20)$$

with the mathematical definition of the retardation factor in Equation (2.20). This derivation shows that sorption with linear distribution results in a mathematical formulation that simplifies to a dimensionless factor. This scalar is multiplied with the change in concentration over time in the ADE and therefore can also be interpreted as the inverse relative transport velocity.

2.1.4 Immobile Pore Water

The ADE as presented in Equation (2.20) can reconstruct major features of the BTC obtained in column experiments. Solute propagation is covered by advective fluxes, the

broadening of solute gradients is accounted for by dispersion/diffusion and retardation is modeled by sorption. However, many observed BTCs from column experiments show a non-sigmoid form, often called “tailing” (Giddings 1963) due to non-equilibrium (Šimůnek et al. 2003). Besides non-equilibrium resulting from chemical interactions associated with rate limitations, i.e. chemical non-equilibrium, one conceptual model that explains non-equilibrium is the distinction of the pore space into stagnant immobile regions and a mobile water content (van Genuchten et al. 1974), i.e. physical non-equilibrium. The fraction of mobile water is given by the factor β according to

$$\theta_m = \beta\theta \quad (2.21)$$

$$\theta_{im} = (1 - \beta)\theta = \tilde{\beta}\theta. \quad (2.22)$$

Based on mathematical formulations of Deans (1963), Coats and Smith (1964) derived a mathematical model using an exchange parameter ω to simulate diffusive exchange between these two regions, offering also analytical solutions (de Smedt and Wierenga 1979). The basic approach is given by replacing the source/sink function P by

$$P = -\partial_t \theta_{im} c_{im} \quad (2.23)$$

$$\partial_t \theta_{im} c_{im} = \omega(c_m - c_{im}). \quad (2.24)$$

which is similar to the description of kinetic sorption with a first-order model as presented in Equation (2.12).

2.1.5 Two-Site Two-Region Model

The concepts of dividing the kinetics of sorption sites at the solid phase into equilibrium and non-equilibrium and also dividing the pore water into mobile and immobile regions lead to two-site two-region models (van Genuchten and Wagenet 1989) that cover the main aspects of non-equilibrium solute transport. These models permit the reconstruction of many transport phenomena and led to a versatile application, e.g. in the numerical simulation software *HYDRUS* (Radcliffe and Šimůnek 2010; Šimůnek et al. 2013). As a

result, the following work is also based on the application of two-site two-region models following the constitutive equations:

$$\partial_t(\theta_m c_m + \beta(\rho_{\text{eq}}\sigma_m + \rho_{\text{neq}}\varsigma_m)) = \partial_x(\theta_m D \partial_x c_m - q c_m) - \omega(c_m - c_{\text{im}}) \quad (2.25)$$

$$\partial_t(\theta_{\text{im}} c_{\text{im}} + \tilde{\beta}(\rho_{\text{eq}}\sigma_{\text{im}} + \rho_{\text{neq}}\varsigma_{\text{im}})) = \omega(c_m - c_{\text{im}}) \quad (2.26)$$

$$\partial_t \sigma_m = \partial_t \phi(c_m) \quad (2.27)$$

$$\partial_t \sigma_{\text{im}} = \partial_t \phi(c_{\text{im}}) \quad (2.28)$$

$$\partial_t \varsigma_m = \alpha(\varphi(c_m) - \varsigma_m) \quad (2.29)$$

$$\partial_t \varsigma_{\text{im}} = \alpha(\varphi(c_{\text{im}}) - \varsigma_{\text{im}}). \quad (2.30)$$

2.1.6 Comparison to Interaction Kinetics in Completely Mixed Batch Reactors

To provide a comparability to the interaction kinetics observed in completely mixed batch reactor experiments, the previous equations can be solved under neglect of all transport processes. If, additionally, no equilibrium sorption sites and no immobile regions are assumed, Equation (2.25) reduces to

$$\theta \partial_t c = -\rho \partial_t \varsigma = -\rho \alpha(\varphi(c) - \varsigma), \quad (2.31)$$

and Equation (2.29) reduces to

$$\partial_t \varsigma = \alpha(\varphi(c) - \varsigma). \quad (2.32)$$

Assuming $c(0) = c^{\text{init}}$, $\varsigma(0) = 0$ and $\varphi(c) = K_d c$, these equations offer a convenient analytical solution according to

$$c(t) = \frac{c^{\text{init}}}{S} ((S - 1)e^{-\alpha S t} + 1), \quad (2.33)$$

where S is used as a sorption coefficient according to

$$S = 1 + \frac{\rho K_d}{\theta}. \quad (2.34)$$

This definition is closely related to R which is not used here to avoid confusion between the definition of R as relative transport velocity and this derivation, which is related to the mass balance of sorption. Only in case of equilibrium sorption this also results in a retardation of transport.

2.2 Dimensionless Parameters

A dimensionless parametrization is often used to compare column experiments carried out under different boundary conditions or with varying geometry. It combines the influence and interdependency of involved processes to decisive ratios or factors. The previous section lead to the derivation of the dimensionless parameter characterizing linear equilibrium adsorption as retardation R . Another prominent example is the utilization of the quasi-time scale exchanged pore volumes t_{pv} with the unit $[t_{pv}] = \text{pv}$. It represents the time which is necessary to exchange the amount of solute volume corresponding to the water-filled pore space (Toride et al. 1993). Therefore, the time t can be transformed to exchanged pore volumes t_{pv} by

$$t_{pv} = \frac{Qt}{\theta V_c} = \frac{qAt}{\theta LA} = \frac{vt}{L} \quad (2.35)$$

with A as the base area of the column and L as the length of the column. Experiments that are scaled to t_{pv} show the same BTC independent of the pumping rate or the mean pore water velocity if the porous medium exhibits the same dispersivity and no non-equilibrium processes that react to a different residence time in the column are involved. Differences in the BTC with respect to the dispersivity of the porous medium therefore become directly evident. Furthermore, an arbitrary column experiment with a conservative tracer and non-preferential, laminar flow shows the BCM at exactly at 1 pv, indicated by the inflection point for continuous-feed boundary conditions or the peak maximum for pulse-type boundary conditions. Thus, the scale can be interpreted intuitively with respect to the relative transport velocity, e.g. when the transport velocity is subjected to retardation due to sorption processes. A scaled space variable can also be defined in analogy by relating the space variable to the column length (Toride et al. 1993) following

$$z = \frac{x}{L}. \quad (2.36)$$

Another important example is the Péclet ($Pé$) number⁶, which characterizes the relation of advective fluxes and dispersive fluxes. The $Pé$ number is defined as

$$Pé = \frac{Lq}{\theta D} = \frac{L}{\lambda}. \quad (2.37)$$

The last transformation is only allowed when no molecular diffusion is present and therefore $D = D_h = \lambda v$. Then, the $Pé$ number becomes independent of the pumping rate. In general, column experiments carried out at the same $Pé$ number show the same spreading of concentration gradients in the BTC due to dispersion independent of the column geometry

⁶Named after Jean Claude Eugène Péclet (1793 - 1857), who introduced the number to generalize the characteristics of heat transfer (Péclet 1830).

(Bear 1988). It also indicates if the system is dominated by advection (high Pe) or by dispersion (low Pe).

The kinetics of sorption are represented by the Damköhler (Da) number⁷ given as

$$Da = \alpha\tau = \frac{\alpha LR}{v} = \frac{\alpha L}{v_t}, \quad (2.38)$$

constituting the product of the mass transfer coefficient α and the residence time in the column τ (e.g. Bahr and Rubin 1987). A value near unity represents situations, where the residence time equals the timescale of the mass transfer. High Da numbers indicate fast kinetics compared to the transport velocity, whereas low Da numbers show fast transport compared to the interaction rate.

The Da number can also be stated in terms of rate-limited exchange to immobile regions by replacing the mass transfer parameter from liquid solid interactions α with the mass transfer coefficient of exchange to immobile regions ω resulting in

$$Da = \omega\tau = \frac{\omega L}{v_t}. \quad (2.39)$$

The concept of Da numbers therefore applies to any kind of rate-limited interaction and transport behavior resulting from kinetic liquid solid interactions can also be expected from kinetic exchange to immobile regions.

Dimensionless formulations can be found for most variations of the ADE (van Genuchten and Wagenet 1989) by stating the derivatives with respect to the scaled variables and replacing the parameters with the dimensionless ratios. This helps in simplifying and generalizing analytical solutions. The results presented especially in the numerical part of this thesis will use dimensionless parameters for easy comparability.

⁷Named after Gerhard Damköhler (1908 - 1944), who introduced the number to generalize the characteristics of kinetics of chemical reactions (Damköhler 1936).

2.3 Evaluation of Mass Balances

2.3.1 General Mass Balance in Column Experiments

The total amount of a substance n_{tot} generally results from the integration over all involved compartments. In technical terms

$$n_{\text{tot}} = n_{\text{aqu}} + n_{\text{sorb}} + n_{\text{gas}}, \quad (2.40)$$

with the amount of substance in the aqueous phase n_{aqu} , adsorbed at the solid phase n_{sorb} and in the gas phase n_{gas} . The assumption is made that in column experiments, no incorporation of the tracer into the solid phase, i.e. the porous medium, occurs and the amount of substance in the solid phase is located chemically bound at the liquid solid interface. In case of laminar flow and under the assumption that each layer perpendicular to the flow direction is homogeneous, each compartment can be formulated as one-dimensional integral according to

$$n_{\text{aqu}} = \int_{\Omega} A\theta c \, d\Omega = \int_0^L A\theta c \, dx = A\theta \int_0^L c \, dx \quad (2.41)$$

$$n_{\text{sorb}} = \int_{\Omega} A\rho s \, d\Omega = \int_0^L A\rho s \, dx = A\rho \int_0^L s \, dx \quad (2.42)$$

$$n_{\text{gas}} = \int_{\Omega} A\eta \frac{p}{R_m \vartheta} \, d\Omega = \int_0^L A\eta \frac{p}{R_m \vartheta} \, dx = A\eta \frac{1}{R_m \vartheta} \int_0^L p \, dx, \quad (2.43)$$

where Ω is the spatial domain, η is the volumetric fraction of the gas phase, p is the partial pressure, R_m is the gas constant and ϑ is the temperature. The last transformation of the previous equations is not allowed when θ , ρ and η are not constant over x , i.e. when the porous medium is not homogeneously saturated or exhibits differences in the bulk density.

The closed-flow mode permits further statements of mass balances with respect to the temporal conservation of mass. In general, the initial amount of substances n and the water volume V equal their final state including possible losses from the aqueous phase following

$$n^{\text{init}} = n^{\text{end}} + n_{\text{loss}} \quad (2.44)$$

$$V^{\text{init}} = V^{\text{end}} + V_{\text{loss}}. \quad (2.45)$$

These formulations build the basis for all following mass balance analyses.

2.3.2 The Volumetric Dilution Factor

Totsche (2001) introduced the volumetric dilution factor d_v as a decisive parameter in closed-flow experiments. It is based on the observation that during a transport experiment,

the concentration of a tracer converges to a lower concentration due to dilution with tracer-free solution from within the porous medium. Under the assumption of a conservative tracer, n_{loss} can be eliminated from Equation (2.44). Furthermore, if initially the porous medium is completely free of the tracer and a solution with concentration c^{init} is filled in the mixing vessel with volume V_{mix} , the initial amount of substance n^{init} is solely given by the mixing vessel. Any following transport experiment leads to a final concentration c^{end} that is determined by the ratio of the volumes of the mixing vessel and the water-filled pore space, since the only process that leads to a decrease in concentration is the distribution of n^{init} over all aqueous compartments of the experimental setup.

As a result, each conservative breakthrough experiment in closed-flow mode shows a constant ratio of tracer solution at equilibrium c^{end} and tracer concentration provided with the mixing vessel initially c^{init} , which is the definition of the volumetric dilution factor d_v . The mathematical derivation of d_v from the mass balance in Equation (2.44) starts with

$$c^{\text{init}}V_{\text{mix}} = c^{\text{end}}V_t \quad (2.46)$$

$$c^{\text{init}}V_{\text{mix}} = c^{\text{end}}(V_{\text{mix}} + V_p + V_s) \quad (2.47)$$

$$c^{\text{init}}V_{\text{mix}} = c^{\text{end}}(V_{\text{mix}} + \theta V_c + V_s), \quad (2.48)$$

where V_t is the total water volume of the experiment, V_p is the water-filled pore volume, V_s is void space in tubing and the experimental setup that is not part of the porous medium and V_c is the volume of the column. A rearrangement and the definition that d_v equals the relative concentration observed after establishment of equilibrium yields

$$d_v = \frac{c^{\text{end}}}{c^{\text{init}}} = \frac{V_{\text{mix}}}{V_{\text{mix}} + \theta V_c + V_s}. \quad (2.49)$$

This shows that d_v can also be interpreted as fraction, from which the mixing vessel volume contributes to the total volume of the experiment and therefore describes the relative volume of the mixing vessel as a dimensionless parameter. Closed-flow experiments carried out with the same volumetric dilution factor that also share classical dimensionless parameters show the same BTC when scaled to exchanged pore volumes. Consequently, it is a dimensionless parameter that sufficiently describes the characteristics of closed-flow experiments. If an experimenter is given all instructions on applying a classical column experiment, the only additional information needed for an application of a corresponding closed-flow experiment is the value of d_v as it implicitly represents the mixing vessel solute volume.

2.3.3 Intrinsic Determination of the Water Content

The statement in Equation (2.49) has further implications regarding the water content. Since V_{mix} and V_c are usually known parameters of the experimental setup and d_v can easily be measured as the ratio of c^{end} and c^{init} , Equation (2.49) can be rearranged to

$$\theta V_c + V_s = \frac{V_{\text{mix}} - d_v V_{\text{mix}}}{d_v} \quad (2.50)$$

If V_s is known or can be neglected, this can be simplified further to

$$\theta = \frac{V_{\text{mix}} - d_v(V_{\text{mix}} + V_s)}{d_v V_c} \quad (2.51)$$

and θ can be calculated directly from involved volumes and the volumetric dilution factor. If V_s is unknown, an apparent water content θ_{app} can be defined as water content that would be detected, when V_s was part of the water-filled pore space of the column according to

$$\theta V_c + V_s = \theta_{\text{app}} V_c \quad (2.52)$$

This, in combination with Equation (2.50), leads to

$$\theta_{\text{app}} = \frac{V_{\text{mix}} - d_v V_{\text{mix}}}{d_v V_c} \quad (2.53)$$

If these equations are used for the determination of the water content, the difference between θ and θ_{app} has to be accounted for.

The strength in the derivation of Equation (2.53) lies in the independence from any aspects of transport, which offers the possibility of application to every closed-flow column experiment. The only condition that has to be fulfilled is the establishment of a stable equilibrium concentration that is not influenced by any process other than the mixture of solutes, which holds for conservative tracers.

2.3.4 Intrinsic Characterization of Sorption

The mass balance in Equation (2.44) also holds for reactive tracers which show chemical interactions at surfaces when the integration is extended appropriately. The term n_{loss} then represents the amount of substance which does not remain in the solution and is sorbed to a surface. If equilibrium sorption following a linear relationship of concentration

in the aqueous phase and concentration at the liquid solid interface is considered as given in Equation (2.13), the mass balance can be stated as

$$c^{\text{init}}V_{\text{mix}} = c^{\text{end}}V_t + sm_{\text{pm}} \quad (2.54)$$

$$c^{\text{init}}V_{\text{mix}} = c^{\text{end}}V_{\text{mix}} + c^{\text{end}}\theta V_c + c^{\text{end}}\rho K_d V_c \quad (2.55)$$

$$c^{\text{init}}V_{\text{mix}} = c^{\text{end}}V_{\text{mix}} + c^{\text{end}}V_c(\theta + \rho K_d) \quad (2.56)$$

$$\theta + \rho K_d = \frac{c^{\text{init}}V_{\text{mix}} - c^{\text{end}}V_{\text{mix}}}{c^{\text{end}}V_c} \quad (2.57)$$

$$\theta \left(1 + \frac{\rho K_d}{\theta}\right) = \frac{c^{\text{init}}V_{\text{mix}} - c^{\text{end}}V_{\text{mix}}}{c^{\text{end}}V_c}, \quad (2.58)$$

where m_{pm} is the solid mass of the porous medium. The volume of the setup V_s is neglected here. If it has to be considered, these statements can use the apparent water content θ_{app} according to Equation (2.52) instead of θ . Furthermore, $c^{\text{end}}/c^{\text{init}}$ is the observed dilution d in analogy to d_v , but in the general case of reactive transport. This simplifies Equation (2.58) to

$$S\theta = \frac{V_{\text{mix}} - dV_{\text{mix}}}{dV_c}. \quad (2.59)$$

A comparison to Equation (2.51) shows that S can be interpreted as a factor to the water content that has to be considered when the observed dilution d is not only influenced by the mixture of solutes, i.e. when $d_v \neq d$. If the statement in Equation (2.51) is inserted into Equation (2.59), this derivation finally yields

$$S = \frac{d_v(d-1)}{d(d_v-1)}. \quad (2.60)$$

The sorption coefficient S can therefore be determined by the knowledge of the relative dilution d_v expected for conservative transport, which is equal to the knowledge of the volumetric water content θ , and the actually observed relative dilution d .

2.3.5 Hypotheses Emerging from the Mass Balance

The occurrence of mass balances has important implications on the application of column experiments. A comprehensive comparison of mass balance derived parameters with numerical and experimental result is therefore presented based on the following hypotheses:

1. The volumetric dilution factor describes the additional experimental condition needed to sufficiently describe closed-flow experiments and therefore serves as a feasible reference parameter to compare experimental setups.

2. The intrinsic determination of the water content from BTC data in closed-flow experiments is unique, robust and practicable.
3. The intrinsic determination of sorbed mass from BTC data in closed-flow experiments is unique, robust and practicable.

These hypotheses are answered in subsection 5.1.1.

2.4 The Mixing Process in the Mixing Vessel

2.4.1 Derivation of the Constitutive Equation

The mixing vessel is the decisive factor in closed-flow experiments. It provides the influent boundary condition for the transport inside the column as it feeds the inflow and is responsible for the dilution observed in equilibrium depending on the mixing vessel volume. However, since it is also coupled to the outflow, the solution inside the mixing vessel is permanently mixed with effluent solution. Therefore, the concentration and chemical milieu is constantly driven in direction of the effluent. This generates a dynamic behavior of the mixing vessel solution and therefore also of the influent solution.

A closer look at the mixing process during a finite time step Δt in the interval $[t_i, t_i + \Delta t]$ shows that an amount of substance n_i is transported with the inflow and removed from the mixing vessel. During the same time, an amount of substance n_e enters the mixing vessel via the outflow. Thus, the discrete development of n_{mix}^i to n_{mix}^{i+1} can be stated as follows:

$$n_{\text{mix}}^{i+1} = n_{\text{mix}}^i - n_i + n_e \quad (2.61)$$

$$c_{\text{mix}}^{i+1} V_{\text{mix}} = c_{\text{mix}}^i V_{\text{mix}} - \overline{c_{\text{mix}}^i} Q \Delta t + \overline{c_e^i} Q \Delta t, \quad (2.62)$$

when the volumetric flux rates of inflow and outflow both equal Q , which is valid for saturated conditions or steady-state flow in unsaturated conditions. To fulfill the mass balance, overlined concentrations represent mean concentrations of mixing vessel and effluent, respectively, in the interval $[t_i, t_i + \Delta t]$ to account for their dynamic behavior. A rearrangement in direction of a difference quotient of concentrations leads to

$$c_{\text{mix}}^{i+1} = c_{\text{mix}}^i - \frac{Q \Delta t}{V_{\text{mix}}} (\overline{c_{\text{mix}}^i} - \overline{c_e^i}) \quad (2.63)$$

$$\frac{c_{\text{mix}}^{i+1} - c_{\text{mix}}^i}{\Delta t} = \frac{Q}{V_{\text{mix}}} (\overline{c_e^i} - \overline{c_{\text{mix}}^i}) \quad (2.64)$$

$$\frac{\Delta c_{\text{mix}}}{\Delta t} = \frac{Q}{V_{\text{mix}}} (\overline{c_e^i} - \overline{c_{\text{mix}}^i}). \quad (2.65)$$

This is valid for all c_{mix}^i in the duration of the experiment $(0, T)$ and therefore can be formulated for $\Delta t \rightarrow 0$ as

$$\partial_t c_{\text{mix}} = \frac{Q}{V_{\text{mix}}} (c_e - c_{\text{mix}}), \quad (2.66)$$

since $\overline{c_{\text{mix}}^i}$ and $\overline{c_e^i}$ can be regarded as identical to c_{mix}^i and c_e^i , respectively, for $\Delta t \rightarrow 0$. The last statement builds the basis for a mathematical evaluation of closed-flow experiments owing to the mechanistic description of the development of concentration in the mixing vessel.

An important implication from Equation (2.66) is the inherent information about the effluent concentration. If either c_e or c_{mix} is measured, both can be transformed to each other via an appropriate rearrangement of Equation (2.66). Hence, a direct measurement of the effluent is not necessary when the mixing vessel concentration is recorded or vice versa. The effluent BTC is given as

$$c_e = c_{\text{mix}} + \frac{V_{\text{mix}}}{Q} \partial_t c_{\text{mix}} \quad (2.67)$$

and the mixing vessel BTC is calculated from the effluent according to

$$c_{\text{mix}}(t) = e^{-\frac{Qt}{V_{\text{mix}}}} \left(c_{\text{mix}}^{\text{init}} + \int_0^t \frac{Q}{V_{\text{mix}}} e^{\frac{Qt'}{V_{\text{mix}}}} c_e(t') dt' \right). \quad (2.68)$$

2.4.2 Approximations for Special Cases

The Initial Exponential Decrease

The development of the concentration in the mixing vessel as presented in Equation (2.66) permits analytical solutions for certain boundary conditions. In the most general situation, a breakthrough experiment is carried out with a column initially at constant background and a defined amount of substance in the mixing vessel. This leads to a dilution of tracer solution inside the mixing vessel with the effluent solution at constant concentration in the beginning of an experiment until the moment of first tracer breakthrough. During this time, Equation (2.66) can be solved under the assumptions that $c_e = c_e^{\text{init}}$ and $c_{\text{mix}}(0) = c_{\text{mix}}^{\text{init}}$ to

$$c_{\text{mix}} = c_e^{\text{init}} + (c_{\text{mix}}^{\text{init}} - c_e^{\text{init}}) e^{-\frac{Qt}{V_{\text{mix}}}} \quad (2.69)$$

This simplifies to

$$c_{\text{mix}} = c_{\text{mix}}^{\text{init}} e^{-\frac{Qt}{V_{\text{mix}}}} \quad (2.70)$$

when the column is initially free of tracer. The exponential decrease described here represents the infinitesimal mixing process. However, the application of this equation is restricted to the duration before the onset of the tracer breakthrough, e.g. when $t \leq 0.5 \text{ pv}$ to ensure the validity of the assumptions regarding the effluent concentration. As the initial concentration as well as the volume of the mixing vessel are usually known boundary parameters of the experimental setup and c_{mix} represents the BTC, the only unknown in Equation (2.70) is Q . This implies that the pumping rate can be determined from the measurement of the BTC using the first part of the exponential dilution. Since no transport processes can interfere with the shape of the initial dilution in case of laminar

non-preferential transport, this observation is indicative only for the pumping rate, allowing an independent determination of Q , e.g. via nonlinear regression.

The First Oscillation Maximum

In open-flow mode, some handy ways of estimating the BCM as representation of the retardation from shape measures, e.g. the inflection point, allow for a quick survey of the transport regime. However, this is not possible in closed-flow mode experiments since the shape of the BTC is completely altered into oscillations. To maintain the option of a fast estimation of the BCM and therefore reveal possible retardation, another indicative BTC feature has to be used. Because of the multiple passage of tracer solution through the column, Totsche (2001) expected the wavelength to be a solid indication for the BCM. The BTC feature most suitable for the determination of the oscillation wavelength is the easily observable position of the oscillation maximum. However, the passage of the tracer through the mixing vessel has to be considered as well, resulting in the appearance of the first and the following maxima at $t_{pv} > 1$ pv. The wavelength should therefore be interpreted as related to the BCM of the system including the mixing vessel instead of being related only to the porous medium (Ritschel 2011). Still, the first oscillation maximum is an obvious and easily detectable feature of a BTC obtained in closed-flow mode that is strongly related to the BCM.

As a potential way to handle the issue of tracer passage through the mixing vessel volume, this subsection presents a way to estimate the BCM based on the observation of the first oscillation maximum. To include the influence of the mixing vessel volume on the position of the oscillation maximum, a similar approach of approximating Equation (2.66) as shown for the determination of the pumping rate is used. In the derivation, the influence of diffusion and dispersion is neglected, since their effect on the position of the first oscillation maximum is negligible for $Pé$ numbers greater unity (Ritschel 2011). Consequently, the following approach is inapplicable at diffusion dominated systems. At this point the reader may be reminded of the fact that the following derivation is intended to estimate the position of the oscillation maximum and not to represent solute transport, where a neglect of diffusion/dispersion would be absurd.

For reasons of simplification and comparability, the space relative to column length z is used as spatial scale and the temporal scale is represented by the amount of exchanged pore volumes t_{pv} . The relation of water-filled pore space inside the column and mixing vessel volume is constituted by the coefficient k defined as

$$k = \frac{\theta V_c}{V_{\text{mix}}} \quad (2.71)$$

to simplify the following formulas. An adequate representation of Equation (2.66) is then given as

$$\partial_{t_{pv}} c_{\text{mix}} = k(c_e - c_{\text{mix}}). \quad (2.72)$$

Under neglect of diffusion and dispersion, it can be assumed that the effluent is free of tracer until the exchange of 1 pv multiplied by retardation. As a result, the concentration in the mixing vessel is not influenced by the breakthrough of the tracer and is solely subjected to exponential dilution (Figure 2.1 a). Since these assumptions are only valid in $t_{pv} = [0, R]$, the BTC is divided into multiple phases, each representing one particular passage of tracer solution through the column. Following that, the corresponding first phase of the BTC with solely exponential dilution is denoted as c_1 . This phase is followed by successive definitions of the development of concentration in the mixing vessel c_n , each defined in $t_{pv} = [(n-1)R, nR]$. Under the assumptions mentioned above, Equation (2.72) can be solved for $n = 1$ with $c_e = 0$ and $c_1(0) = c_{\text{mix}}^{\text{init}}$ to

$$c_1 = c_{\text{mix}}^{\text{init}} e^{-kt_{pv}}. \quad (2.73)$$

At $t_{pv} = R$, the tracer has traveled through the column once and the mixing vessel starts to mix with effluent solution containing tracer. A further consideration of the BTC in the mixing vessel therefore demands for an estimation of effluent concentration for $t_{pv} \geq R$. The neglect of diffusion and dispersion proves very useful here, since the spatial distribution in the column at $t_{pv} = R$ exactly reflects what has been feed with the inflow (Figure 2.1 b). As a result, $c(z)$ mirrors $c_1(t_{pv})$ (compare Figure 2.1 a and Figure 2.1 b), because each z represents the distance a tracer is transported in the corresponding time in terms of t_{pv} . This connection implies that the effluent concentration in the second phase of the breakthrough can be represented in terms of the mixing vessel concentration in the first phase $c_1(t_{pv})$. According to this, the solution for the next phase of the BTC in the mixing vessel is obtained by assuming $c_e(t_{pv} + R) = c_1(t_{pv})$. To correct for the shift in the function argument, \hat{c}_1 is defined as c_1 shifted by one retardation, so that $c_1(t_{pv} - R) = \hat{c}_1(t_{pv}) = c_e(t_{pv})$. An appropriate formulation of Equation (2.66) then yields

$$\partial_{t_{pv}} c_2 = k(\hat{c}_1 - c_2). \quad (2.74)$$

Since the development of mixing vessel concentration is continuous and thus, the phases defined in this derivation intersect at all nR , it is necessary that $c_2(R) = c_1(R) = c_{\text{mix}}^{\text{init}} e^{-kR}$. When solving Equation (2.74), this leads to

$$c_2 = c_{\text{mix}}^{\text{init}} e^{-kt_{pv}} (1 + ke^{kR}(t_{pv} - R)). \quad (2.75)$$

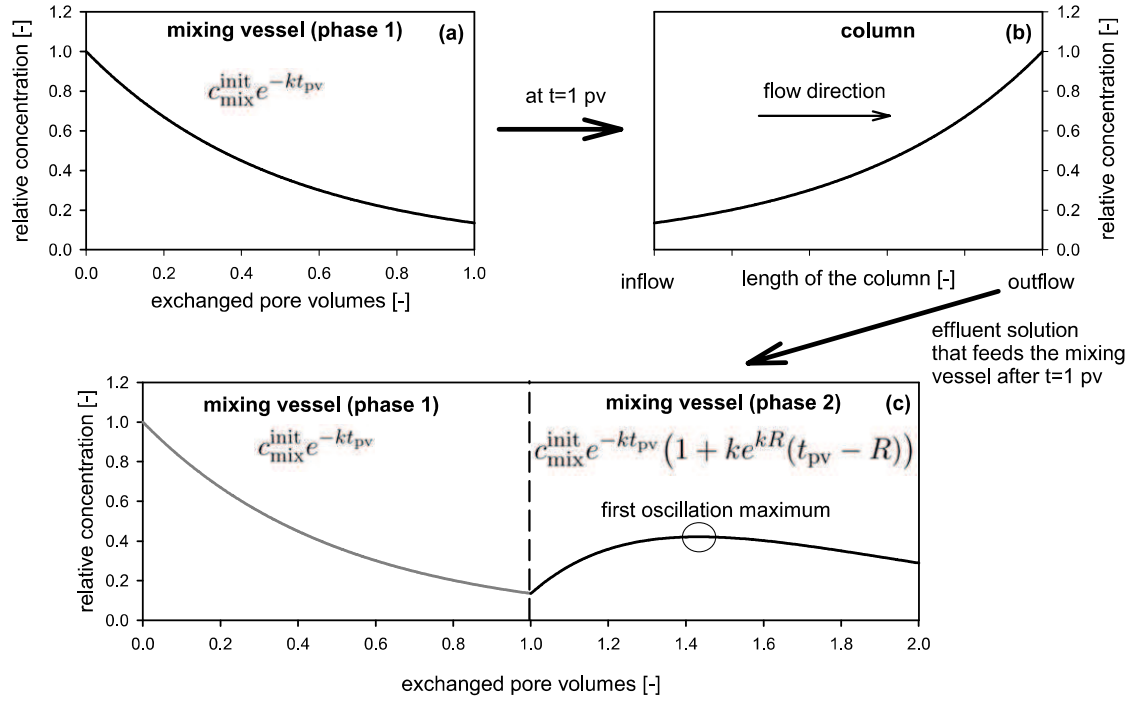


Figure 2.1: Scheme of the derivation of the analytical description of the first oscillation maximum of the BTC in the mixing vessel at $R = 1$ and $k = 2$, (a) shows the exponential dilution in the mixing vessel to be expected while the tracer travels through the column and tracer-free solution is carried with the effluent, (b) shows the distribution of tracer inside the column resulting from this course of concentration in the mixing vessel after the exchange of 1 pv, (c) shows the first oscillation that is to be expected in the mixing vessel when a distribution described by (b) exits the column via the effluent.

If this procedure is continued for the next phases in an analogous way, a pattern emerges and a generalization can be formulated as

$$c_n = c_{\text{mix}}^{\text{init}} e^{-kt_{\text{pv}}} \sum_{m=0}^{n-1} \frac{k^m}{m!} e^{kmR} (t_{\text{pv}} - mR)^m. \quad (2.76)$$

This equation is somewhat related to the Taylor series of a function $f(x)$ expanded at point a , which is defined as

$$T_{f(x)}(a) = \sum_{m=0}^{\infty} \frac{f^{(m)}(a)}{m!} (x - a)^m \quad (2.77)$$

The solution of the solute transport behavior in the mixing vessel described in Equation (2.76) shows some major similarities here. The m -th derivative of $f(t) = e^{kt}$ yields $f^{(m)}(t) = k^m e^{kt}$. The expansion point $a = mR$ represents the phase in which the breakthrough is evaluated to the $(n - 1)$ -th term. The whole series is scaled by the initial concentration $c_{\text{mix}}^{\text{init}}$ and exponentially damped by $e^{-kt_{\text{pv}}}$.

To reconsider the search for the oscillation maximum, an investigation of c_n reveals that the first maximum is always found in the second phase ($n = 2$) represented by Equation (2.75) (Figure 2.1 c). A straight forward way to analyze Equation (2.75) with respect to maxima is to calculate the root of the first derivative. The derivative of Equation (2.75) is

$$\partial_{t_{pv}} c_2 = c_{mix}^{init} k e^{-kt_{pv}} \left(e^{kR} (k(R - t_{pv}) + 1) - 1 \right), \quad (2.78)$$

which dramatically simplifies when the root is calculated as

$$t_{pv}^{max} = \frac{1 - e^{-kR}}{k} + R. \quad (2.79)$$

The last step is the rearrangement of Equation (2.79) with respect to R . Due to the exponential term a linear transformation is not possible and the Lambert-W-function (Barry et al. 2000) has to be applied. The final result is then

$$R = \frac{W(e^{-kt_{pv}^{max}+1}) - 1}{k} + t_{pv}^{max}. \quad (2.80)$$

With this approach, the retardation can be estimated from the first oscillation maximum t_{pv}^{max} corrected by the influence of the mixing vessel volume represented by k .

2.4.3 Hypotheses Emerging from the Mixing Process

The mixing vessel is the most important boundary condition in closed-flow experiments. Therefore, an exhaustive investigation of the influence of the mixing vessel on solute transport was conducted experimentally and numerically based on following hypotheses

1. Equation (2.66) fully describes the temporal course of concentration in the mixing vessel and therefore can serve as model for the inflow boundary condition.
2. The solute volume of the mixing vessel decisively impacts the shape of the BTC, the establishment of equilibrium and the type of inflow boundary condition.
3. The approximation of Equation (2.66) presented in order to derive the volumetric pumping rate Q is applicable.
4. The approximation of Equation (2.66) presented in order to derive the retardation R is applicable despite the neglect of dispersion.
5. The BTC obtained from measurements in the mixing vessel contains the same information as the BTC measured in the effluent.

These hypotheses are answered in subsection 5.1.2.

2.5 Comparison to a Damped Harmonic Oscillator

2.5.1 Conceptual Approach

The appearance of concentration oscillations implies the close relation to a physical harmonic oscillator, e.g. a spring. A conceptual reduction to the essential aspects of such a physical system leads to the following conditions needed to be considered a harmonic oscillator:

1. A force, that drives the system towards an equilibrium
2. This force is proportional to the distance between system state and equilibrium
3. The system shows an inertia resulting in an overshoot when approaching the equilibrium with a high “velocity”

These characteristics also somewhat apply for closed-flow experiments. The “force” that drives the system towards an equilibrium with respect to partitioning, adsorption and similar chemical interactions with the solid phase is represented by the concentration gradient inside the column and with respect to the mixing vessel. The magnitude of these gradient decides on the strength of transport processes, which approximately covers the second requirement. The processes leading to the “inertia” is transport in general and the mixing process in the mixing vessel and dispersion inside the column, in the broadest sense all processes that exhibit a time-delay. In this (rather vague) sense, a closed-flow experiment can be considered a harmonic oscillator and the BTC is the analogy to the trajectory of the oscillator evolving over time. To review if also the mathematical description of the physical harmonic oscillator can be applied to closed-flow experiments, a derivation of the motion of a spring is given below.

The basic law describing a spring is Hooke’s law:

$$F = -k_s x \quad (2.81)$$

Combined with Newton’s second law of motion

$$F = ma = m d_t^2 x \quad (2.82)$$

the basic formulation of a harmonic oscillator can be derived as

$$m d_t^2 x = -k_s x. \quad (2.83)$$

For any real physical system, friction causes movement to slow down, ultimately leading the system to stop. In case of a physical spring, the oscillations diminish and a stable

position is reached. The strength of friction can be modeled as proportional to the velocity written as

$$F = -C d_t x. \quad (2.84)$$

The addition of this to Equation (2.83) yields

$$m d_t^2 x + C d_t x + k_s x = 0 \quad (2.85)$$

to describe a damped harmonic oscillator (Bartelmann et al. 2015). This is usually rewritten as

$$d_t^2 x + 2\zeta\omega_0 d_t x + \omega_0^2 x = 0, \quad (2.86)$$

where $\omega_0 = \sqrt{\frac{k_s}{m}}$ is considered the undamped angular frequency and $\zeta = \frac{C}{2\sqrt{mk_s}}$ represents the damping ratio (Bartelmann et al. 2015). The latter parameters decides on the general behavior of the oscillator.

1. $\zeta < 1$ (*underdamped case*): The damping is relatively low compared to the spring force acting on the mass, which results in an overshoot when approaching the equilibrium, appearing as oscillations.
2. $\zeta = 1$ (*critical damping*): The system returns to equilibrium as fast as possible without showing oscillations
3. $\zeta > 1$ (*overdamped case*): The damping is strong enough to suppress oscillations and additionally delays the establishment of equilibrium

Depending on the specific case, Equation (2.86) offers several analytical solutions. Due to the relevance for closed-flow experiments, the following example only discusses the oscillating case for $\zeta < 1$. A convenient analytical solution for this scenario (Bartelmann et al. 2015) is given by

$$f(t) = \Gamma e^{-\zeta\omega_0 t} \sin(\sqrt{1 - \zeta^2} \omega_0 t + \Phi) + f_{eq} \quad (2.87)$$

The function f used here represents the position of the spring and equilibrium is reached when $f(t)$ equals f_{eq} . The parameters Γ and Φ are the initial amplitude and the phase of the oscillation, respectively. The separation into the exponential part and the sinusoidal part offers an intuitive interpretation of Equation (2.87). The damping is represented by the exponentially decreasing first part that converges to zero and the oscillations are shown in the sine function in the second part.

A transfer of this model to a closed-flow experiment can be achieved by interpreting $f(t)$ as concentration over time, i.e. $c(t)$. This requires the assignment of the initial

concentration instead of the initial amplitude and the replacement of f_{eq} with the final concentration to which the experiment converges to, resulting in

$$c(t) = \Gamma e^{-\zeta\omega_0 t} \sin(\sqrt{1 - \zeta^2} \omega_0 t + \Phi) + c^{\text{end}} \quad (2.88)$$

One very interesting aspect encountered here is the appearance of a reduced frequency at which the system oscillates due to damping calculated as $\omega_d = \sqrt{1 - \zeta^2} \omega_0$ (Bartelmann et al. 2015). Hence, the damping ratio reduces the observed frequency. Transferred to closed-flow experiments, this implies that the observed wavelength is not only governed by the transport velocity of the solute, but also changes depending on the damping.

2.5.2 Hypotheses Emerging from the Harmonic Oscillator

The most suggestive connections between harmonic oscillators and closed-flow experiments will be investigated by the application of the presented model to BTC data from column experiments and are formulated as hypotheses as follows:

1. The model describing harmonic oscillators is applicable and allows the interpretation of experimental results in terms of the model.
2. The damping of the harmonic oscillator is strongly related to the mixing in the mixing vessel and the dispersion.
3. There is a fundamental wavelength corresponding to the undamped angular frequency ω_0 that is solely dependent on the transport velocity and the differences in observed wavelength are a result of damping, which causes an effective damped angular frequency ω_d .

These hypotheses are answered in subsection 5.1.3.

2.6 Evaluation of Measured BTCs

2.6.1 Concept of Transfer Functions

A prominent approach in describing the process of transport is utilizing the mathematical concept of convolution (Jury and Roth 1990; Koestel et al. 2011). The operator corresponding to convolution is “*”, which is not to be confused with the multiplication operator “.”. A convolution of two functions f and g into h is defined as

$$h = f * g = g * f = \int_{-\infty}^{\infty} f(x')g(x - x') dx' = \int_{-\infty}^{\infty} f(x - x')g(x') dx'. \quad (2.89)$$

Convolution can be imagined as an alteration of input g by applying the impulse response function f to it. An easy example is the blurring of an 2D image via a so-called “Gaussian Kernel”, which assigns each pixel of the new image a mean value of surrounding pixels of the original image, weighted based on a 2-dimensional Gaussian distribution. The process of pixel averaging appears as blurring to the observer. In that context, the input would be the unblurred image, the impulse response is represented by the centered Gaussian distribution and the blurred image is the result of convolution.

In context of solute transport, also an open-flow column experiment can be considered in the framework of transfer functions. The input signal is given by the course of concentration of the solution in the supply vessel. The transport through the column “convolves” this input depending on the specific transport parameters to what can be measured as temporal course of concentration of effluent solution, i.e. the BTC. A reformulation of Equation (2.89) in terms of column experiments is then given by

$$c_e = f_{\text{pm}} * c_{\text{in}} \quad (2.90)$$

Each experimental setup including the characteristics of the porous medium can be represented by an associated impulse response function, which contains all transformations of the input signal due to, e.g., advection, diffusion or chemical reactions. This function can also be considered the travel-time probability density function (PDF) of the porous medium since it represents the probability which travel-time is taken by a single molecule from a pulse input. Thus, the integral of f_{pm} is unity according to

$$\int_{-\infty}^{\infty} f_{\text{pm}} dt = 1. \quad (2.91)$$

As a result, the full analytical reconstruction of this function equals the identification of transport parameters. To achieve this, three steps are necessary

1. Measurement of data corresponding to the impulse response function f_{pm} of the porous medium.

2. Finding a parameterized, analytical description of $f_{\text{pm}} \equiv$ constructing a model.
3. Fitting this function to the presumably noisy data to obtain a set of parameters.

To avoid any confusion, the term transfer function is only used conceptually in this section since it is defined as Laplace transform of the impulse response in signal processing and also used as description of the whole convolution integral in context of transport (Jury and Roth 1990). Both definitions are somewhat related but refer to a different aspect of this concept. In order to understand how this concept also applies to closed-flow column experiments, some further explanations are given in the following subsections.

Measurement of the Travel-Time PDF

As already described, the usual observation in column experiments is the BTC as a result from transport processes and the temporal course of influent solution. Therefore, the impulse response is not observable directly and Equation (2.90) has to be inverted. This operation is referred to as deconvolution and the BTC has to be “deconvolved” with the input signal in order to derive the impulse response function. As time is the independent variable for BTCs, the following functions are defined in t . In general, deconvolution is mathematically complicated and usually results in non-unique solutions. Therefore, the determination of impulse response functions is often carried out at advantageous boundary conditions. One way is offered by the neutral element in convolution, which is the Dirac delta function δ , implying that

$$f * \delta = f. \quad (2.92)$$

As a result, if either the input signal in Equation (2.89) or the impulse response function can be considered an approximation of δ , the convolution leaves the other function unaffected. Since the impulse response function is given by the setup and is not likely close to a Dirac delta function, the experimenter has to apply a Dirac like solute pulse to the influent instead. To ensure the mass balance, the associativity with respect to scalar multiplication in convolution allowing statements such as

$$f * (ag) = a(f * g) \quad (2.93)$$

can be used to scale the Dirac pulse accordingly leading to a likewise scaling of the result from convolution. After application of the solute pulse, the transport through the column “convolves” this scaled pulse to the BTC, which now exactly resembles the impulse response function scaled by the initial solute pulse as resulting from Equation (2.90), Equation (2.92) and Equation (2.93).

In the literature, besides a Dirac like solute pulse, a frequent influent boundary condition is a continuous-feed or step input. This temporal course of influent solution also shows an uncomplicated behavior when adapting the concept of convolution. The substitution of the function representing the input signal with the Heaviside step function H defined as

$$H(t) = \begin{cases} 0, & t < 0 \\ \frac{1}{2}, & t = 0 \\ 1, & t > 0 \end{cases} \quad (2.94)$$

can be applied for a proper representation of the continuous-feed boundary condition. Another property of H is the relation to the Dirac delta function δ , which is the derivative of H according to

$$d_t H = \delta. \quad (2.95)$$

This relation is sometimes found instead of Equation (2.94) as the definition of H . The evaluation of experiments run under a boundary condition described by H exploits the differentiation rule of convolution stating that

$$d_t(f * g) = f * d_t g. \quad (2.96)$$

Subsequent integration yields

$$f * g = \int f * d_t g dt. \quad (2.97)$$

Replacing g with H and using the relation to the Dirac delta function results in

$$f * H = \int f * \delta dt. \quad (2.98)$$

$$f * H = \int f dt. \quad (2.99)$$

This implies that convolution with a Heaviside function acts as an integral operator (Gilbert and Nicholson 2004). In the context of column experiments, if a continuous-feed is applied to the system, the transport through the column “convolves” the input into a BTC that is identical to the integral of the impulse response function, also referred to as step response function. Again, an appropriate scaling using Equation (2.93) is needed to fulfill mass balances. The BTC can therefore be considered a scaled travel-time cumulative distribution function (CDF) and the actual impulse response function is obtained by scaling and calculating the derivative. However, this operation is sensitive to small variation in the data and might intensify noise.

An Analytical Expression of the Travel-Time PDF

In order to retrieve transport parameters from the measurement of the BTC, an analytical expression of the impulse response function has to be derived. Depending on the conceptual model, the boundary condition and the complexity of involved transport processes, numerous expressions can be derived. Jury and Roth (1990) present an exhaustive compilation of different scenarios and solutions. Most prominently, impulse response functions based on the ADE result in Gaussian shape PDFs or CDFs via Laplace transformation. As an example, an impulse response function describing one-dimensional advection and dispersion through a column is given as

$$f_{\text{pm}} = \frac{L}{2\sqrt{\pi Dt^3}} e^{-\frac{(L-vt)^2}{4Dt}}. \quad (2.100)$$

This expression can also be used to calculate forward predictions on the expected effluent BTC for all types of inflow boundary conditions, most generically formulated as the convolution integral

$$c_f(t) = \int_{-\infty}^t c_{\text{in}}(t-t') \frac{L}{2\sqrt{\pi Dt'^3}} e^{-\frac{(L-vt')^2}{4Dt'}} dt'. \quad (2.101)$$

This derivation only considers advection and broadening of concentration gradients due to diffusion and dispersion, combined as apparent dispersion coefficient D here. For each additional process, another analytical expression is needed. Specific analytical solutions are, e.g. available for formulations of the ADE including kinetic sorption (Lindstrom and Boermsma 1973; van Genuchten and Wierenga 1976) or zero-order production and first-order decay (van Genuchten 1981a). For the purpose of validating numerical implementations, analytical solutions of the ADE as presented in Equation (2.101) offer a reliable tool to calculate reference BTCs. However, special care has to be taken on the application of Equation (2.101) since c_f represents flux concentrations. In numerical models, often the resident concentration c_r is given. In these cases, c_f has to be calculated from c_r (Jury and Roth 1990) according to

$$c_f = c_r - \frac{D}{v} \partial_x c_r. \quad (2.102)$$

The discussion on transfer functions in closed-flow experiments will refer to the convolution integral shown in Equation (2.101).

2.6.2 Fitting of Models to Measurements

A huge variety of fitting algorithms are available. The general approach of fitting can be described as adjusting the shape of a simulated or calculated graph in order to resemble

the shape of a measured curve, often referred to as regression. The simulated curve results from the theoretical and parameterized model that is designed to image the involved processes and reconstruct what has been measured. The parameters are then changed until a minimal difference of model and measurement is found. The parameter values can then be interpreted as they carry a physical meaning if the underlying model assumptions are valid. In the literature, this method is often referred to as optimization, which is defined as finding the optimal set of parameters with respect to the minimization of an “objective function”. A comprehensive overview of parameter estimation in context of solute transport is given in Kool et al. (1987) and in Franssen et al. (2009) or Zhou et al. (2014) for general hydrology.

Most prominently, the least-squares solution, i.e. the least sum of squared residuals between observation and model, is considered the most probable solution and therefore often used as objective function. The algorithms to find the set of parameters satisfying this condition vary in speed and convergence. A widely applied method for generic curve fitting is the Levenberg-Marquardt algorithm⁸. However, as for all gradient based methods, only local optima are found. This presumes a convex surface of the objective function for a successful determination of meaningful parameters. Especially for high-dimensional problems, this assumption is usually not valid and global optimization strategies have to be applied. Interestingly, many of these methods mimic behavior observed in nature, where systems converge to complex optima of various boundary conditions. As an example, biological evolution creates species, that are adapted to their environment with astonishing precision. Also abiotic systems show complicated optimization, e.g. the growth of crystals along lattice plains according to the thermodynamical properties. The core idea of these algorithms is the ability to accept worse solutions temporarily with a certain probability in order to avoid getting stuck in local minima. An overview of global optimization methods and the recent development of algorithms is given in Floudas and Gounaris (2009). The Levenberg-Marquardt algorithm as a local optimization strategy and the simulated annealing algorithm as an example for global optimization are introduced in the next section since their wide application throughout this thesis.

Objective Function

The general objective function O assuming independent variables \mathbf{x} and dependent variables \mathbf{y} resulting in datum pairs of (x_i, y_i) is defined as follows

$$O_l(\boldsymbol{\varpi}) = \sum_{i=1}^I |y_i - f(x_i, \boldsymbol{\varpi})|^l, \quad (2.103)$$

⁸Named after Kenneth Levenberg (1919-1973) and Donald W. Marquardt (1929-1997), who introduced this algorithm (Levenberg 1944; Marquardt 1963).

where $f()$ is a general model operator converting the independent variable into the dependent variable based on the set of parameters $\boldsymbol{\varpi}$ used in the model and i is the index used to screen all I data point. The exponent l defines the norm of the objective function. For $l = 2$, the sum of squared residuals is calculated and referred to as l_2 -norm, whereas with $l = 1$, the l_1 -norm is defined as the sum of absolute residuals. Latter is sometimes used if the l_2 -norm produces artifacts due to the overvaluation of outliers in the data. The function $O_l(\boldsymbol{\varpi})$ represents a general measure for the deviation of measurement and model and is subjected to minimization in parameter optimization, since it approaches zero for decreasing residuals, independent of the applied norm.

A closely related concept is the coefficient of determination R^2 that places the l_2 -norm in relation to the variation in the data. In this way, an intuitive range of possible values from 0, in cases where none of the variation in the data is explained by the model, to 1, where the model perfectly fits the data, is created. R^2 is defined as

$$R^2 = 1 - \frac{\sum_i (y_i - f(x_i, \boldsymbol{\varpi}))^2}{\sum_i (y_i - \bar{y})^2} = 1 - \frac{O_2(\boldsymbol{\varpi})}{\sum_i (y_i - \bar{y})^2} \quad (2.104)$$

Levenberg-Marquardt algorithm

The Levenberg-Marquardt algorithm is an extension of the Gauss-Newton method applied to the context of modeling (Levenberg 1944; Marquardt 1963). It is based on Newton's iterative method of finding the root of a function. The basic iteration can be stated as

$$\boldsymbol{\varpi}^{i+1} = \boldsymbol{\varpi}^i - \mathbf{H}^{-1} \mathbf{g} \quad (2.105)$$

$$\Delta \boldsymbol{\varpi} = -\mathbf{H}^{-1} \mathbf{g}, \quad (2.106)$$

where \mathbf{H} is the Hessian matrix, \mathbf{g} is the gradient vector and $\Delta \boldsymbol{\varpi}$ is the supplement to $\boldsymbol{\varpi}$ for the next iteration. When calculating an update to the parameter set according to Equation (2.106), the calculation of \mathbf{H} is computationally inefficient and prone to instabilities. For this reason, the first-order Taylor approximation of \mathbf{H} following

$$\mathbf{H} \approx 2\mathbf{J}'\mathbf{J} \quad (2.107)$$

is used instead. Here, the Jacobi matrix \mathbf{J} defined as gradient of the model at each independent variable with respect to the model parameters according to

$$\mathbf{J}_{i,j} = \frac{\partial f(x_i, \boldsymbol{\varpi})}{\partial \boldsymbol{\varpi}_j} \quad (2.108)$$

with i and j indexing I data points and J parameters, respectively, is utilized due to its easy computability. This approximation is usually not problematic since the algorithm is based on iteration and errors due to approximation are eliminated in later iterations.

With Equation (2.107) and the relation that the gradient vector \mathbf{g} can also be represented in terms of the Jacobian matrix according to

$$\mathbf{g} = -2\mathbf{J}'(\mathbf{y} - \mathbf{f}(\boldsymbol{\varpi})), \quad (2.109)$$

an update rule to the initial guess of parameters $\boldsymbol{\varpi}$ is derived from Equation (2.106) as

$$\Delta\boldsymbol{\varpi} = (\mathbf{J}'\mathbf{J})^{-1}\mathbf{J}'(\mathbf{y} - \mathbf{f}(\boldsymbol{\varpi})). \quad (2.110)$$

This is called a Gauss-Newton scheme for the minimization of $O_2(\boldsymbol{\varpi})$ showing a quadratic rate of convergence. However, if the guessed parameter set $\boldsymbol{\varpi}$ is far away from the optimum, this method is prone to divergence sometimes resulting in an increase of $O_2(\boldsymbol{\varpi})$. For this reason, the Levenberg-Marquardt algorithm extends the update rule by introducing the Levenberg-Marquardt parameter γ and the identity matrix \mathbf{I} resulting in

$$\Delta\boldsymbol{\varpi} = (\mathbf{J}'\mathbf{J} + \gamma\mathbf{I})^{-1}\mathbf{J}'(\mathbf{y} - \mathbf{f}(\boldsymbol{\varpi})). \quad (2.111)$$

If no decrease in the objective function can be achieved with Equation (2.110), γ is successively increased, pronouncing the influence of the identity matrix. For large γ , the term $(\mathbf{J}'\mathbf{J} + \gamma\mathbf{I})^{-1}$ converges to γ^{-1} , and the update vector is given by

$$\Delta\boldsymbol{\varpi} = \gamma^{-1}\mathbf{J}'(\mathbf{y} - \mathbf{f}(\boldsymbol{\varpi})), \quad (2.112)$$

which represents the direction of the steepest descent resulting definitely in a reduction of $O_2(\boldsymbol{\varpi})$, if not already in a minimum. For this reason, γ is increased until a “safe” update rule is obtained. As the steepest descent iteration shown in Equation (2.112) shows only slow convergence, the algorithm decreases γ on a successful step, to check if the Gauss-Newton direction is reliable again. In this way, the stability of the steepest descent algorithms with the rate of convergence of the Gauss-Newton algorithm is combined and virtually all local optimization problems can be solved conveniently.

After an optimum is found, parameter uncertainty is approximated by assuming that \mathbf{J} is constant around the optimum. Hence, the covariance matrix can be calculated as

$$C(\boldsymbol{\varpi}) = \sigma^2(\mathbf{J}'\mathbf{J})^{-1} = \frac{O_2(\boldsymbol{\varpi})}{I - J}(\mathbf{J}'\mathbf{J})^{-1}. \quad (2.113)$$

Consequently, the confidence interval is approximated by

$$\Delta\boldsymbol{\varpi}_j = t_{I-J, 0.975} \sqrt{C(\boldsymbol{\varpi})_{jj}} \quad (2.114)$$

with t as the student-t distribution with $I - J$ degrees of freedom and 5% significance.

Simulated Annealing

A very prominent global optimization algorithm is called simulated annealing. Basically it is a Metropolis algorithm⁹ that combines Markov-Chain-Monte-Carlo methods¹⁰ with the Maxwell-Boltzmann distribution following

$$P(E) \propto e^{-\frac{E}{k_b \vartheta}} \quad (2.115)$$

Here $P()$ is considered the probability, at which a particle carries the energy E at constant temperature ϑ . The probability ratio of two states evaluates the relative probability rather than the absolute one and can be expressed explicitly as

$$\frac{P(E_2)}{P(E_1)} = e^{-\frac{\Delta E}{k_b \vartheta}} \quad (2.116)$$

since the coefficient of proportionality needed for a proper analytical expression of Equation (2.115) is eliminated. This ratio is called the Boltzmann factor. The Metropolis algorithm exploits this in order to generate draws from a distribution described by Equation (2.115). The basic idea behind the approach is to create a Markov chain that follows this distribution. If then an arbitrary point of the Markov chain is chosen, the draw from a Maxwell-Boltzmann distribution is simulated.

The algorithm is initialized with a single particle with random energy. By using a PDF, e.g. a Gaussian distribution, a random walk towards another energy is proposed and the energy difference is evaluated and accepted if a uniform random draw in $[0,1]$ is smaller than or equal to $e^{-\frac{\Delta E}{k_b \vartheta}}$. As a result, a random walk decreasing the energy is always accepted, but a step increasing the energy is only accepted with a certain probability, more likely at high temperatures. The series of accepted energies can be considered a Markov chain. Metropolis et al. (1953) proved that this Markov chain shows a distribution following Equation (2.115). The Markov chain can also be thought of as imaging the energy distribution by sampling their shape. The algorithm was later extended to produce draws from an arbitrary distribution by Hastings (1970).

Transferred to optimization, a particle is considered a set of parameters ϖ and its energy is the objective function $O_l(\varpi)$. A higher value of the objective function implies higher energy and lower probability and vice versa. A random walk in energy is a random walk in parameter space. In this way, this Markov chain contains parameter sets with a distribution given by the surface of the objective function if the temperature is constant. In analogy to

⁹Named after Nicholas Constantine Metropolis (1915-1999), who introduced Monte-Carlo methods (Metropolis et al. 1953).

¹⁰Named after Andrei Andreyevich Markov (1856-1922), who introduced Markov chains as representation of stochastic processes, which then were combined with Monte-Carlo methods by Metropolis and Ulam (1949).

the principle described above, this offers an interesting way of imaging the shape of the objective function, e.g. in order to investigate anomalous or multi-modal distributions.

However, the basic approach just described can also be used to find a global optimum by applying a cooling scheme to the Markov chain. This resembles the situation where a physical system is cooling down while forming crystal structures during phase transitions. If cooling down is sufficiently slow, the algorithm was proven to find the global optimum in energy (Gidas 1985; Granville et al. 1994), corresponding to a thermodynamically well-ordered crystal structure.

In context of optimization, the parameter set is initialized at a high temperature, allowing to sample the whole parameter space. If the temperature is cooled down, the set of parameters converges to the global optimum of the objective function.

2.6.3 Shape Measures of the Breakthrough Curve

Another approach to evaluate solute transport is the analysis of the shape of the BTC by analysis of the statistical moments (Koestel et al. 2011). Generally, moments are expressed as the expected value of k -th power of a random variable X according to

$$m_k = E(X^k) \quad (2.117)$$

Related to column experiments, the BTC can be considered a scaled travel-time PDF f_X or a travel-time CDF F_X in case of application of a Dirac like pulse or a continuous-feed boundary, respectively. To convert the BTC to the corresponding function, a proper scaling based on the mass balance is needed to fulfill the property of a PDF or CDF, which is

$$\int_{-\infty}^{\infty} f_X dx = \lim_{x \rightarrow \infty} F_X = 1. \quad (2.118)$$

Moments are then functionals of the BTC according to

$$m_k = \int_{-\infty}^{\infty} x^k f_X dx = \int_{-\infty}^{\infty} x^k dF_X. \quad (2.119)$$

Furthermore, central moments are defined by centering the random variable around its expected value

$$\mu_k = E((X - E(X))^k) = E((X - \mu)^k). \quad (2.120)$$

Written in integral form

$$\mu_k = \int_{-\infty}^{\infty} (x - \mu)^k f_X dx = \int_{-\infty}^{\infty} (x - \mu)^k dF_X, \quad (2.121)$$

where $\mu = m_1$ is the first moment representing the mean value of random variable X . Some of these moments offer an intuitive interpretation. The first raw moment is the mean of f_X . If f_X is considered the BTC, this equals the BCM, which is the mean travel time of the solute through the column. The second central moment represents the variance of the distribution ($\mu_2 = \sigma^2$). Each moment of a measured BTC measured in open-flow mode corresponds to specific transport processes (Koestel et al. 2011).

In this way, shape measures based on temporal moments provide a powerful tool to evaluate BTCs of open-flow experiments as these BTCs can be considered travel-time PDFs in case of a pulse-type boundary condition or travel-time CDFs in case of a continuous-feed boundary condition. The oscillating BTC of closed-flow experiments is conceptually far from a probability distribution and an evaluation of temporal moments from the entire BTC is basically meaningless as several consecutive breakthroughs overlap. In principle, if the corresponding travel-time PDF of the porous medium is identified, the analysis of temporal moments could be applied. However, this is rather pointless as all transport parameters are already given with the identification of the parameterized impulse response or travel-time PDF. For this reason, a deeper analysis of temporal moments in context of closed-flow experiments does not appear insightful and therefore was not conducted.

2.6.4 Fourier Transform

The previous sections presented an exhaustive overview of approaches for the evaluation of BTC that are also common for open-flow experiments. However, the periodic behavior inherent in the concentration oscillation in closed-flow experiments suggests further approaches that specifically deal with repeating patterns. The most prominent example, known from time-series analysis and signal processing, is the Fourier transform. It is used to convert a function from the time domain into the frequency domain or vice versa. Specifically, the Fourier transform of a periodic function that shows an oscillation over time peaks at the frequency of this oscillation. The general definition of the Fourier transform is given by

$$\mathcal{F}(f) = \int_{-\infty}^{\infty} f e^{-2\pi i t \omega} dt. \quad (2.122)$$

Owing to Euler's Formula and exploiting the symmetry of trigonometric functions, this can also be stated as

$$\mathcal{F}(f) = \int_{-\infty}^{\infty} f (\cos(2\pi t \omega) - i \sin(2\pi t \omega)) dt. \quad (2.123)$$

As measured data is not continuous, the discrete analogue (Press et al. 2007) is given by

$$\hat{f}_k = \sum_{j=0}^{N-1} f_j e^{-2\pi i \frac{j}{N} k} = \sum_{j=0}^{N-1} f_j \left(\cos(2\pi \frac{j}{N} k) - i \sin(2\pi \frac{j}{N} k) \right). \quad (2.124)$$

The real part of \hat{f} carries information on the even symmetrical part of f and the imaginary part of \hat{f} carries information on the odd symmetrical part of f . Since the phase of the oscillation is not of interest and therefore the distinction between odd and even symmetry can be omitted, the absolute value of the complex \hat{f} according to

$$|\hat{f}_k| = \sqrt{\Re(\hat{f}_k)^2 + \Im(\hat{f}_k)^2} \quad (2.125)$$

is the most meaningful result from the Fourier transform regarding the evaluation of oscillations in closed-flow experiments.

Due to a large amount of redundant calculations in Equation (2.124), the discrete Fourier transform is often solved with algorithms known as Fast-Fourier transform that are computationally more efficient (Duhamel and Vetterli 1990). As measured data is often not equidistant, adapted algorithms might be necessary (Dutt and Rokhlin 1993).

2.6.5 Hypotheses Emerging from the BTC analysis

The altered shape of the BTC in closed-flow experiments demands an investigation on the applicability of the presented methods. The most suggestive hypotheses are

1. The convolution of the travel-time PDF and input signal is still a valid representation of the processes in a closed-flow experiment.
2. The Fourier transform of the BTC provides additional insights into the periodic behavior of closed-flow experiments.

These hypotheses are answered in subsection 5.1.4.

3 Material and Methods

3.1 Experimental Procedures

3.1.1 Columns and Substrate

For the demonstration of features of closed-flow experiments, column experiments with reactive and non-reactive substrates were conducted, each in duplicate (emc GmbH, Germany, material: polymethylmethacrylat (PMMA)). The non-reactive substrate was prepared of quartz sand (Type Haltern H33, Quarzwerke GmbH, Germany) that was dry-mixed with quartz silt (Type Millisil Haltern W11, Quarzwerke GmbH, Germany) until a visually homogeneous distribution was achieved. Hence, this mixture produces a silty sand with low chemical reactivity. When appropriate, synthetic goethite (LANXESS Bayferrox 920) was added and served as reactive substrate. Furthermore, for some reference tests, pure quartz sand (Roth, Quarz, 0.4 mm to 0.8 mm) was used. The material was characterized with respect to mineral composition with X-Ray diffraction (XRD) (D8 ADVANCE, Bruker, Germany), morphology with scanning electron microscopy (SEM) (ULTRA PLUS field emission scanning electron microscope, Zeiss, Germany) and specific surface area measured with the N₂-Brunauer-Emmett-Teller (BET) method (Brunauer et al. 1938) (Quantachrome, Syosset, USA).

Quartz Sand Haltern H33

The quartz sand used for most of the substrates was Type H33 from the mining region Haltern. Details on the size distribution are given in Table 3.2. The grains were rounded (Figure 3.1) giving a specific surface area of 0.125 m² g⁻¹. Quartz usually exhibits a low

Table 3.1: Composition of substrates used for the column experiments

	Qz	ASQz	ASQzGt
Quartz sand Roth [wt%]	100	0	0
Quartz sand Haltern H33 [wt%]	0	73	95
Quartz silt Millisil Haltern W11 [wt%]	0	27	0
Goethite Bayferrox 920 [wt%]	0	0	5

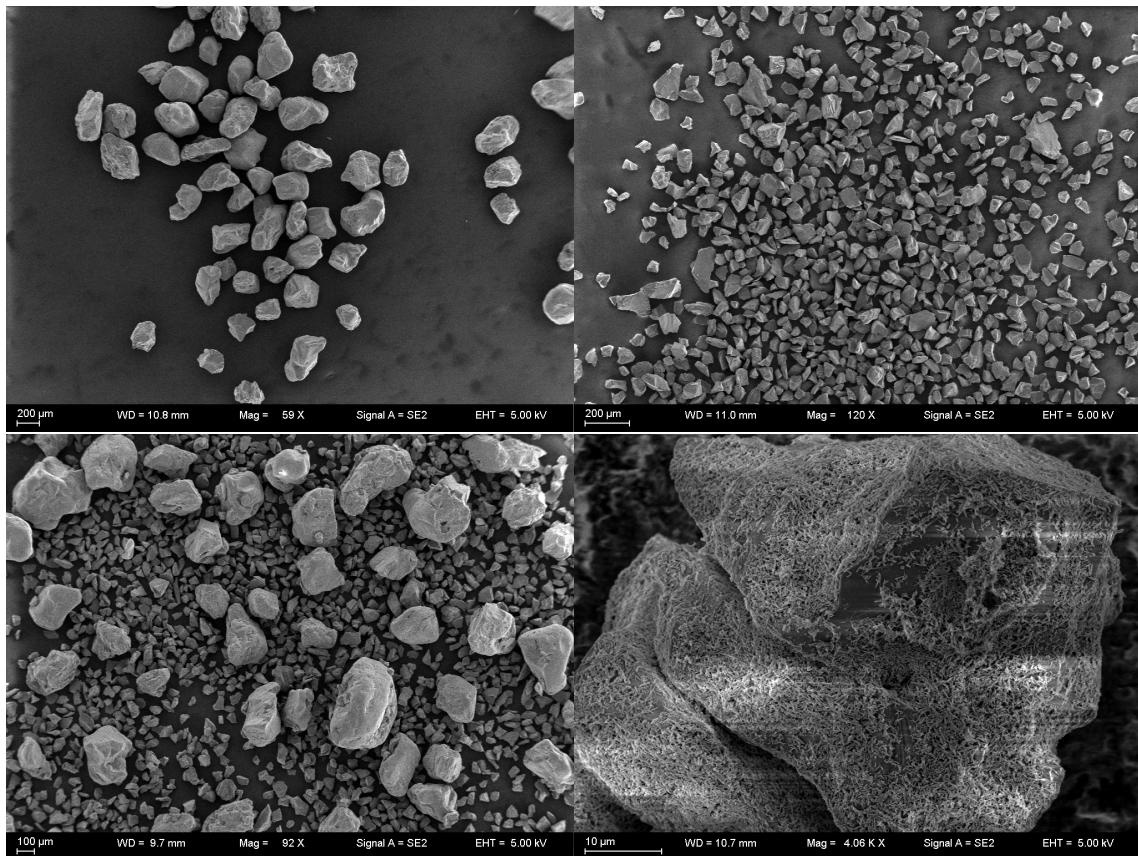


Figure 3.1: SEM images of artificial soil materials: pure quartz sand Haltern H33 (top left), quartz silt W11 after wet sieving (top right), mixture of H33 and W11 as used in the experiments (bottom left), quartz surface coated with goethite as a result from goethite addition (bottom right)

PZC around 3 and therefore the quartz surface is negatively charged in contact with near pH-neutral solutions.

Quartz Silt Millisil W11

The quartz silt was delivered by the same supplier as the quartz sand. After preliminary experiments suffered from severe particle mobilization when using the raw grain size distribution, the fine particle fraction below $36\ \mu\text{m}$ was removed by wet sieving. This process resulted in a mean grain size of $40\ \mu\text{m}$ (Table 3.3). The surface was determined as $1\ \text{m}^2\ \text{g}^{-1}$ showing sharp edges from milling (Figure 3.1).

Table 3.2: Grain size distribution of quartz sand Haltern H33 (manufacturer's specifications)

grain size [μm]	355-500	250-355	180-250	125-180	90-125
fraction [wt%]	8	48	33	10	1

Goethite Bayferrox 920

The mineral used for the composition of the reactive substrate was goethite, since it is ubiquitous in soils of moderate climates and, as major constituent of soil, causes a large part of their reactivity (Liu et al. 2014). Goethite minerals form characteristic needle-like well-ordered crystals. It is also often used as a representative iron oxide, since there are several synthesis pathways that can produce pure goethite without expensive instrumentation (Cornell and Schwertmann 2003). Characterization via XRD and SEM revealed pure goethite with a mean needle length of 600 nm. The specific surface area was measured as $16.6 \text{ m}^2 \text{ g}^{-1}$ with N_2 -BET. Goethite is characterized by a PZC of around 8 leading to a positively charged surface in neutral and acidic solutions. When mixed with quartz, the contrast in charge in neutral solutions produces strong associations of quartz and goethite minerals. As a result, the proposed reactive mineral mixture ASQzGt has shown to be stable with respect to water flow despite the small goethite crystal size, ascertained by occasional measurements of Fe in the column effluent.

Experimental Setup

The material was dried at 105°C for three days before packing and filled into the columns with stepwise manual compaction to produce a homogeneous pore size distribution. This resulted in bulk densities of around 1.65 g cm^{-3} . Porous plates of stainless steel with a pore size of $5 \mu\text{m}$ were placed at the inlet and outlet of the columns. The mixing vessels (SIMAX laboratory bottle 100 mL, Friedrich and Dimmock, Inc., USA) were connected to the column outlets via connection tubes (ISMATEC Tygon standard tubing, IDEX Health and Science, Germany) and to the column inlets via pumping tubes (ISMATEC PharMed PBT, IDEX Health and Science, Germany) driven by a peristaltic pump (ISMATEC Reglo Analog, IDEX Health and Science, Germany). To avoid a large impact of void volumes, the tubing was shortened to a minimum. The gravimetrically determined volumes of the setup void volume and tubing were in the range of a few mL. The mixing vessels were covered with laboratory film (PARAFILM, Pechiney Plastic Packaging, USA) to avoid evaporation. The columns were saturated with ultrapure water (Elix+Milli Q, Millipore, USA; $R=18.2 \text{ M}\Omega$, $\text{DOC} < 1 \text{ ppm}$) and washed in open-flow mode until the electrical conductivity of the effluent was below $15 \mu\text{S cm}^{-1}$. The water content required for saturation was determined gravimetrically. The mixing vessels were equipped with

Table 3.3: Grain size distribution of quartz silt Millisil W11 after wet sieving

grain size [μm]	125-160	100-125	63-100	40-63	36-40
fraction [wt%]	0.2	1.8	10.5	63	24.5

electrical conductivity probes (LTG 1/23 SMEK, Meinsberg, Germany) connected to a data logger (KM2000, Meinsberg, Germany). To ensure a homogeneous mixture, the mixing vessels were placed on a magnetic stirring device (MULTISTIRRER 6, Fischer Scientific, Germany) and equipped with magnetic stir bars.

Prior to each experiment, the exact pumping rate was determined gravimetrically. In particular for long term experiments, the actual rate might deviate from the requested one due to wear of the tubing. The exact parameters of each experimental setup are given in the corresponding section discussing the results of that particular experiment.

3.1.2 Conservative Tracer Experiments

All tracer tests were conducted with 10 mM NaCl (Roth, Germany; p.a.) solution (pH=6.1) or ultrapure water. The contrast in ionic strength was intended to permit the interpretation of electrical conductivity as surrogate for tracer concentration. Since the goethite/quartz mixture was stable at both ionic strengths, no impact on the porous medium was assumed. Measurements of the electrical conductivity were used to reconstruct the NaCl concentration, exploiting the near linear correlation in the applied concentration range (Lide 2009).

The breakthrough experiments were carried out at different flow rates and different mixing vessel volumes filled with tracer solution, which each correspond to a distinct volumetric dilution factor. Thus, a relative decrease in concentration to the value given by this factor is expected due to dilution. When the tracer solution was provided with the mixing vessel, the flow started and electrical conductivity was logged in equidistant time steps. Experiments carried out in this way are referred to as “forward breakthrough”. After the electrical conductivity reached a constant value indicative of an equilibrium between the solid and the mobile phase, the solution in the mixing vessel was replaced with ultrapure water. Then, the flow continued until reestablishment of constant electrical conductivity. This phase is referred to as “backward breakthrough”, since the starting conditions are inverted. After the sequence of forward and backward breakthrough, the columns were rinsed with ultrapure water in open-flow mode at the same flow rate for preparing the same initial conditions as for the previous experiments. Rinsing was stopped after the effluent reached an electrical conductivity smaller than $15 \mu\text{S cm}^{-1}$ for at least one day to prevent the interference of possible physical non-equilibrium. Since NaCl is easily soluble and Cl^- is nonreactive with respect to quartz at near-neutral pH due to the low PZC of quartz (Kosmulski 2011) and the affinity of Na^+ to quartz surfaces is negligible for the mass balance (Allen et al. 1971), it was assumed that subsequent experiments were not influenced by previous NaCl percolations. For media containing goethite, it was assumed that adsorption of Cl^- is negligible at near-neutral pH (Hingston et al. 1972) and Cl^- is easily displaced by other anions competing for adsorption sites (Cornell and Schwertmann 2003).

At this stage, the next breakthrough experiment was started. For the investigation of physical non-equilibrium or other effects strongly related to the fluid flow velocity, the recommendations from Wehrer and Totsche (2003, 2008) to run experiments exhibiting a ratio of a least five in flow velocity were followed.

3.1.3 Reactive Tracer Experiments

Vanillic Acid (Alfa Aesar, Germany, >98%) was used as reactive tracer at a concentration of 0.1 mM and chosen as surrogate representing a typical compound in the degradation pathway of lignin (Ruiz-Dueñas and Martinez 2009). Therefore, it is commonly found in soils (e.g. Ander et al. 1984). An intermediate reactivity towards goethite is expected due to the carboxylic moiety with a pK_a of 4.53. The quantification of vanillic acid exploits the strong UV absorption of aromatic compounds and the linear relationship of UV/Vis absorption and solute concentration according to Lambert-Beer's law. UV/Vis spectra were obtained in a flow-through quartz cuvette (Suprasil 3.5 mL, Hellma, Germany) using a Cary 50 UV/Vis spectrophotometer (Varian, Germany). Spectra were resolved in 1nm steps at a scan rate of 120 nm min^{-1} from 350 nm to 200 nm. Quantification of vanillic acid was carried out using positive matrix factorization (Paatero and Tapper 1994; Kim and Park 2008) of the entire set of spectra including a spectrum of the stock solution. Sample scores were normalized to the score of the stock solution.

3.2 Numerical Aspects

Because of the strict requirements that have to be fulfilled in order to apply analytical solutions, the most widely used approach, which can handle all variation in additional terms of the ADE at any boundary condition and high-dimensional space, is the numerical solution. The basic idea behind numerical solutions is to discretize the derivatives in the ADE in order to simplify this PDE defined on a continuum to a discrete and therefore computable approximation. A number of discretization methods is available for temporal derivatives, e.g. Euler schemes (e.g. Butcher 2008) and the Crank-Nicholson scheme (Crank and Nicolson 1996), and spatial derivatives, e.g. the finite-differences scheme, the finite-elements scheme or the finite-volumes scheme (e.g. Allaire and Craig 2007). Depending on the properties of the PDE and the type of problem, each scheme performs differently well. To highlight a few strengths of spatial schemes, a finite-volume scheme offers inherent mass conservation, a finite-element scheme is very flexible in representing structured domains and a finite-difference scheme is easy to implement (Tadmor 2012). An examination of temporal schemes reveals a similar situation. Explicit schemes are very accurate at high gradients when using slope limiters (Sweby 1984) and allow a straightforward implementation, but often suffer from numerical instability, whereas the stable implicit schemes require the solution of huge systems of equations and are prone to produce artifacts, especially numerical dispersion.

The modeling of closed-flow experiments obviously also relies on the solution of the ADE, since the transport processes inside the column are not changed due to the solute recirculation. However, the inflow solution serves as inflow boundary condition to the transport problem in the form of Dirichlet or Neumann boundary conditions. Implemented as constant in open-flow experiments, the temporal change of the mixing vessel solution that feeds the inflow has to be considered here. The dynamic behavior is covered by the PDE describing the development of concentration in the mixing vessel as shown in Equation (2.66) in dependence of concentration carried with the effluent. The latter corresponds to the outflow boundary solution of the transport problem in the column, which results from the inflow boundary. Here, the circle of dependencies and the closed-loop of the setup becomes evident as mathematical circular reference. To sum up, the simulation of closed-flow experiments requires a coupling of the ADE to the constitutive equation describing the mixing vessel. The following sections explain the methods and consequences of discretization Equation (2.66) in an explicit and implicit way.

3.2.1 Explicit Solution

An explicit solution of a PDE is constructed with all variables outside the temporal gradient representing the system state at the current time step i . In general, these system states are

known quantities and the resulting equations can be solved without further considerations. An explicitly discrete formulation of Equation (2.66) would be stated by substituting the left-hand side containing the derivative with a difference quotient and the right-hand side with the known current concentrations as follows

$$\frac{c_{\text{mix}}^{i+1} - c_{\text{mix}}^i}{\Delta t} = \frac{Q}{V_{\text{mix}}} (c_e^i - c_{\text{mix}}^i). \quad (3.1)$$

A rearrangement with respect to the only unknown c_{mix}^{i+1} results in

$$c_{\text{mix}}^{i+1} = \frac{1}{V_{\text{mix}}} (c_e^i Q \Delta t + c_{\text{mix}}^i (V_{\text{mix}} - Q \Delta t)) \quad (3.2)$$

With this equation, the development of concentration of solute in the mixing vessel can be calculated directly from ADE modeling results and the numerical implementation is straight forward.

3.2.2 Implicit Solution

An implicit solution of a PDE is constructed with all variables outside the temporal gradient representing the system state at the time step succeeding i . These quantities are usually unknown and only result from a consideration of other statements also containing the unknowns. The solution is therefore implicit in a set of statements which then result in a large system of equations. In this way, the new system state at $i + 1$ is calculated for all unknown quantities combined, whereas explicit solutions calculate each quantity isolated. This approach dramatically increases the numerical stability due to the distribution of, e.g., approximation errors and discretization errors among the unknowns. As a result, local overestimates or underestimates of concentrations are damped out. However, this comes at the cost of the smearing of gradients, often referred to as “numerical diffusion”. An implicitly discrete formulation of Equation (2.66) would be stated by substituting the left-hand side containing the derivative with a difference quotient and the right-hand side with the concentrations from the time step succeeding i as follows

$$\frac{c_{\text{mix}}^{i+1} - c_{\text{mix}}^i}{\Delta t} = \frac{Q}{V_{\text{mix}}} (c_e^{i+1} - c_{\text{mix}}^{i+1}). \quad (3.3)$$

A rearrangement with respect to c_{mix}^{i+1} and defining $V_{\text{mix}}^{\text{inc}}$ as the mixing vessel solute volume increased by the volume due the volumetric flux during the time step according to $V_{\text{mix}}^{\text{inc}} = V_{\text{mix}} + Q\Delta t$ yields

$$\begin{aligned} c_{\text{mix}}^{i+1} &= \frac{1}{Q\Delta t + V_{\text{mix}}} (c_e^{i+1}Q\Delta t + c_{\text{mix}}^i V_{\text{mix}}) \\ &= \frac{1}{V_{\text{mix}}^{\text{inc}}} (c_e^{i+1}Q\Delta t + c_{\text{mix}}^i V_{\text{mix}}). \end{aligned} \quad (3.4)$$

3.2.3 Numerical Implementation

Under assumption of an equidistant grid, the spatial domain can be divided into $J + 1$ nodes. A concentration is defined at each node ranging from c_0 to c_J . The distance between each node is then Δx . The current time step is denoted as Δt and upper indices appearing in concentration statements represent the time.

The implementation of the explicit solution can be realized by substituting the term representing the influent concentration at the inflow boundary with Equation (3.2). This approach requires no further adaptation of the numerical scheme regarding the transport in the column and can be applied to both, implicit and explicit solutions of the ADE. For consistency, the implementation of the explicit solution was coupled to an explicit Euler scheme with an upwinding scheme and a slope limiter for the stabilization of advection dominated systems (Noye 1987b).

In contrast, the implementation of the implicit solution has implications for the numerical scheme used for the simulation of transport in the column. In the following derivation, this is illustrated by a simplified depiction of the numerical scheme (Hogarth et al. 1990; Noye 1987a). As a basis, an implicit one-dimensional finite difference discretization of the most basic formulation of the ADE is given as

$$\partial_t c = D\partial_x^2 c - v\partial_x c \quad (3.5)$$

$$\frac{c_j^{i+1} - c_j^i}{\Delta t} = D \frac{c_{j-1}^{i+1} - 2c_j^{i+1} + c_{j+1}^{i+1}}{\Delta x^2} - v \frac{-c_{j-1}^{i+1} + c_{j+1}^{i+1}}{2\Delta x}. \quad (3.6)$$

The derivatives were approximated as central differences. A rearrangement with respect to concentration results in

$$c_j^i = c_{j-1}^{i+1} \underbrace{\left(-\frac{D\Delta t}{\Delta x^2} - \frac{v\Delta t}{2\Delta x} \right)}_{B_-} + c_j^{i+1} \underbrace{\left(\frac{2D\Delta t}{\Delta x^2} + 1 \right)}_B + c_{j+1}^{i+1} \underbrace{\left(-\frac{D\Delta t}{\Delta x^2} + \frac{v\Delta t}{2\Delta x} \right)}_{B_+}. \quad (3.7)$$

In this equation, the three unknown quantities are c_{j-1}^{i+1} , c_j^{i+1} and c_{j+1}^{i+1} . The coefficients with constant, known terms are combined as B with respective indices. Assuming a mixed boundary condition at the inflow, i.e. a Neumann boundary condition for the isolation of

diffusion by forcing $\partial_x c|_{x=0} = 0$ and a Dirichlet boundary condition for advection, and a zero gradient boundary condition at the outflow, two boundary equations can be set up according to

$$\frac{c_0^{i+1} - c_0^i}{\Delta t} = D \frac{-c_0^{i+1} + c_1^{i+1}}{\Delta x^2} - v \frac{-c_{\text{mix}}^{i+1} + c_1^{i+1}}{2\Delta x} \quad (3.8)$$

$$c_{\text{mix}}^{i+1} \frac{v\Delta t}{2\Delta x} + c_0^i = c_0^{i+1} \underbrace{\left(\frac{D\Delta t}{\Delta x^2} + 1 \right)}_A + c_1^{i+1} \underbrace{\left(-\frac{D\Delta t}{\Delta x^2} + \frac{v\Delta t}{2\Delta x} \right)}_{A_+} \quad (3.9)$$

and

$$\frac{c_J^{i+1} - c_J^i}{\Delta t} = D \frac{-c_{J-1}^{i+1} + c_J^{i+1}}{\Delta x^2} - v \frac{-c_{J-1}^{i+1} + c_J^{i+1}}{2\Delta x} \quad (3.10)$$

$$c_J^i = c_{J-1}^{i+1} \underbrace{\left(-\frac{D\Delta t}{\Delta x^2} - \frac{v\Delta t}{2\Delta x} \right)}_{C_-} + c_J^{i+1} \underbrace{\left(1 + \frac{D\Delta t}{\Delta x^2} + \frac{v\Delta t}{2\Delta x} \right)}_C. \quad (3.11)$$

If Equation (3.7) is formulated for every j , also concerning the boundaries written in Equation (3.9) and Equation (3.11), a system of equations develops, which can be represented in matrix form as

$$\begin{pmatrix} A & A_+ & 0 & \dots & \dots & \dots & 0 \\ B_- & B & B_+ & 0 & \ddots & \ddots & \vdots \\ 0 & B_- & B & B_+ & 0 & \ddots & \vdots \\ \vdots & \ddots & \ddots & \ddots & \ddots & \ddots & \vdots \\ \vdots & \ddots & 0 & B_- & B & B_+ & 0 \\ \vdots & \ddots & \ddots & 0 & B_- & B & B_+ \\ 0 & \dots & \dots & \dots & 0 & C_- & C \end{pmatrix} \begin{pmatrix} c_0^{i+1} \\ c_1^{i+1} \\ \vdots \\ c_j^{i+1} \\ \vdots \\ c_{J-1}^{i+1} \\ c_J^{i+1} \end{pmatrix} = \begin{pmatrix} c_0^i + c_{\text{mix}}^{i+1} \frac{v\Delta t}{2\Delta x} \\ c_1^i \\ \vdots \\ c_j^i \\ \vdots \\ c_{J-1}^i \\ c_J^i \end{pmatrix}. \quad (3.12)$$

Numerical methods to invert the matrix on the left, e.g. Gaussian elimination or iterative solution schemes that exploit the sparsity of matrices found in the numerical solution of PDEs (Saad 2000), are then applied to solve for c_0^{i+1} to c_J^{i+1} . This illustrates the basic numerical scheme of an one-dimensional implicit finite-difference solution of the ADE in open-flow experiments. The quantity c_{mix}^{i+1} is placed on the right side of the equation, since its value is known for well-defined boundary conditions in open-flow experiments independent of the numerical solution.

However, in closed-flow experiments, the dynamic behavior of the mixing vessel, which is dependent on the outflow and therefore on the numerical solution of the particular time step, demands a reformulation of the boundary equation at the inflow. Following the

previous example, the expression of c_{mix}^{i+1} in Equation (3.9) has to be substituted with the statement in Equation (3.3) under the assumption that the effluent concentration c_e^{i+1} equals the concentration at the last node c_J^{i+1} resulting in

$$\frac{c_0^{i+1} - c_0^i}{\Delta t} = D \frac{-c_0^{i+1} + c_1^{i+1}}{\Delta x^2} - v \frac{-\frac{1}{V_{\text{mix}}^{\text{inc}}}(c_J^{i+1}Q\Delta t + c_{\text{mix}}^i V_{\text{mix}}) + c_1^{i+1}}{2\Delta x} \quad (3.13)$$

$$c_{\text{mix}}^i \frac{v\Delta t V_{\text{mix}}}{2\Delta x V_{\text{mix}}^{\text{inc}}} + c_0^i = c_J^{i+1} \underbrace{\left(-\frac{vQ\Delta t^2}{2\Delta x V_{\text{mix}}^{\text{inc}}}\right)}_{A_-} + c_0^{i+1} \underbrace{\left(\frac{D\Delta t}{\Delta x^2} + 1\right)}_A + c_1^{i+1} \underbrace{\left(-\frac{D\Delta t}{\Delta x^2} + \frac{v\Delta t}{2\Delta x}\right)}_{A_+}. \quad (3.14)$$

Here, an additional term in the equation describing the inflow can be seen in form of a dependence from the effluent concentration, while the rest of the numerical scheme remains the same. The difference becomes evident constructing the system of equations again as matrix form according to

$$\begin{pmatrix} A & A_+ & 0 & \dots & \dots & 0 & A_- \\ B_- & B & B_+ & 0 & \ddots & \ddots & 0 \\ 0 & B_- & B & B_+ & 0 & \ddots & \vdots \\ \vdots & \ddots & \ddots & \ddots & \ddots & \ddots & \vdots \\ \vdots & \ddots & 0 & B_- & B & B_+ & 0 \\ \vdots & \ddots & \ddots & 0 & B_- & B & B_+ \\ 0 & \dots & \dots & \dots & 0 & C_- & C \end{pmatrix} \begin{pmatrix} c_0^{i+1} \\ c_1^{i+1} \\ \vdots \\ c_j^{i+1} \\ \vdots \\ c_{J-1}^{i+1} \\ c_J^{i+1} \end{pmatrix} = \begin{pmatrix} c_0^i + c_{\text{mix}}^i \frac{v\Delta t V_{\text{mix}}}{2\Delta x V_{\text{mix}}^{\text{inc}}} \\ c_1^i \\ \vdots \\ c_j^i \\ \vdots \\ c_{J-1}^i \\ c_J^i \end{pmatrix}. \quad (3.15)$$

Hence, the loop in the setup appears as entry A_- in the matrix, giving it a more circular pattern. This is especially important since many approaches to solve matrices requires strong conditions on the matrix structure or are based on the reduction of the matrix inversion to the diagonals. Therefore, the matrix was inverted via Gaussian elimination guided according to the sparsity of the matrix.

The implementation of source and sink functions, e.g. liquid solid interaction and microbial degradation, was achieved by an appropriate extension of Equation (3.5) to comply with all the processes represented by the two-site two-region model according to Equation (2.25) to Equation (2.30). Newton's method was used to solve equations involving nonlinear interactions.

3.3 Software Development

3.3.1 Design Paradigms and Features

In order to perform sensitivity analyses and inverse modeling, a software was developed in PureBasic featuring a graphical user interface (GUI) for convenient application and real-time visualization. Special focus was given to the ease of application and an intuitive interface allowing quick data management. The intention was to leave the end-user playing around with possible options and thinking about the transport properties rather than the syntax of complicated shell input commands without sacrificing the functionality. A list of features is given in the following overview

Transport processes (see section 2.1):

1. advection
2. dispersion
3. (rate limited) adsorption following linear, Langmuir or Freundlich isotherms
4. diffusion into immobile regions
5. first-order decay and zero-order production

Experimental boundary conditions:

1. open-flow mode and closed-flow mode
2. application of a fraction collector
3. void volumes before and after the column
4. flow interrupts

Numerical Schemes (see subsection 3.2.3):

1. fully implicit Euler scheme with central differences as fast and stable generic solution
2. explicit upwinding scheme with slope limiter for stabilization of advection dominated systems

Optimization schemes:

1. one-dimensional line search
2. multi-parameter local optimization using the Levenberg-Marquardt algorithm (see section 2.6.2)
3. simulated annealing as generic global optimization (see section 2.6.2)

Sensitivity analyses:

1. automated calculation of a family of BTCs with a transport parameter scanning an interval
2. generating the objective function in dependence of two transport parameters in order to visualize multiple optima, correlations and equifinality

Shape analyses:

1. quick calculation of first and second derivatives of BTCs
2. discrete Fourier transform of BTCs
3. calculation of shape measures (see subsection 2.6.3)

GUI:

1. structured overview and access to parameters
2. import and export of data via the application programming interface (API) of the operating system using convenient file requester windows
3. real-time visualization of BTCs and spatial distribution of concentrations along the transport profile
4. allow customization to acknowledge personal preferences

Additional features:

1. convolution of data with analytical expressions of the transfer function (see subsection 2.6.1)
2. disturbance of calculated BTCs with heteroscedastic white noise generated with the Box-Muller method (Box and Muller 1958)

3.3.2 Model verification

To verify the model, a set of open-flow BTCs from the analytical solution of the ADE as presented in Equation (2.101) was calculated with Pe numbers ranging from 0.01 to 100 in order to simulate advection dominated as well as diffusion dominated systems. For the inflow, pulse-type and continuous-feed boundary conditions were used. The numerical implementation was then compared to these calculations. For each BTC, an R^2 of >0.9999 was achieved and the error in solute mass balance for the numerical simulation was $<0.1\%$. This proves the numerically correct implementation and discretization of the ADE in the presented software for the application with open-flow experiments. However, the verification

with respect to the modeling of closed-flow experiments is given in the results, since no analytical solution is known to the author and the modeling hypotheses with regard to the mixing vessel itself have to be verified in addition to the numerical implementation.

3.3.3 Illustration of Sensitivity Analyses

Throughout this thesis, a large number of sensitivity analyses are presented. As this term may be used in slightly different ways, a clear distinction is provided to help the reader in interpretation.

1. A series of modeled BTCs scanning a certain parameter:

This type of sensitivity analysis is presented in order to show the effect of varying transport parameters on the shape of the BTC. There, the BTC is modeled several times while scanning an interval of the parameter in focus. The response of the BTC gives an intuition about how sensitive the BTC is with respect to the parameter.

This kind of sensitivity analyses is usually presented as classical two-dimensional graph showing a family of BTCs.

2. Surface of the objective function around the two-dimensional parameter optimum:

The performance of optimization schemes and the parameter uncertainty depends on the surface of the objective function around the parameter optimum. An illustration of this surface gives a good intuition on parameter correlation and sensitivity.

Here, two independent variables are modeled to give a three-dimensional graph, which is then presented as “heat map”. Each “heat map” is obtained from 100x100 model runs, each represented by one particular dot of the “heat map”. In contrast to the next type, all calculations refer to one BTC and thus, one set of optimal parameters. This type of “heat map” can be recognized from the white asterisk at the center that indicates the global optimum.

3. Response of the one-dimensional objective function to changes in the volumetric dilution factor d_v :

To assess the performance of the closed-flow design in inversely modeling parameters, it is most convenient to illustrate the shape of the objective function with respect to changes of one particular parameter at different d_v values. Specifically, BTCs were modeled at a wide interval of d_v values using a fixed set of parameters. For each BTC, the shape of the objective function around the optimum of one particular parameter is calculated.

In this way, also two independent variables are created and the results are presented as “heat map”. In contrast to the previous description, each row in this kind of “heat map” refers to a different modeled BTC at another d_v . This type of “heat map” can be recognized from the logarithmic y-axis with different d_v .

4 Results and Discussion

Part of the experimental results at different mixing vessel solute volumes are published in Ritschel and Totsche (2016b) and part of the sensitivity analysis with respect to dispersion and rate-limited interaction is in revision for publication (Ritschel and Totsche 2016a).

4.1 Experiment A: Different Mixing Vessel Volumes

As already noted in Totsche (2001) and Ritschel (2011), the volume of the mixing vessel is the most decisive boundary condition in closed-flow experiments, but its predicted effect on the shape of the BTC, i.e. a pronounced appearance of oscillations at smaller mixing vessels, is experimentally unverified until now. To investigate this issue, two columns (inner diameter: 4.1 cm, length: 15 cm) were set up in closed-flow mode using the ASQz medium and a mixing vessel with a solute volume of 100 mL. The bulk densities were 1.66 g cm^{-3} and 1.67 g cm^{-3} for column I and column II, respectively. The gravimetrically determined water volumes including water in tubing and void volume of the setup were $(67.2 \pm 0.3) \text{ mL}$ and $(64.6 \pm 0.3) \text{ mL}$ for column I and column II, respectively. Afterward, another two columns (inner diameter: 4.1 cm, length: 10 cm) were set up for experiments with a mixing vessel volume of 30 mL and 20 mL. Bulk densities were 1.65 g cm^{-3} and 1.66 g cm^{-3} for column I and column II, respectively. The gravimetrically determined water volumes including water in tubing and void volume of the setup were $(44.5 \pm 0.2) \text{ mL}$ and $(43.3 \pm 0.2) \text{ mL}$ for column I and column II, respectively. The void volume in the column setup was estimated as 4.1 mL and 3.0 mL for column I and column II, respectively. The column setups were assumed to fulfill the assumptions needed for the application of the ADE, since the structural correlation is small compared to the column length and the columns were packed from homogenized material (Khan and Jury 1990). The mixing vessels were filled with NaCl tracer and equipped with a probe for measuring the electrical conductivity. For $V_{\text{mix}} = 30 \text{ mL}$ and $V_{\text{mix}} = 20 \text{ mL}$, the backward breakthrough was also recorded applying ultrapure water to the mixing vessels. The exact pumping rates in each experiment are given in Table 4.1.

4.1.1 Effect on the Breakthrough Behavior

The resulting BTCs are shown in Figure 4.1. With decreasing mixing vessel volume (=lowering of the d_v) four main characteristics of the BTC are affected:

1. the final equilibrium concentration
2. steepness of the initial exponential decrease
3. amplitude of oscillation
4. wavelength of the oscillation.

The change in equilibrium is the trivial consequence of solute mixing between the involved volumes. Large mixing vessel volumes show a relatively small decrease in concentration due to minor impact of the water-filled pore space, whereas small mixing volumes are diluted to a larger extent. The exponential decrease in the beginning of a BTC is a result from the dilution with tracer free solution from the column effluent. The exponential shape directly follows from Equation (2.70) as long as the effluent concentration is zero. With decreasing mixing vessel volume also the steepness of the exponential decrease becomes higher resulting from the faster dilution in smaller mixing vessel volumes at constant volumetric flux rates. For the same reason, an increase in effluent concentration, which is to be expected near 1 pv, imprints much faster on the shape of the BTC at smaller mixing vessel volumes. As a result, the rise in concentration of the BTC following the exponential decrease is more pronounced and the overall amplitude of the oscillation is higher. This is reflected in the amount of visible concentration maxima in the BTC. At a mixing vessel of 100 mL hardly any oscillation can be seen, whereas at $V_{\text{mix}} = 30$ mL two maxima and at $V_{\text{mix}} = 20$ mL three maxima are clearly visible. At last, the wavelength of the oscillation becomes shorter with decreasing mixing vessel volume due to the faster passage of a solute pulse through the mixing vessel volume (Figure 4.1 a).

The backward BTC are inverse with respect to the characteristics of the oscillations caused by the inverse initial conditions, i.e. a porous medium uniformly filled with tracer

Table 4.1: Experimental boundary conditions for the experiment with different mixing vessel volumes and water volumes reconstructed from BTC data.

Experiment Column	$V_{\text{mix}} = 100$ mL		$V_{\text{mix}} = 30$ mL		$V_{\text{mix}} = 20$ mL	
	I	II	I	II	I	II
Q [$\mu\text{L min}^{-1}$]	66.4 ± 1.1	66.1 ± 1.1	66.5 ± 1.1	69.3 ± 1.1	33.2 ± 1.1	33.3 ± 1.1
V_p [mL]	67.2 ± 0.4	64.6 ± 0.3	44.5 ± 0.2	43.3 ± 0.2	-	-
recon. V_p [mL]	61.5 ± 1.0	58.5 ± 0.9	43.2 ± 0.6	43.3 ± 0.6	53.6 ± 1.0	49.2 ± 0.9
θ [-]	0.310	0.295	0.337	0.328	-	-

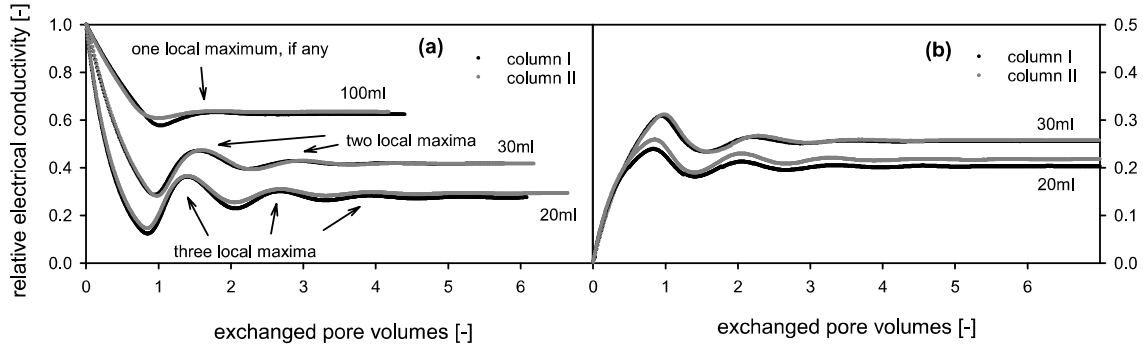


Figure 4.1: BTCs measured in the mixing vessel of a closed-flow setup with $V_{\text{mix}} = 100 \text{ mL}$, $V_{\text{mix}} = 30 \text{ mL}$ and $V_{\text{mix}} = 20 \text{ mL}$ resulting in $d_v = 0.62$, $d_v = 0.41$ and $d_v = 0.27$ (a) and backward BTCs measured in the mixing vessel of a closed-flow setup with $V_{\text{mix}} = 30 \text{ mL}$ and $V_{\text{mix}} = 20 \text{ mL}$ (b).

solution and a mixing vessel solution void of tracer. Thus, the concentration in the mixing vessel is rising in the beginning reaching a maximum around 1 pv and oscillating afterwards. Comparable to the forward breakthrough, a smaller mixing vessel produces more pronounced and longer oscillations (Figure 4.1 b).

4.1.2 Determination of the Water-Filled Pore Space

As expected from theoretical considerations, the system relaxes to a stable concentration in the aqueous phase after the oscillations have diminished. Considering the mass balance in closed-flow experiments, this equilibrium is indicative for the water content since the application of a conservative tracer also implies the validity of the assumptions made in subsection 2.3.3 that the only process causing a long-term decrease in concentration is the mixture of different volumes. Due to the lack of exact knowledge on the setup void volumes, Equation (2.53) was used to calculate the apparent water content for a comparison with independently determined gravimetrical values (Table 4.1).

For the first set of columns with $V_{\text{mix}} = 100 \text{ mL}$, the calculated V_p using the observed dilution were $(61.5 \pm 1.0) \text{ mL}$ and $(58.5 \pm 0.9) \text{ mL}$ for column I and column II, respectively. Considering the gravimetrical determination, this is about 6 mL lower than expected, pointing towards stagnant regions in the column setup that do not take part in the actual water flow and therefore do not dilute the tracer. For this reason, the column setup was changed for further experiments to reduce the void space in tubing and experimental setup to the largest possible extent. In the following setup, the calculated V_p using the dilution measured in the experiments were $(43.2 \pm 0.6) \text{ mL}$ and $(43.3 \pm 0.6) \text{ mL}$, which was now very close to the gravimetrical values. This highlights the importance of distinguishing void space that is involved in transport and void space that is separated from the water flow. Experiments carried out later with the same columns and $V_{\text{mix}} = 20 \text{ mL}$

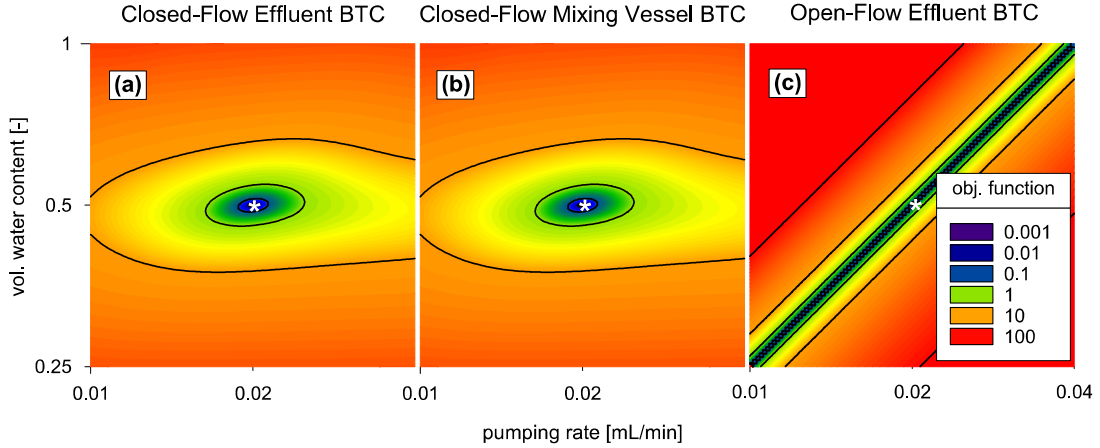


Figure 4.2: Surface of the objective function with respect to changes in the water content and the pumping rate around the optimal value of $\theta = 0.5$ and $Q = 0.02 \text{ mL min}^{-1}$ at $d_v = 0.5$ in case of closed-flow experiments (a, b) and open-flow experiments (c).

show higher water contents, indicating a fluctuating saturation over time (Table 4.1), which is coherent with the observation of small encapsulated air bubbles inside the columns in the beginning of the experiment. Air entrapment is commonly observed and is to be expected when using quartz sand media similar to ASQz (Holocher et al. 2002). This shows that complete water saturation was not reached within the first exchanged pore volumes in porous media solely composed of quartz grains and that the water content has to be verified after the saturation or during longer experiments. Therefore, the possibility to intrinsically determine the water content via closed-flow experiments renders beneficial in reducing the experimental effort by avoiding the need to verify the water content by repeated weightings.

In addition, this way in determining the water content from BTC data obtained in closed-flow mode avoids the need to dry the porous medium prior to saturation, which is mandatory for a solid quantification with gravimetric methods, e.g. weighting of the solution supply vessel during the saturation. As discussed in section 1.3, this is a major drawback in classical approaches. The quantification of the water content from temporal moments is also possible in open-flow mode. However, this methodology strictly depends on the knowledge of the pumping rate (Koestel et al. 2011). In addition, the correct determination of the first normalized moment may be obscured by preferential flow (Kamra and Lennartz 2005) and is severely affected by data truncation (Young and Ball 2000). An observation that can be attributed to the water content uniquely, i.e. the equilibrium concentration in closed-flow experiments, is an important gain to solve this issue. The sensitivity analysis shown in Figure 4.2 underlines that the pumping rate and the water content are linearly correlated in open-flow experiments when reconstructed from BTC

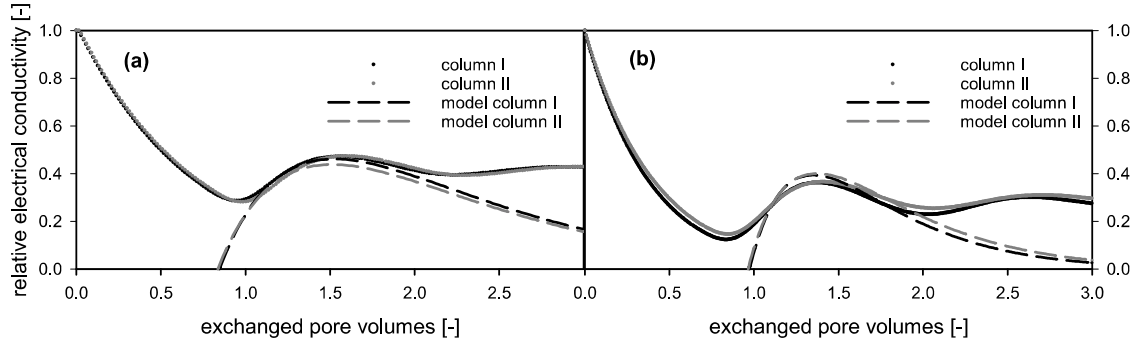


Figure 4.3: Illustration of the model used for the reconstruction of the BCM at $V_{\text{mix}} = 30 \text{ mL}$ (a) and at $V_{\text{mix}} = 20 \text{ mL}$ (b), note the inappropriate representation of the measurements far from the oscillation maximum.

data. In contrast, both parameters are strictly independent when reconstructed from BTC data obtained in closed-flow mode. The possibility to determine the water content is especially useful when the saturation changes during a set of successive experiments with the same porous medium. Repeated conservative tracer experiments conducted in order to characterize the porous medium (Weigand et al. 2002) would always provide the water content when performing them in a closed-flow mode.

4.1.3 Determination of the Breakthrough of the Center of Mass

The dataset recorded for different mixing vessel volumes also offers the possibility to verify the approach to reconstruct the BCM from BTC data given in section 2.4.2 experimentally. As expected, the first oscillation maximum $t_{\text{pv}}^{\text{max}}$ is not constant and appears slightly below 1.6 pv for tracer tests with a mixing vessel volume of 30 mL ($d_v = 0.41$), which decreases to around 1.4 pv for experiments carried out at a mixing vessel volume of 20 mL ($d_v = 0.27$). After reconstruction of the breakthrough of the center of mass with Equation (2.80), this difference is compensated for by the inclusion of k , i.e. the relation of water-filled pore space and the mixing vessel solute volume, and results from 1.03 to 1.04 are achieved for R (Table 4.2). This seems plausible concerning the expected value of 1 for conservative tracers and proves the reliability of estimates for the breakthrough of the center of mass determined in the proposed way. However, the slight bias towards higher values is likely due to the neglect of dispersion and diffusion. Especially for non-symmetrical pulses, which are expected in closed-flow experiments due to the dynamic inflow boundary, dispersion and diffusion might also shift the BCM and cause a apparent R higher than unity even in case of conservative transport.

The exact localization of the first oscillation maximum was not possible for experiments with $V_{\text{mix}} = 100 \text{ mL}$ implying that this method is not applicable for $d_v > 0.5$, where no oscillations are expected (Figure 4.1 a).

An illustration on the performance of the applied model according to Equation (2.75) is shown in Figure 4.3. The model fits the measurements only near the oscillation maximum regarding the location of the first maximum. Other features of the experimental BTC are not represented well, which reminds of the assumptions made in the derivation of this method and its intention to only describe the position of first oscillation maximum appropriately. However, only the model describing the phase of the BTC from 1 pv to 2 pv is shown here and therefore it is only valid in this range. Large part of the differences seen in Figure 4.3 are outside this range and a comparison to the model would require the calculation of the corresponding phase according to Equation (2.76).

Table 4.2: Reconstruction of retardation from the first oscillation maximum.

Experiment Column	$V_{\text{mix}} = 100 \text{ mL}$		$V_{\text{mix}} = 30 \text{ mL}$		$V_{\text{mix}} = 20 \text{ mL}$	
	I	II	I	II	I	II
k	0.66	0.64	1.48	1.44	2.68	2.46
measured $t_{\text{pv}}^{\text{max}}$	-	-	1.56	1.58	1.38	1.41
reconstructed R	-	-	1.03	1.04	1.03	1.04

4.2 Experiment B: Different Flow Velocities

During the initial stage of an arbitrary tracer experiment, the concentration in the mixing vessel decreases solely due to dilution until the arrival of the first solute breakthrough that causes a gradient in the effluent. During this stage, the assumption made in the derivation of Equation (2.70) are valid and the pumping rate can be reconstructed. Specifically, data smaller than 0.5 pv was fitted to Equation (2.70) with the Levenberg-Marquardt algorithm for the experiments carried out with different mixing vessel volumes, in which also the pumping rate varied. Since the initial concentrations and V_{mix} were measured, the only unknown in Equation (2.70) is Q . As the assumptions from Equation (2.70) still hold, the backward BTC allow for the same procedure.

To verify this approach for experiments, where only the pumping rate varies, another forward and backward breakthrough was recorded using the same columns as for the experiment with different mixing vessel volumes, now using a mixing vessel with $V_{\text{mix}} = 20 \text{ mL}$ with a sixfold pumping rate. The obtained BTC are almost identical to those obtained at the slower pumping rate after scaling to exchanged pore volumes, rendering diffusion of minor influence (Figure 4.4). The model according to Equation (2.70) was perfectly able to reconstruct the measurements for all BTCs, regardless if measured as forward BTC (Figure 4.5 a) or backward BTC (Figure 4.5 b). Consequently, the assumption of the exponential behavior of the initial part of the mixing vessel BTC of closed-flow experiments is valid and the reconstruction of pumping rates by the application of this model is very robust.

A comparison to the measured pumping rates is given in Table 4.3. Most of the reconstructed pumping rates slightly differ from those measured gravimetrically without any obvious systematic trend. Since the reconstruction from BTC data can be considered an online acquisition, it is closer to the “real” pumping rate, because abrasion may lead to a different effective tube diameter when performing the pumping rate test before or after the experiments. This highlights the need to assess the actual pumping rate promptly before or after an outflow experiment and is especially relevant for studies involving

Table 4.3: Reconstruction of the pumping rate from the initial exponential BTC.

Experiment Column	$V_{\text{mix}} = 100 \text{ mL}$		$V_{\text{mix}} = 30 \text{ mL}$		$V_{\text{mix}} = 20 \text{ mL}$	
	I	II	I	II	I	II
measured Q	66.4 ± 1.1	66.1 ± 1.1	66.5 ± 1.1	69.3 ± 1.1	33.2 ± 1.1	33.3 ± 1.1
forward	63.65 ± 0.07	63.77 ± 0.05	63.8 ± 0.3	66.8 ± 0.4	32.00 ± 0.03	33.22 ± 0.01
backward	-	-	68.7 ± 0.3	71.6 ± 0.2	32.1 ± 0.1	31.7 ± 0.1
measured Q	-	-	-	-	215.9 ± 1.1	203.9 ± 1.1
forward	-	-	-	-	210.8 ± 1.0	211.5 ± 1.0
backward	-	-	-	-	215.7 ± 1.9	222.1 ± 0.8

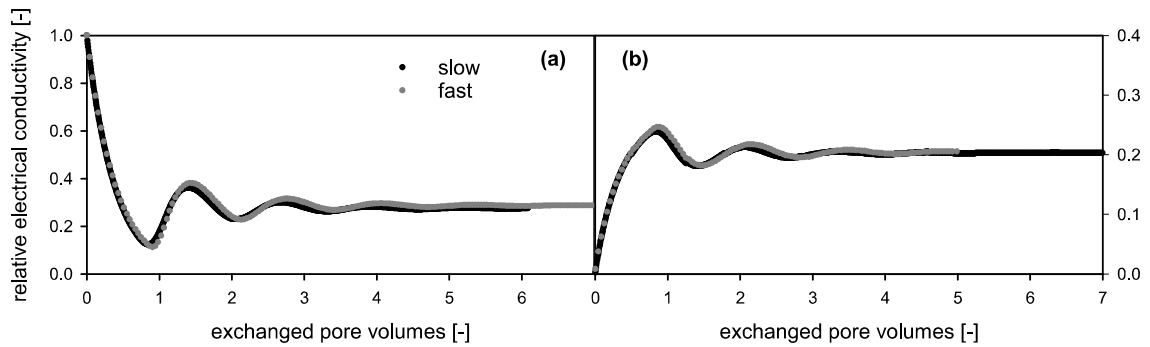


Figure 4.4: Forward and backward BTCs obtained at two different pumping rates with the same mixing vessel volume of 20 mL.

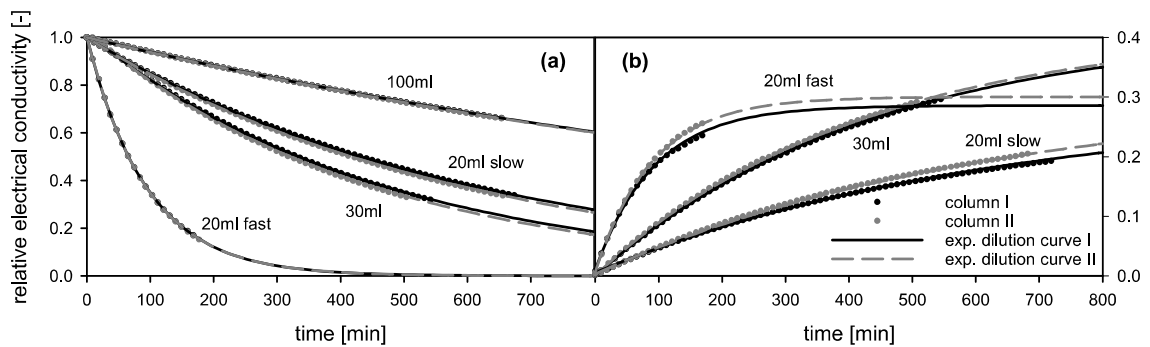


Figure 4.5: Comparison of the model for exponential dilution (lines) and measured forwards BTCs (dotted) obtained at different pumping rates and mixing vessel volumes for forward (a) and backward (b) breakthroughs.

retarded transport, where a correct pumping rate is crucial to calculate the exact amount of exchanged pore volumes needed for the evaluation of the BCM.

In classical approaches, the independent determination of the flow rate is possible by weighting of the solution supply or the volume of outflow over time without much effort. However, for closed-flow experiments, this assessment is not possible due to the recirculation and the resulting constant volumes in both, the column and the mixing vessel. The determination of the flow rate from BTC data is therefore feasible and the closed-flow approach exhibits no drawback in this context, since data collected before the exchange of 0.5 pv is usually uninformative regarding the transport properties and can be used for this purpose in a solid manner. However, the initial exponential decrease is only observable in the mixing vessel as the effluent is initially free of tracer comparable to BTCs in open-flow experiments. Thus, the pumping rate is not directly imprinted on the effluent BTC and the mixing vessel BTC can be considered more directly indicative than the effluent BTC. However, as shown with the sensitivity analysis in Figure 4.2 b, no correlation of the water content and the pumping rate appears in closed-flow mode, regardless if the BTC is

measured in the effluent or in the mixing vessel. This is explained by the fact that although the first breakthrough observed in the effluent BTC is determined by both, the pumping rate and the water content, the water content uniquely imprints on the equilibrium dilution. This annihilates the correlation and the effluent BTC provides the same information as the mixing vessel BTC in agreement to Equation (2.67) and Equation (2.68), which imply the conversion from one BTC to the other.

4.3 Model Validation for Closed-Flow Experiments

The proposed numerical model was applied to the BTCs obtained with different mixing vessel volumes and pumping rates. In this way, all relevant boundary conditions that may affect the BTC of a closed-flow experiment are screened. For the water content and the flow rate, the known values resulting from the calculations described in the previous sections were used. The only parameter subjected to fitting was consequently the dispersion length as no source and sink processes were involved. An excellent agreement between model and observed BTC was achieved for all conducted experiments (Figure 4.6). The resulting R^2 was above 0.995 for all experiments and the relative error in mass balance of the solute was below 0.1%.

The fitted dispersion lengths are found in the range between 1 mm and 1 cm, which are typical values for homogeneously packed sand columns (Hu and Brusseau 1994). The experiments carried out with a mixing vessel volume of 100 mL showed a strong increase in dispersion lengths, presumably caused by the lack of sensitivity of the BTC with regard to dispersion at these boundary conditions. This is reflected in the small visual difference of the replicates causing such strong variation. An overview of fitted parameters is given in Table 4.4.

As a result, the validity of the model regarding the mixing in the mixing vessel and the coupling of the dynamics inside the mixing vessel to the solute transport in the porous medium can be assumed. Furthermore, the dynamic influent is sufficiently covered by Equation (2.66). As the extension of the transport model by additional processes does not affect the process of dilution in the mixing vessel and therefore the numerical implementation of the closed-flow dynamics, this model is also applicable with any additional transport process.

Table 4.4: Parameters obtained from the inverse modeling of BTCs at different mixing vessel volumes.

Experiment Column	$V_{\text{mix}} = 100 \text{ mL}$		$V_{\text{mix}} = 30 \text{ mL}$		$V_{\text{mix}} = 20 \text{ mL}$	
	I	II	I	II	I	II
fitted λ [mm]	1.22 ± 0.06	4.39 ± 0.10	0.26 ± 0.04	0.17 ± 0.04	0.66 ± 0.02	0.98 ± 0.02
R^2 [-]	0.998	0.999	0.999	0.998	0.999	0.996
					fast pumping rate	
					0.50 ± 0.02	0.26 ± 0.04
					0.999	0.995

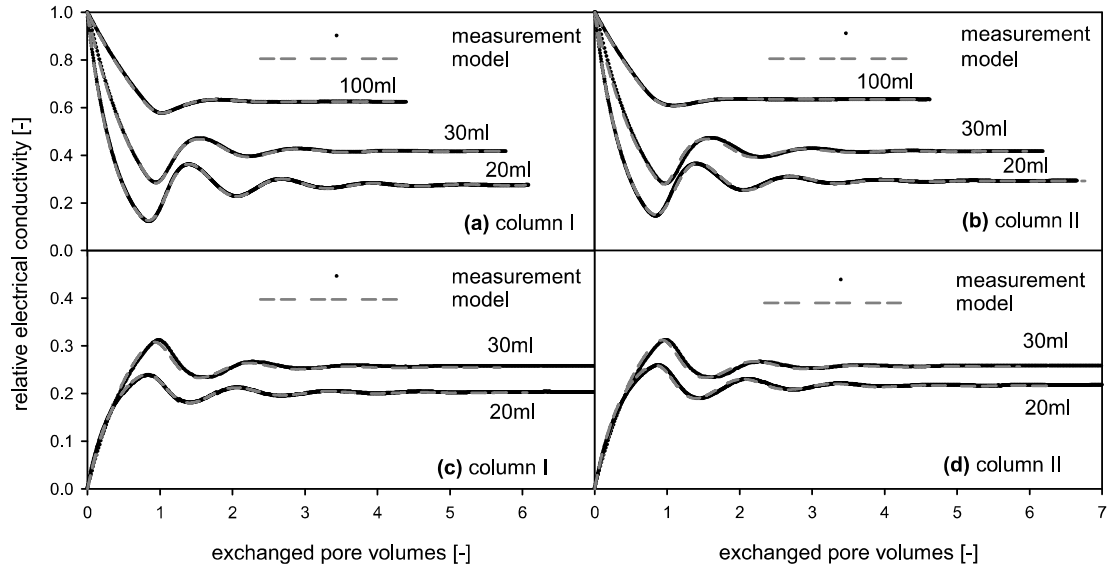


Figure 4.6: Simulated BTCs using fitted dispersion in comparison to measurements, forward breakthrough for column I (a), forward breakthrough for column II (b), backward breakthrough for column I (c) and backward breakthrough for column II (d).

4.4 Experiment C: Reactive Breakthrough

To investigate the behavior of reactive tracers, two columns (inner diameter: 4.1 cm, length: 10 cm) were set up in closed-flow mode using the ASQzGt medium and a mixing vessel with a solute volume of 30 mL. The bulk densities were 1.66 g cm^{-3} for both columns. Before the actual reactive tracer experiment, a BTC was recorded using the NaCl tracer. Both columns showed the typical behavior already described and discussed in the previous sections (Figure 4.7). Fitted transport parameters are given in Table 4.5. After rinsing of the columns with ultrapure water to remove remaining NaCl, vanillic acid was applied to the mixing vessels and the breakthrough was recorded spectroscopically in direct succession to the mixing vessel. As a result, the measured concentration represents the concentration present in the mixing vessel delayed by the time needed for the passage of the tubing to the flow-through cell used for the UV/Vis measurement. The delay is in the range of 0.02 pv to 0.04 pv and therefore only causes a small deviation to the observation expected in the mixing vessel. Additionally, the first two measurement were void of tracer, since the flow-through cell was initially filled with ultrapure water.

In comparison to the NaCl BTC, three major differences are evident when using the vanillic acid tracer. First, the oscillation shows a longer wavelength seen especially in the delayed first maximum. This points to the notable occurrence of retardation. Using Equation (2.80), column I shows $R = 1.45$ and column II shows $R = 1.33$. In comparison,

Table 4.5: Experimental parameters and values obtained from the inverse modeling of BTCs (marked with an asterisk) during the experiment with vanillic acid.

column	I (NaCl)	I (vanillic acid)	II (NaCl)	II (vanillic acid)
D [$\text{mm}^2 \text{ min}^{-1}$]	0.0017*	0.0015*	0.0015*	0.0011*
Q [$\mu\text{L min}^{-1}$]	96.7	96.7	94.7	94.7
θ [-]	0.448	0.448	0.444	0.444
ρ [g cm^{-3}]		1.65		1.66
f [-]		0.174*		0.055*
equilibrium sorption				
K_d [L mol^{-1}]		0.457*		1.124*
n_f [-]		1		1
R [-]		1.30*		1.23*
non-equilibrium sorption				
K_d [L mol^{-1}]		4.273*		9.134*
n_f [-]		0.517*		0.162*
Da [-]		0.133*		0.108*
k		1.971		1.954
$t_{\text{pv}}^{\text{max}}$		1.927		1.806
R using Equation (2.80)		1.45		1.33

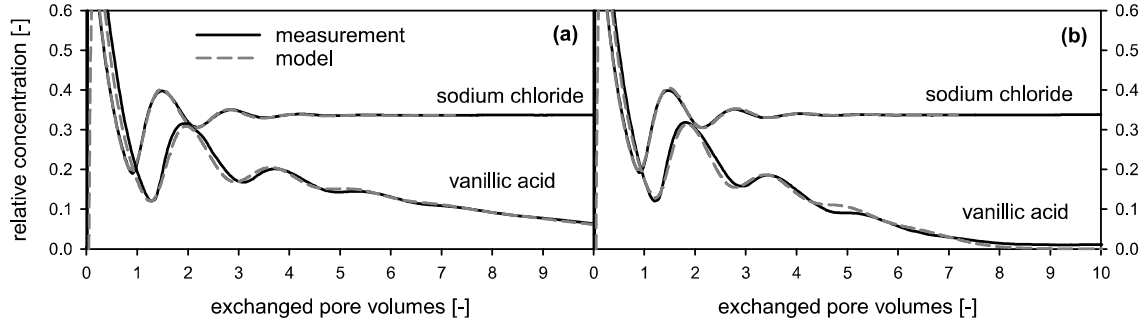


Figure 4.7: BTCs measured in the mixing vessel with $V_{\text{mix}} = 30 \text{ mL}$ using NaCl and vanillic acid as tracer for column I (a) and column II (b), model simulations shown as dashed line.

the retardation resulting from the inversely modeled equilibrium K_d value shows $R = 1.30$ for column I and $R = 1.23$ for column II, which is slightly below the estimation from the oscillation maximum. However, an additional retardation caused by the non-equilibrium interactions is likely and, as already shown, the estimation of retardation from the oscillation maximum is slightly biased towards higher values. A change in effective pumping rate that may produce a similar observation can be excluded since the initial exponential decrease that is uniquely attributable to the pumping rate is identical to the preliminary experiments with the NaCl tracer (Figure 4.7). Second, the concentration is significantly below the equilibrium concentration observed with the NaCl tracer. Therefore, in addition to the mixture of solutes, another sink acts on vanillic acid. To rule out a photodecay caused by the irradiation with UV light, a cuvette filled with the stock solution was repeatedly measured without any flow for two days after the experiments. There, no decrease in signal intensity was observed and the decrease in UV/Vis absorption can securely be attributed to (transport) processes inside the porous medium. Third, an approximately exponential decrease superposes the entire oscillation, leading to concentrations of vanillic acid near the detection limit for column II (Figure 4.7). Together, retardation and the lower concentration is evidence for liquid solid interactions, which at least partly obey a kinetic limitation seen in the exponential shape of the BTC after several pv. The slightly lower D values observed for experiments with vanillic acid can be attributed to the lower diffusion coefficient usually found for larger molecules.

Accordingly, the full two-site/two-region model as presented in Equation (2.25) to Equation (2.30) had to be used for the model simulation. The vast number of parameters describing the liquid solid interactions impeded an easy inverse modeling. Thus, local optimization strategies as successfully applied to conservative tracer experiments suffered from severe divergence and simulated annealing had to be applied to find the global optimum in parameter space (Table 4.5). For refinement and computation of confidence intervals, the solution from simulated annealing was used as initialization for the Levenberg-

Marquardt algorithm, which converges near the optimum. In this way, a satisfying model could be derived (Figure 4.7). However, the non-dimensionless parameters involved in liquid solid interaction are strongly correlated and may therefore not represent the underlying physical processes. Consequently, the calculation of confidence intervals that were usually given to other modeling results was omitted due to their irrelevance and non-uniqueness in correlated scenarios. Only the dimensionless parameters R of around 1.25 and Da of around 0.1 are reliable non-correlated results from the inverse modeling, also allowing their interpretation.

As stated in the introduction, closed-flow experiments are especially suited to maintain the feedbacks involved in liquid solid interactions. Regarding the chemical milieu, this becomes apparent with the presented experiment. The pH of the stock solution was 4.31 resulting from the deprotonation behavior of vanillic acid. If this tracer was used in an open-flow setup, the long-term state of the solution also inside the porous medium would converge to this pH assuming a limited buffer capacity that is expected for a finite soil profile. In comparison, the pH value inside the mixing vessel, which is assumed to be identical to the pH in the porous medium when the oscillation equilibrium is reached, increased to 5.25 for column I and to 5.27 for column II. Considering the acid/base chemistry of vanillic acid ($pK_a = 4.53$), most of the molecules in the stock solution are protonated, while the pH in equilibrium with the porous medium forces the presence of predominantly deprotonated vanillic acid. As the pH also impacts the surface charge of soil minerals (Kosmulski 2011), this result of equilibration of the aqueous solution with the solid mineral matrix may tremendously affect the kinetics and strength of sorption reactions (e.g. Schaffer and Licha 2015) and open-flow and closed-flow experiments are virtually incomparable in the reactive case.

4.5 Sensitivity Analyses

The validated model, which combines the ADE as described with Equation (2.25) to Equation (2.30) and the PDE describing the mixing vessel in Equation (2.66), offers the possibility to calculate the predicted behavior of the closed-flow design for boundary conditions that are difficult to investigate experimentally. Furthermore, a series of BTCs with slightly different parameters can be obtained in short time, a task that is elaborate and mostly redundant if carried out experimentally.

To give a comprehensive and exhaustive overview on the effect of decisive parameters on the shape of the BTC, often referred to as sensitivity, the following section will present series of model runs scanning parameters in a meaningful interval. To quantify the sensitivity in terms of the confidence interval, all numerical results were subjected to parameter fitting with the Levenberg-Marquardt algorithm. Although all parameters were provided to the simulation in the first place, the addition of noise might alter the actual optimum, and an optimization makes sense to investigate the performance of inverse models to recover those parameters.

The overview of BTCs will provide an intuition on the expected behavior of closed-flow experiments. In addition, important implications on the most ideal way of performing an experiment with different research interests will be derived.

This section contains numerical results on rate limitations, which are solely focused on liquid solid interactions. However, all aspects that are discussed there also apply to the model describing rate-limited exchange to immobile regions since the mathematical foundation is identical except the distribution coefficient of unity in the immobile regions. Consequently, exchange to immobile regions can be considered a special case of rate-limited interactions from a mathematical point of view and a separate discussion on exchange to immobile regions would be redundant.

4.5.1 Volumetric Dilution Factor

As shown in the experimental results, the damping of the oscillation amplitude depends on the dispersion and the mixing vessel volume. To extend these observations to a wider range of mixing vessel volumes, a numerical sensitivity analysis was conducted for a series of d_v values, which are the dimensionless representation of the mixing vessel volume. To fix the effect of dispersion, a Pe number of 100, an advection dominated transport regime in accordance to the conditions in the experimental part, was used.

As expected, all simulations show that the concentration always converges to equilibrium, given as a relative value by the corresponding d_v in case of conservative transport (Figure 4.8). Furthermore, hardly any oscillation can be seen for $d_v = 0.7$, whereas for $d_v = 0.5$ one, for $d_v = 0.3$ three and for $d_v = 0.1$ five maxima are clearly visible. This

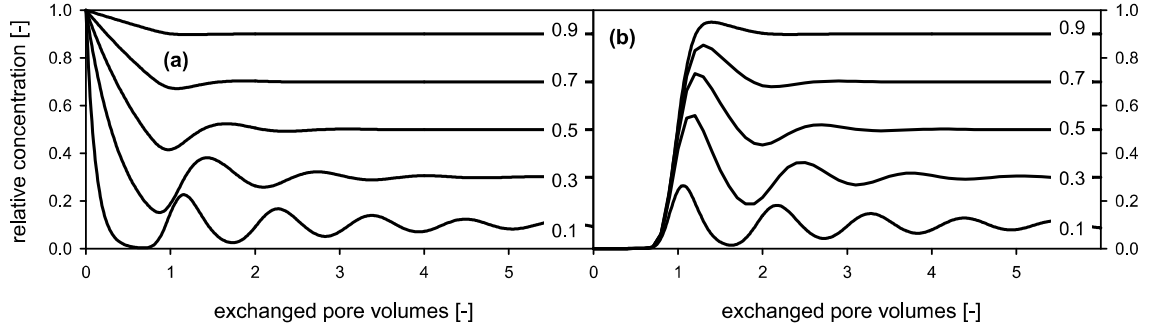


Figure 4.8: Simulated BTCs at different d_v at $Pé = 100$ observed in the mixing vessel (a) and the effluent (b).

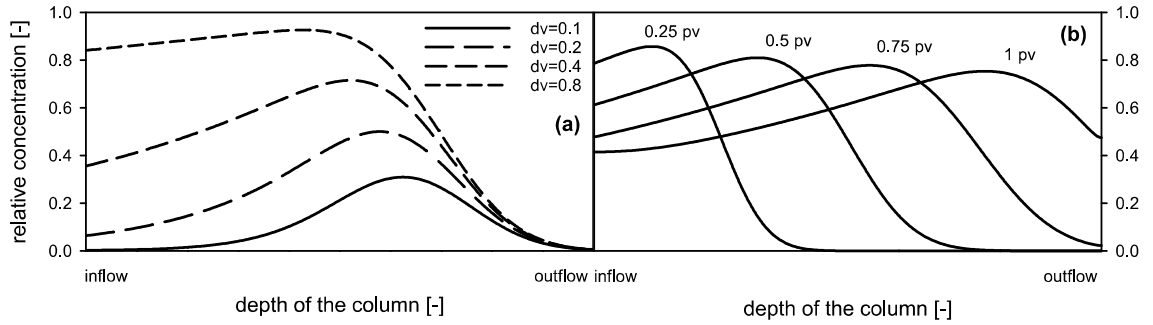


Figure 4.9: Simulated solute profiles along the column at d_v from 0.1 to 0.8 (a) after the exchange of 0.7 pv, and the development of the solute profile at $d_v = 0.5$ at successive time steps (b).

confirms the experimental observations that a ratio of unity between the volume of the mixing vessel and the volume of the water-filled pores (which results in $d_v = 0.5$) is the limit value for the effective emergence of oscillations in the BTC. Since d_v can be adjusted independent of the column geometry by choosing an appropriate volume of the mixing vessel, the appearance of oscillations can consequently be controlled by the experimenter.

One of the benefits from model simulations is the prediction of the dynamics to boundary conditions or places that elude a direct observation. As an example, the spatial distribution of the solute concentration and properties of the porous medium is only assessable with invasive methods or methods that are complex in data analysis and very expensive, e.g. electrical resistivity tomography (e.g. Wehrer and Slater 2015) or X-Ray/positron emission tomography (Olsen et al. 1999; Kasteel et al. 2000). Model simulations provide a fast and cheap tool to make predictions on such problems.

To illustrate the solute profile in the column of a typical closed-flow experiment, a series of models with different d_v was simulated and the solute distribution at 0.7 pv was recorded (Figure 4.9 a). With small mixing vessel volumes, the distribution resembles the shape of a

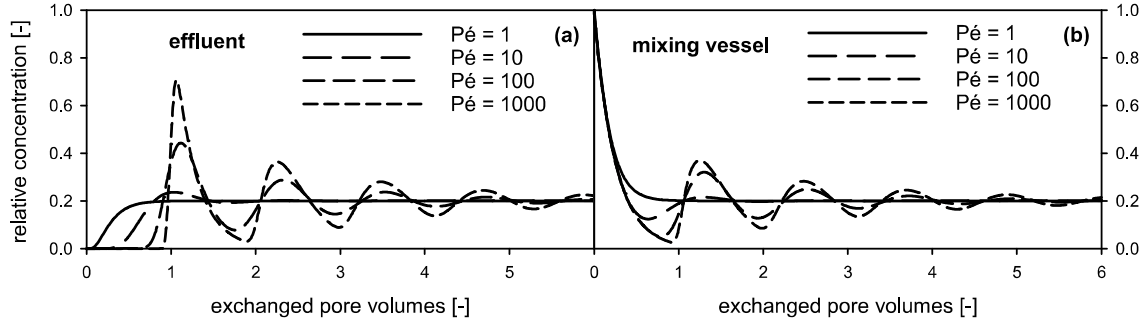


Figure 4.10: Modeled closed-flow BTCs in effluent (a) and mixing vessel (b) at $d_v = 0.2$ with $Pé$ numbers from 1 to 1000.

solute pulse, the typical expectation for open-flow experiments using a pulse-type boundary condition. However, with increasing mixing vessel volume the pulse-like shape is becoming asymmetrical with an increasingly heavy tailing towards the column inflow. This tailing is pronounced throughout the entire passage of the solute through the column (Figure 4.9 b). For mixing vessels that result in a d_v near unity, the distribution is similar to the sigmoidal CDF that is expected for continuous-feed boundary conditions in open-flow mode. To conclude, closed-flow experiments provide a continuum of boundary conditions from a pulse-type boundary to a continuous-feed boundary.

4.5.2 Dispersion

The dispersion of the porous medium is one of the most basic parameters describing the transport regime and the determination of dispersion related parameters is part of most studies on transport in porous media. The main effect that is caused by dispersion in open-flow experiments is the (sometimes asymmetrical) broadening of concentration gradients over time. As a result, the width of the travel-time PDF or CDF is mainly determined by the dispersion of the porous medium. A likewise flattening of concentration gradient is also found in closed-flow experiments regarding the oscillation amplitude, which is damped over time. However, this damping has already been shown to be massively affected by the mixing vessel solute volume. A thorough investigation on the effect of the dispersion, which probably also imprints in the oscillation damping, is therefore urgently needed to assess the performance of closed-flow experiments with respect to the determination of dispersion. In general, a higher apparent dispersion leads to a faster disappearance of oscillations and a low apparent dispersion leads to oscillations which are mainly damped out by the mixing process inside the mixing vessel (Figure 4.10).

As the extent of oscillations can be controlled by the experimental boundary conditions, specifically the mixing vessel volume, a likewise control over the sensitivity of the BTC to the apparent dispersion, which manifests as oscillation damping, seems likely. A higher

sensitivity is expected for small mixing vessels, where oscillations appear throughout the exchange of several pore volumes and a low sensitivity is suggested for large mixing vessel volumes, where hardly any oscillations are observable. Hence, a large influence on parameter uncertainty is expected for small mixing vessels since the effect of dispersion is imprinted on the whole range of visible oscillations in the BTC.

To investigate this, the sensitivity of the BTC was analyzed with regard to changes in the Pe number as representation of the apparent dispersion. This was done by producing an artificial dataset of BTCs at the effluent and the mixing vessel in closed-flow mode at a Pe number of 100 over the complete range of d_v values. To provide a comparison to the classical experimental approach, BTC data was produced under identical boundary conditions in open-flow mode. As d_v is not defined or meaningless in open-flow experiments, a likewise variation of d_v is consequently not possible. With this data as reference, the objective function was quantified as l_2 norm using model runs with Pe numbers covering the interval [50,200] surrounding the optimum of Pe by a factor of 2 (Figure 4.12 a-c). If the objective function shows a large gradient with respect to changes in the Pe number, the system is considered more sensitive and an appropriate optimization algorithm would better be able to find the best fit within a small confidence interval.

As expected, the shape of the objective function is strongly related to the d_v value. Regarding the effluent data, the closed-flow mode shows a strong sensitivity for d_v values from 1 to 0.1 (Figure 4.12 a), i.e. if the contribution of the mixing vessel solute volume to the total solute volume is between 100% and 10%. At very high d_v values, the closed-flow mode experiment is very similar to the corresponding open-flow scenario with respect to the shape of the objective function. This is plausible concerning the shape of the open-flow BTC, which is very similar to the closed-flow BTC at d_v values approaching unity (Figure 4.8 b). A decrease in d_v , i.e. a decrease in mixing vessel volume, leads to a flat objective function and thus, a low sensitivity. When using the mixing vessel BTC data, a comparable sensitivity is only achieved at a d_v of approximately 0.1 (Figure 4.12 b). Larger as well as smaller mixing vessel volumes corresponding to this d_v show a generally low sensitivity. A closed-flow experiment with mixing vessel volumes resulting in a d_v around 0.1 are therefore considered the most sensitive with respect to dispersion, regardless if measured in the effluent or the mixing vessel. In comparison to open-flow experiments (Figure 4.12 c), no superior sensitivity is shown even for closed-flow mode experiments at this particular d_v .

However, such a result is only found for “perfect” artificial data, where an objective function of 0 can be achieved. As this situation is not found for “real” experimental data, the data was disturbed with white noise at a standard deviation of 0.5%, 1% and 3% relative to the respective value. Here, the sharp valley of the objective function in open-flow mode, which causes small parameter uncertainty for the optimal value, quickly

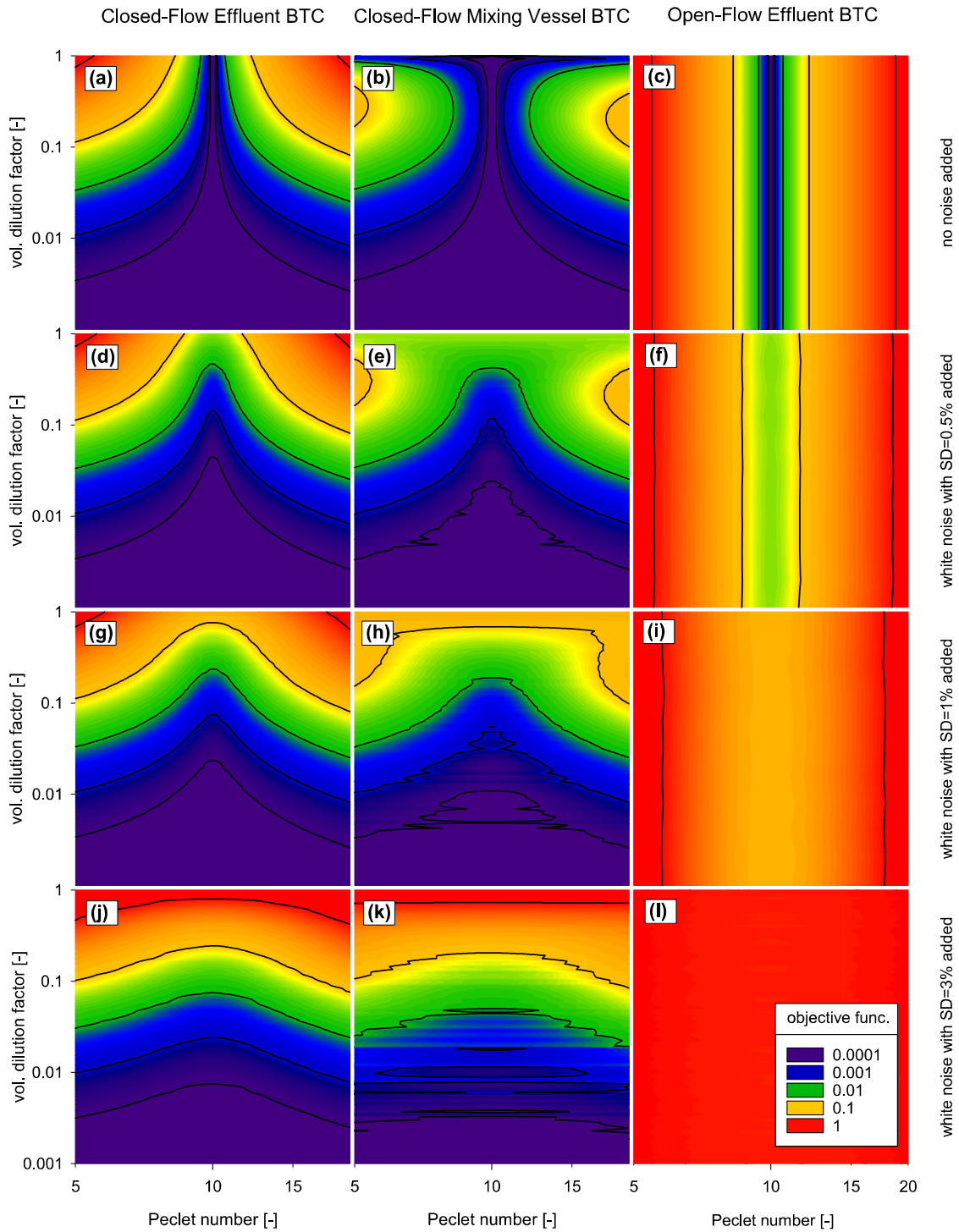


Figure 4.11: Surface of the objective function with respect to changes in the Pe number around the optimal value of $Pe = 10$ for d_v values from 0.001 to 1. Each column represents a different mode of measurement (from left to right: closed-flow effluent, closed-flow mixing vessel, open-flow effluent). Each row represents results at different noise levels (from top to bottom: no noise, 0.5% noise, 1% noise, 3% noise).

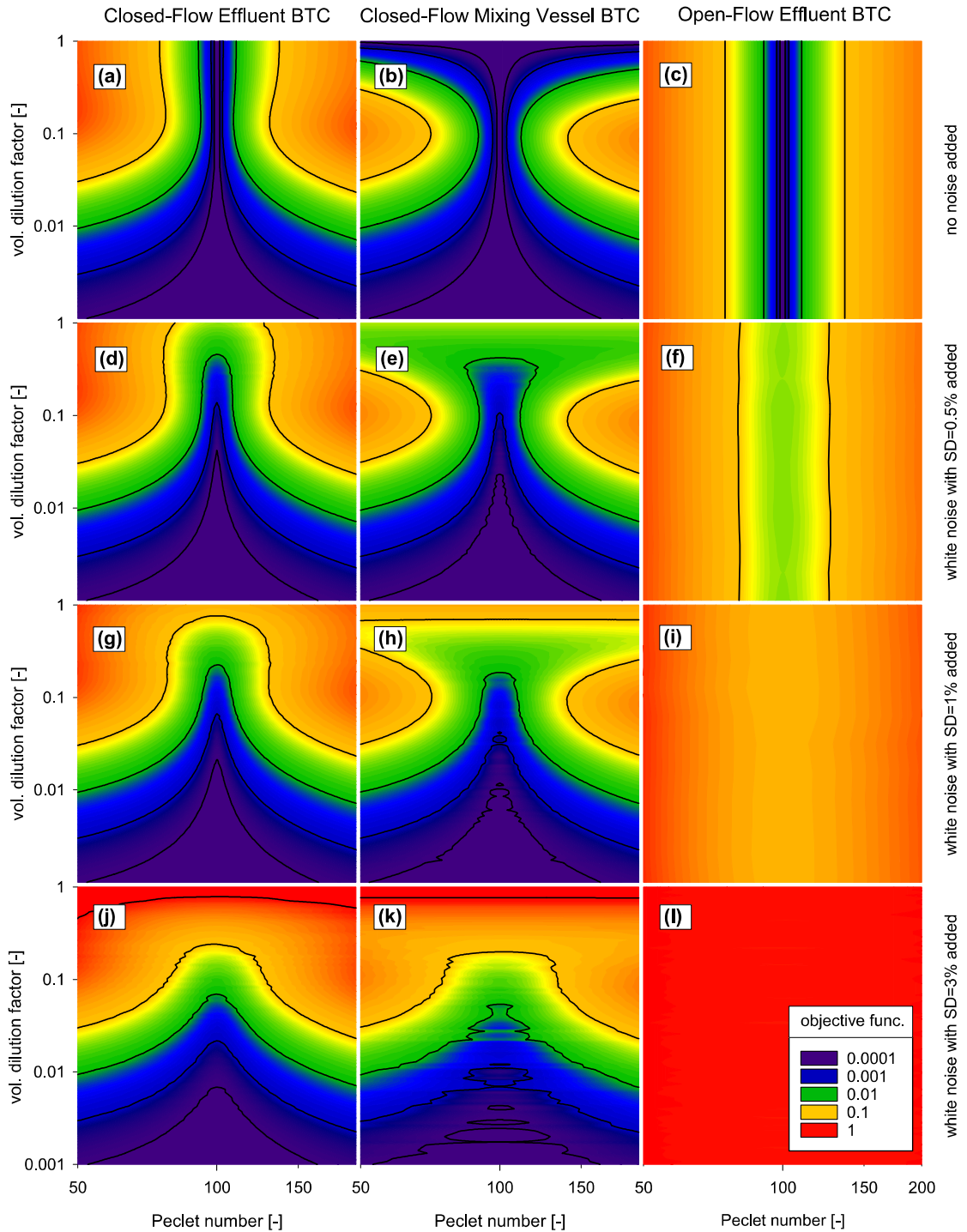


Figure 4.12: Surface of the objective function with respect to changes in the Pe number around the optimal value of $Pe = 100$ for d_v values in the interval $[0.001, 1]$. Each column represents a different mode of measurement (from left to right: closed-flow effluent, closed-flow mixing vessel, open-flow effluent). Each row represents results at different noise levels (from top to bottom: no noise, 0.5% noise, 1% noise, 3% noise).

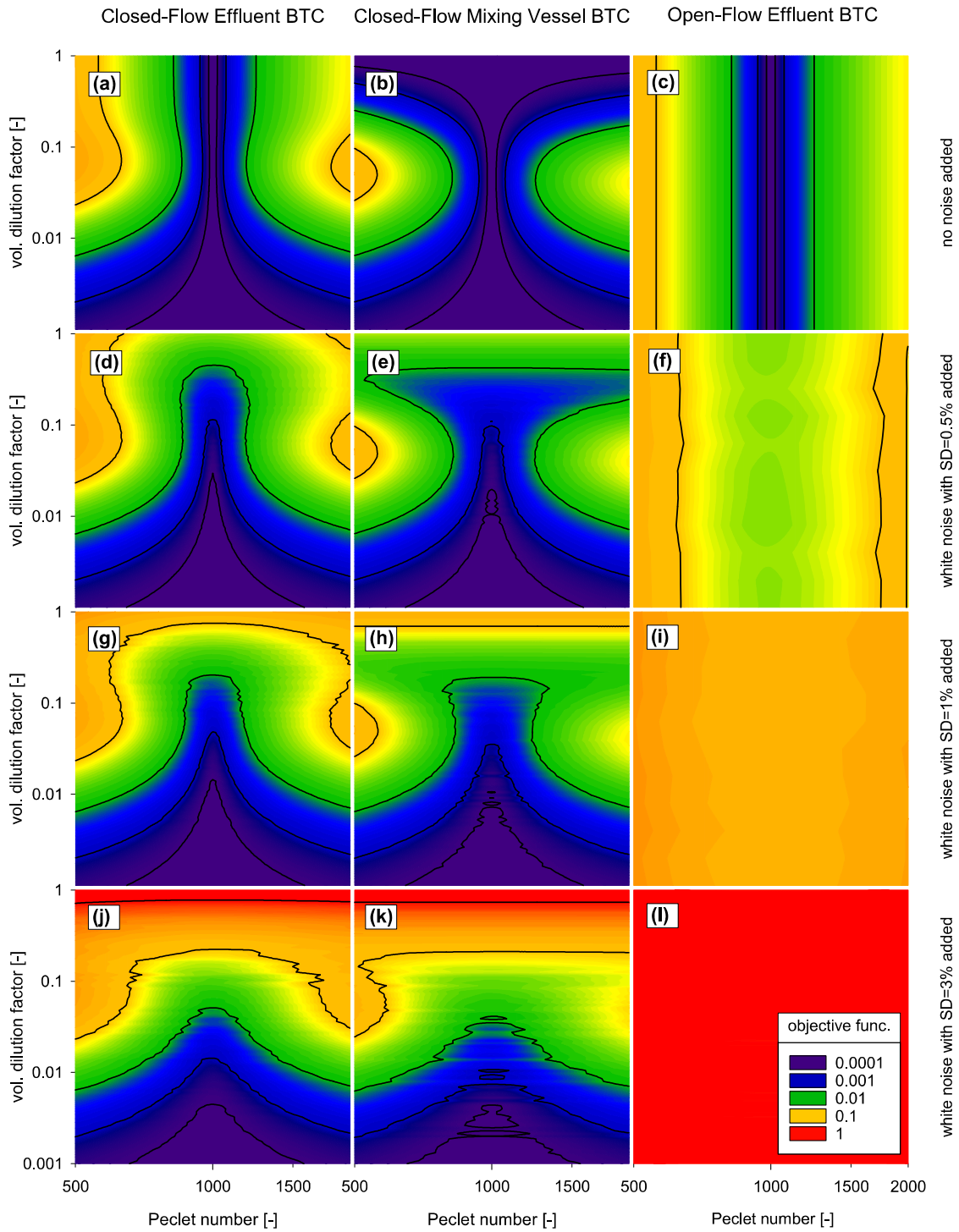


Figure 4.13: Surface of the objective function with respect to changes in the $Pé$ number around the optimal value of $Pé = 1000$ for d_v values from 0.001 to 1. Each column represents a different mode of measurement (from left to right: closed-flow effluent, closed-flow mixing vessel, open-flow effluent). Each row represents results at different noise levels (from top to bottom: no noise, 0.5% noise, 1% noise, 3% noise).

collapses and a much flatter objective function is found (Figure 4.12 f,i,l). In contrast, the sensitivity in closed-flow mode, both for measurements in the effluent and the mixing vessel, is maintained to a large extent despite noise in the data (Figure 4.12 d,e,g,h,j,k). Only for d_v approaching unity, i.e. for very large mixing vessel volumes, a likewise flattening in the objective is observable. At the most optimal mixing vessel volume corresponding to a d_v of 0.1, the addition of noise has only minor effects. As a result, the parameter uncertainty in closed-flow experiments is significantly smaller already with addition of very low amounts of noise (Table 4.6). As a rule of thumb, measurements in the effluent perform twice as sensitive as compared to measurements in the mixing vessel.

For this reason, the most sensitive approach for a determination of dispersion in closed-flow mode is by measuring the effluent concentration using a mixing vessel corresponding to a d_v of around 0.1. Simulations with $Pé$ numbers of 10 and 1000 showed a very similar behavior (Figure 4.11, Figure 4.13). An overview of resulting confidence intervals is given in Table 4.6.

The decrease in uncertainty of model inversion can be explained by the information content of the closed-flow BTC. The entire BTC with visible oscillations is sensitive to dispersion (Figure 4.10) and therefore the inversion algorithm can incorporate more indicative data. As an analogous interpretation, the closed-flow experiment can also be regarded as a multiple breakthrough experiment since the solute pulse travels through the column more than once and the decrease in uncertainty is caused by the intrinsic “replicate” determination.

Table 4.6: Fitted $Pé$ number at $Pé = 1$, $Pé = 10$, $Pé = 100$ and $Pé = 1000$ and fitted R at $R = 2.0$ and $R = 10$ with 0.95-confidence interval from noisy artificial data in open-flow effluent mode (OF), closed-flow effluent mode (CF) and closed-flow mixing vessel mode (CF_m) at $d_v = 0.1$.

$Pé$ noise	1			10		
	0.1%	0.5%	1.0%	0.1%	0.5%	1.0%
OF	0.999 ± 0.002	1.00 ± 0.01	1.00 ± 0.02	10.00 ± 0.01	9.97 ± 0.06	10.0 ± 0.1
CF	1.000 ± 0.001	0.999 ± 0.004	1.003 ± 0.007	10.001 ± 0.004	9.99 ± 0.02	10.01 ± 0.04
CF _m	1.000 ± 0.001	1.000 ± 0.006	1.00 ± 0.01	9.997 ± 0.006	10.01 ± 0.03	10.01 ± 0.06
$Pé$ noise	100			1000		
	0.1%	0.5%	1.0%	0.1%	0.5%	1.0%
OF	100.0 ± 0.2	100.1 ± 0.8	99 ± 2	999 ± 3	1000 ± 15	1010 ± 30
CF	100.00 ± 0.02	100.02 ± 0.08	99.9 ± 0.2	999.8 ± 0.3	999 ± 2	998 ± 4
CF _m	100.00 ± 0.03	100.0 ± 0.2	99.9 ± 0.3	1000.0 ± 0.7	1001 ± 4	1003 ± 7

4.5.3 Linear Liquid Solid Interaction

To investigate the effect of liquid solid interactions, the following simulations were carried out with linear equilibrium sorption corresponding to retardation factors ranging from 1 to 3. To provoke strong oscillations that still damp out after a few pore volumes, a d_v value of 0.3 was chosen. With increasing retardation, the first oscillation maximum is delayed and the oscillation wavelength increases nearly linearly (Figure 4.14 a). In accordance to observations and simulations of conservative transport, the concentration also converges to equilibrium. However, this equilibrium now also depends on the interaction between liquid and solid phase. This is reflected in the lower final concentration for increasing sorption strengths (Figure 4.14 a). As the initial concentration in the column is zero in both, the liquid and the solid phase, the whole initial amount of substance is given by the mixing vessel, a mass balance can be used to reconstruct the sorption coefficient S from the equilibrium concentration according to Equation (2.60). Since d_v is needed for this calculation, it has to be derived independently when performing an experiment, e.g. by measuring the dilution of a conservative tracer or by the calculation from the known water content with Equation (2.49). As a result, the equilibrium in closed-flow experiments offers a way to evaluate liquid solid interactions by comparing the dilution expected for a mixture of conservative solutes, represented by d_v , and the actually observed dilution. All S calculated according to Equation (2.60) are in perfect accordance with the R used for each particular simulation, which is to be expected since liquid solid interaction was simulated as only sink. However, a careful consideration of further sinks, which would imply an extension of the mass balance, is necessary to avoid any misinterpretation when applied to experimental data.

Regarding experiment C with goethite and the vanillic acid tracer, the delayed appearance of the first oscillation maximum was also observable, but the quantification of sorption strength via mass balances could not be applied since, unlike in the presented numerical data, no stable equilibrium was established due to slow sorption kinetics.

To summarize, in closed-flow mode, liquid solid interactions are seen as prolonged wavelength caused by retardation and lower equilibrium concentration. Both observations are independent and can be used separately to characterize liquid solid interactions. This can even be done without the application of numerical simulation, since S gives direct information on K_d as seen in Equation (2.34) and its calculation only relies on one unique observation, i.e. the relative dilution, and the knowledge of the water content.

The results from the sensitivity analysis regarding the apparent dispersion suggest that BTC data obtained in closed-flow mode also exhibits an altered sensitivity with respect to retardation caused by instantaneous linear liquid solid interaction. For this reason, an analogous sensitivity analysis has been carried out for $R = 2.0$ in the interval [1.5,2.5] (Figure 4.15) and for $R = 10.0$ (Figure 4.16) in the interval [9.5,10.5], both at a $Pé$ number

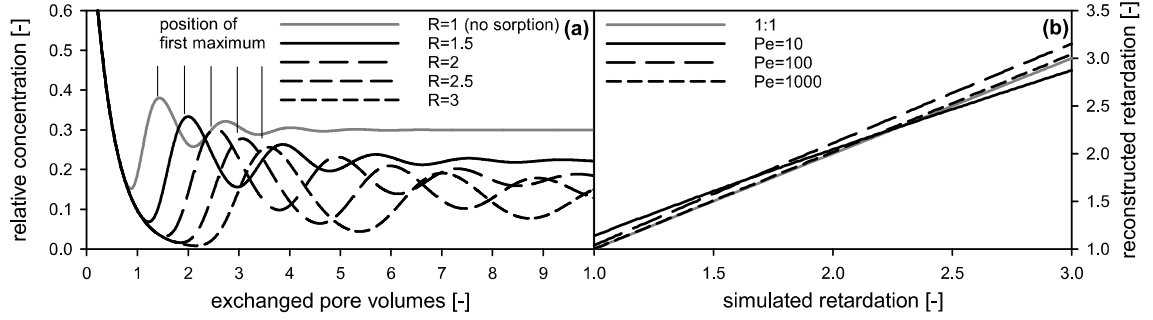


Figure 4.14: Simulated BTCs at different different R (a) and retardation reconstructed from the first oscillation maximum of modeled BTCs using retardations from 1 to 3 at different Pe numbers (b).

of 100. The surface of the objective function was calculated using d_v values in the interval $[0.001, 1]$ with noise added at a standard deviation of 0%, 0.5%, 1.0% and 3%.

The results are very similar to those acquired from the sensitivity analysis with respect to dispersion. Again, the sensitivity of the closed-flow setup with respect to retardation largely depends on the volumetric dilution factor and therefore on the solute volume of the mixing vessel. Specifically, a low d_v produces a flat objective function and thus, a low sensitivity, and increasing d_v values continuously produce steeper valleys in the objective function and thus, a higher sensitivity (Figure 4.15 a,b and Figure 4.16 a,b). Only a slight decrease in sensitivity at d_v values near unity is observed. This is in contrast to the sensitivity with respect to dispersion, which was becoming worse above $d_v = 0.1$ if measured in the mixing vessel due to the lack of information indicative for dispersion in the BTC. The retardation imprints on the oscillation wavelength as well as on the equilibrium concentration and therefore even closed-flow scenarios not showing any oscillations produce

Table 4.7: Fitted R at $R = 2.0$ and $R = 10$ with 0.95-confidence interval from noisy artificial data in open-flow effluent mode (OF), closed-flow effluent mode (CF) and closed-flow mixing vessel mode (CF_m) at $d_v = 0.1$.

R		2.0		
noise	0.5%	1.0%	2.0%	3.0%
OF	2.0002 ± 0.0006	1.9999 ± 0.0010	2.0000 ± 0.0008	1.999 ± 0.003
CF	2.00002 ± 0.00006	2.00009 ± 0.00010	2.0000 ± 0.0004	2.0002 ± 0.0004
CF _m	2.00002 ± 0.00008	1.99996 ± 0.00020	2.0000 ± 0.0005	2.0000 ± 0.0005
R		10.0		
noise	0.5%	1.0%	2.0%	3.0%
OF	10.000 ± 0.002	10.000 ± 0.002	10.000 ± 0.002	9.998 ± 0.008
CF	10.0000 ± 0.0002	9.9996 ± 0.0003	10.000 ± 0.001	10.000 ± 0.001
CF _m	9.9999 ± 0.0004	10.0003 ± 0.0008	10.000 ± 0.001	10.001 ± 0.003

BTC data that is sensitive with respect to retardation. For that reason, the sensitivity in closed-flow mode at very high d_v where no oscillations are present is nearly identical to the sensitivity in open-flow mode (Figure 4.15 a,b vs. Figure 4.15 c). This suggests that the closed-flow design using large mixing vessel volumes pretty much performs like an open-flow experiment with respect to the uncertainty in the determination of retardation, regardless if measured in the effluent or in the mixing vessel.

However, this valley producing this sensitivity at high d_v values in closed-flow mode is sensitive to the addition of noise and quickly vanishes with increasing amount of noise (Figure 4.15 d-l), comparable to the response of the objective function in open-flow mode. As a result, the closed-flow experiment performs most sensitive with noisy data at a d_v value of 0.1, where also the wavelength is indicative for retardation and repeated maxima are observable, thus reducing the uncertainty caused by noise (Figure 4.15 d,e,g,h,j,k and Figure 4.16 d,e,g,h,j,k). In agreement to the results with respect to dispersion, the uncertainty in the determination of retardation is decreased by an order of magnitude, when comparing an open-flow mode experiment with a corresponding closed-flow experiment measured in the effluent. Again, measurements in the effluent roughly perform twice as sensitive as measurements in the mixing vessel.

To sum up, the uncertainty of the inverse determination of retardation is decreased by an order of magnitude for closed-flow experiments measured in the effluent at $d_v = 0.1$ when compared to an analogous open-flow scenario in case of noisy data, regardless of the strength of retardation. Condensed results are given in Table 4.7.

Determination of the Breakthrough of the Center of Mass

To complete the investigation on the reconstruction of the BCM using the first oscillation maximum, a series of BTC was simulated covering k in the range from 0.1 to 10 and R in the range from 1 to 3. This represents experimental setups where the mixing vessel is ten times smaller than the water-filled pore space and vice versa. From these BTCs, the retardation was reconstructed using Equation (2.80). An overview of results is given in Table 4.8. As observed in the reconstruction from experimental data, all values are slightly

Table 4.8: Reconstructed R for simulated breakthroughs with different k and R .

$k \backslash R$	1.00	1.25	1.50	1.75	2.00	2.25	2.50	2.75	3.00
0.1	1.09	1.35	1.60	1.86	2.11	2.36	2.62	2.86	3.12
0.2	1.05	1.31	1.56	1.81	2.06	2.31	2.56	2.81	3.06
0.5	1.02	1.28	1.53	1.78	2.04	2.30	2.56	2.82	3.08
1.0	1.02	1.28	1.54	1.81	2.07	2.34	2.61	2.88	3.13
2.0	1.04	1.31	1.58	1.84	2.11	2.38	2.64	2.91	3.17
5.0	1.06	1.32	1.58	1.83	2.08	2.34	2.59	2.84	3.08
10	1.04	1.29	1.54	1.79	2.03	2.28	2.28	2.52	3.01

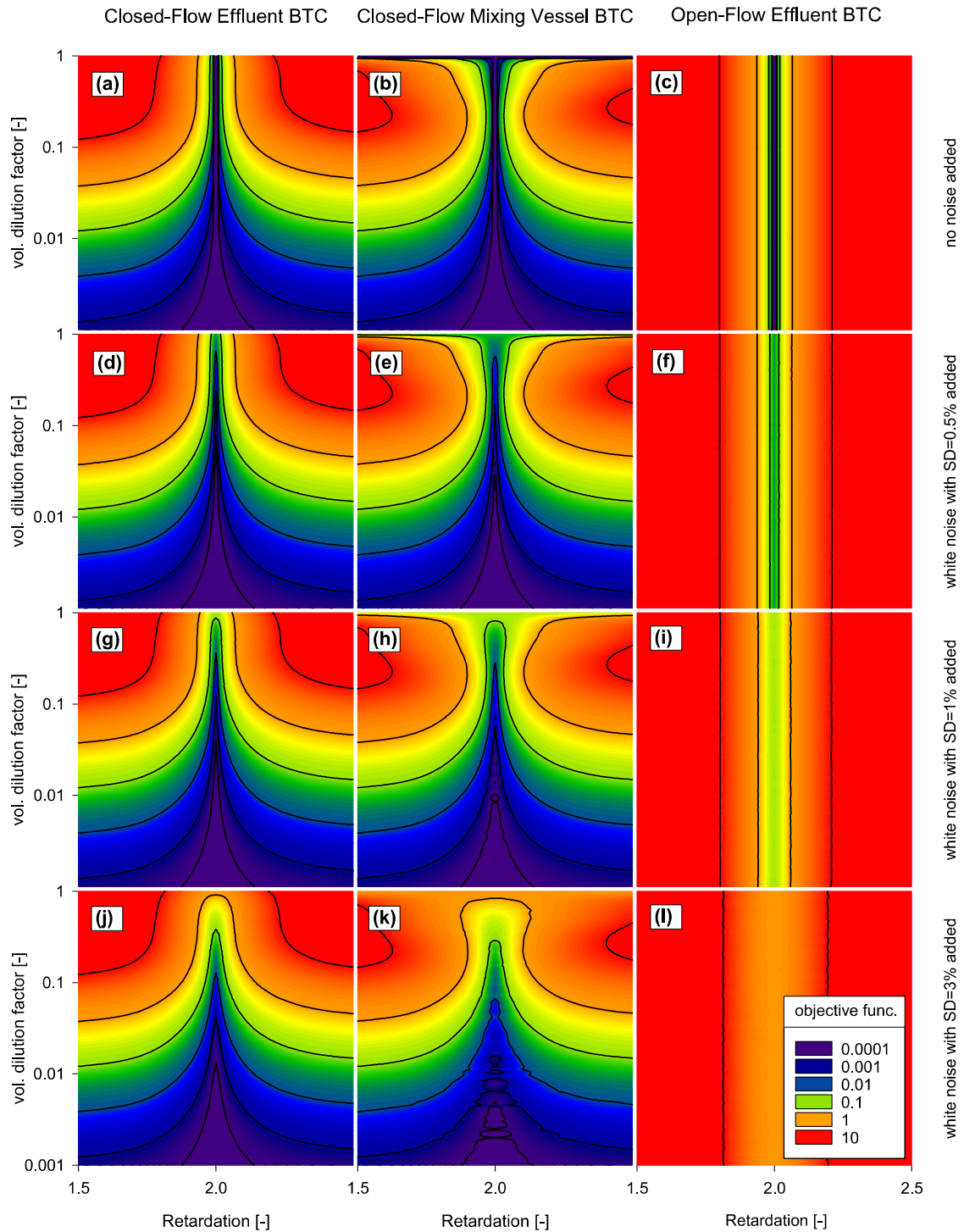


Figure 4.15: Surface of the objective function with respect to changes in R around the optimal value of $R = 2.0$ for d_v values in the interval $[0.001,1]$. Each column represents a different mode of measurement (from left to right: closed-flow effluent, closed-flow mixing vessel, open-flow effluent). Each row represents result at different noise levels (from top to bottom: no noise, 0.5% noise, 1% noise, 3% noise).

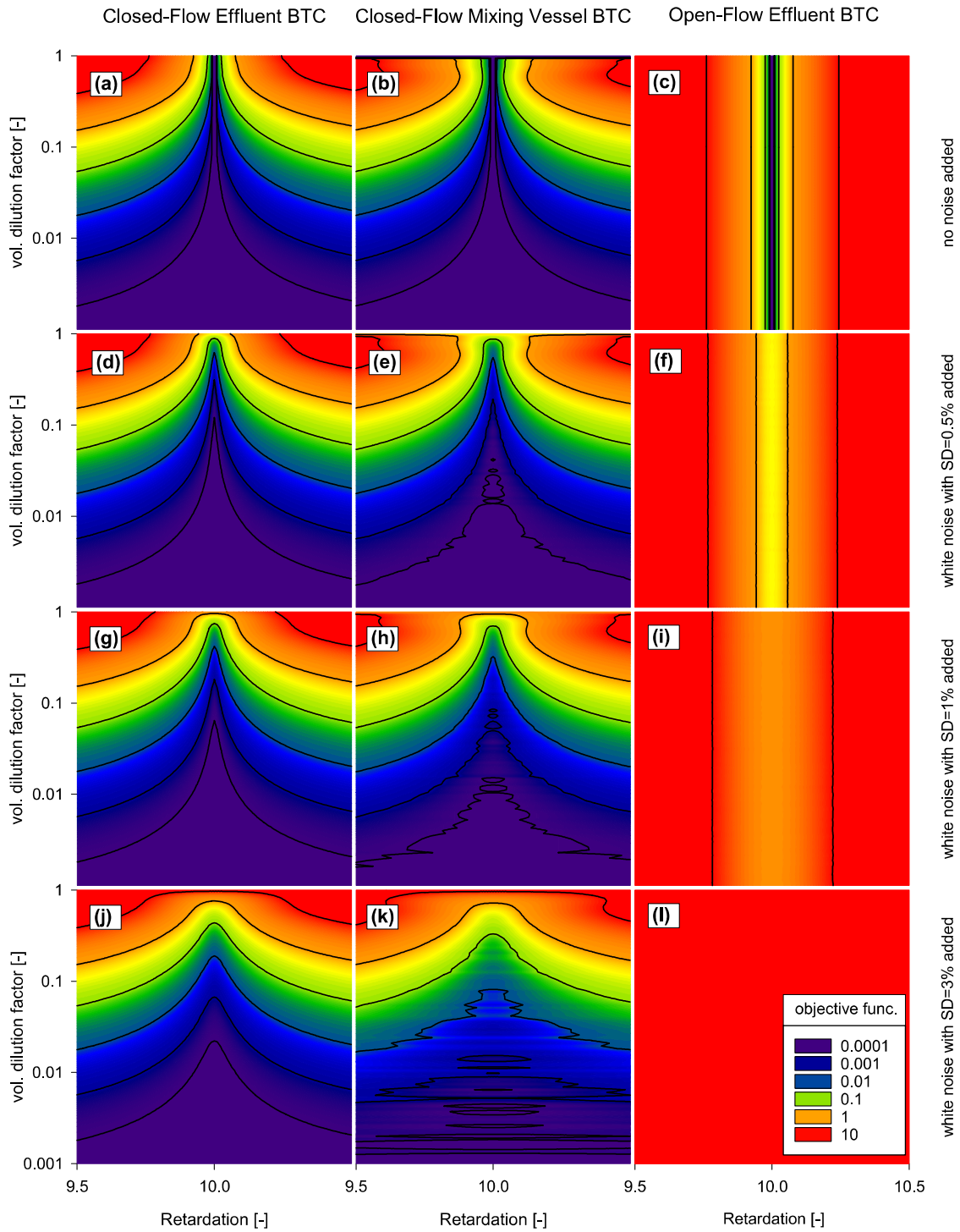


Figure 4.16: Surface of the objective function with respect to changes in R around the optimal value of $R = 10.0$ for d_v values in the interval $[0.001, 1]$. Each column represents a different mode of measurement (from left to right: closed-flow effluent, closed-flow mixing vessel, open-flow effluent). Each row represents result at different noise levels (from top to bottom: no noise, 0.5% noise, 1% noise, 3% noise).

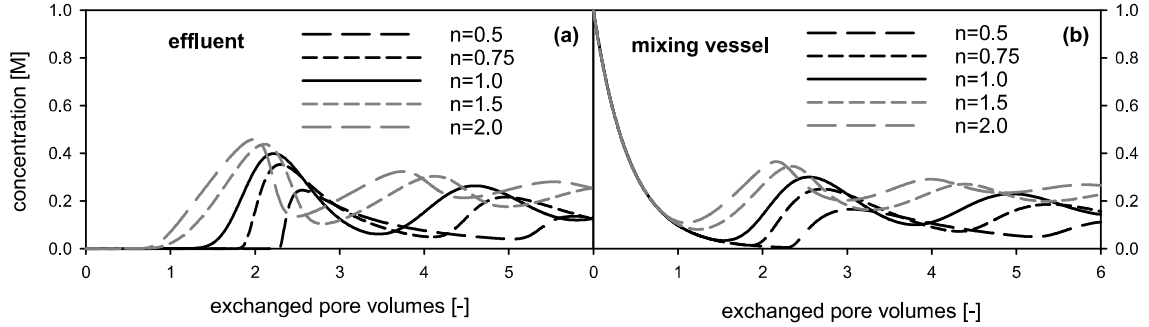


Figure 4.17: Simulated BTCs for varying degree of nonlinearity represented by the Freundlich exponent n_f for measurements in the effluent (a) and measurements in the mixing vessel (b).

higher than expected, which is due to the neglect of dispersion and diffusion. However, no systematic behavior with respect to different values of k and R is evident that permits the application of a general correction to the data. The reconstruction at different Pe numbers revealed a better reconstruction at higher Pe where diffusion is negligible (Figure 4.14 b).

4.5.4 Nonlinear Liquid Solid Interaction

To investigate the effect of nonlinear liquid solid interactions, the following simulations were carried out with equilibrium sorption using a Freundlich isotherm corresponding to a retardation factor of 2 in case of $n_f = 1$, i.e. linear interaction. To provoke strong oscillations that still damp out after a few pore volumes, again a d_v value of 0.3 was chosen. Then, BTCs were calculated in the effluent and the mixing vessel with $n_f = 0.5$, $n_f = 0.75$, $n_f = 1.0$, $n_f = 1.5$ and $n_f = 2.0$ to investigate nonlinear isotherms with increasing as well as decreasing slope (Figure 4.17).

The first difference between the calculated BTCs is the oscillation wavelength. This is explained by the different “effective” retardation that is caused by the slope of the isotherm with respect to the transported concentration. As a result, different amounts of substance are adsorbed and the observed retardation is not only linked to the K_f value as the retardation coefficient is mathematically only defined in case of linear isotherms. Another difference which is most obvious in the effluent (Figure 4.17 a) is the skewness or asymmetry of the oscillation. A nonlinear adsorption with decreasing slope for higher c , i.e. when $n_f < 1$, results in a strong positive skew or right-skew. On the other hand, an isotherm which has an increasing slope with increasing c produces BTCs with strong negative skew or left-skew.

The same situation is also found for BTCs in the mixing vessel, but to a considerably lower extent. There, only n_f values smaller unity produce a clear positive skew. A negative skew for n_f above unity is not pronounced. As isotherms of substances that are investigated

in soil science usually exhibit a nonlinearity represented by n_f values smaller unity, i.e. a decreasing slope for higher c (Limousin et al. 2007), this renders only a minor drawback of BTCs in the mixing vessel. Similar results were achieved when applying a Langmuir isotherm due the shape which often can be resembled partly by a Freundlich isotherm using appropriate parameters and $n_f < 1$. As the the degree of nonlinearity is the only investigated parameter that affects the oscillation asymmetry, any skew in the BTC is an indication of nonlinear interactions. BTCs obtained from open-flow experiments show a similar response to nonlinearity (Brusseau et al. 1989).

A sensitivity analysis with regard to the uncertainty of inverse modeling was not conducted for the following reasons. Nonlinear interactions do not scale linearly with concentration and thus, the effect of nonlinearity is highly dependent on the concentration range. As a result, modeling with normalized concentrations is not meaningful for the comparison of experimental performance. Furthermore, as the dilution inherent in the closed-flow design necessarily results in different concentrations as in open-flow experiments using the same initial tracer concentration, it is not clear what an analogous open-flow experiment exactly is. As a result, a comparison of both designs would be misleading and a conclusive analysis of sensitivity with respect to nonlinearity is not possible.

4.5.5 Damköhler Number

As rate limitations are fundamental in natural soils (e.g. Brusseau et al. 1991; Sardin et al. 1991; Beulke et al. 2004), a meaningful consideration of liquid solid interactions requires the addition of kinetics to the transport model (e.g. van Genuchten et al. 1974; de Wilde et al. 2008). Therefore, a series of BTCs was simulated with Da numbers ranging from 0.01 to 100, which corresponds to situations where the mean tracer residence time is 100 times smaller than the interaction rate and vice versa (Figure 1c). For comparability to previous simulations, a $Pé$ number of 100 and a d_v of 0.3 was used. The linear sorption coefficient was adjusted to theoretically result in a retardation coefficient of 2.

Experiments at low Da numbers between 0 and 1 show oscillations with a constant wavelength forced by the corresponding d_v . With increasing Da number, i.e. with increasing interaction rate, the amplitude gets damped stronger, leading to a complete absence of oscillations between $Da = 1$ and $Da = 10$ (Figure 4.18). This is caused by a balance between sorption and desorption. The removal of sorbate from the aqueous phase is then fast enough to decrease the pulse height while traveling through the column and slow enough to delay the release from the solid phase after the pulse has passed by around half of the time of the oscillation wavelength. This effect decreases the concentration maxima, and increases concentration minima and is similar to destructive interference in classical physics of waves. This damping effect can also be achieved by an increased dispersion. Thus, it is suggested that the equifinality with respect to dispersion versus rate limited interaction

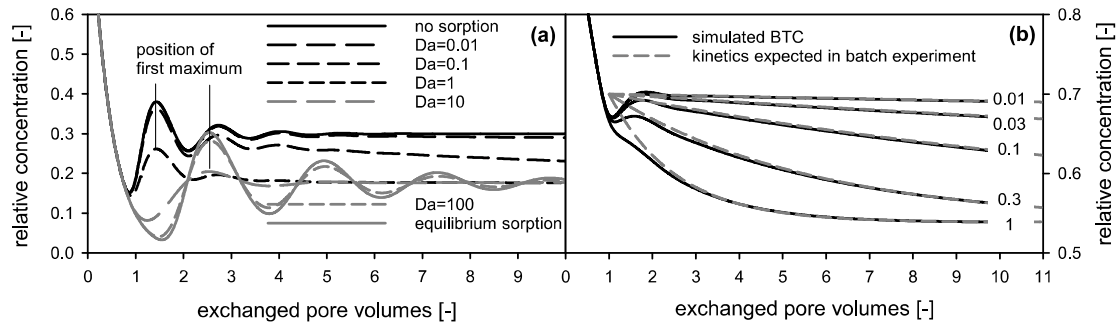


Figure 4.18: Simulated BTCs at different Da numbers (a) and BTCs at Da numbers from 0.01 to 1 compared to expected kinetics in completely mixed batch reactor experiment (b).

causing a broadening of concentration gradients is inherent in transport at these particular Da numbers and cannot be overcome by the application of closed-flow experiments. BTCs at Da numbers higher than 10, where the interaction rate approaches equilibrium, show stronger oscillations with a higher, but again, constant wavelength (Figure 4.18 a). Thus, slow sorption does not affect the oscillation wavelength at $Da < 1$, while at $Da > 10$, the mean transport velocity could be classified as dominated by equilibrium sorption. The range of intermediate Da numbers that do not allow a clear separation of equilibrium and non-equilibrium is smaller than reported for open-flow experiments (Wehrer and Totsche 2003) due to an observable that can uniquely be attributed to the mean transport velocity, i.e. the oscillation maximum. This clear distinction of transport velocity has implications for the assessment of effective retardation. Even though based on a continuous rate parameter and the same distribution coefficient, the mean transport velocity can be considered as either affected or not affected by the interaction.

Kinetics at Intermediate Damköhler Numbers

A closer look at intermediate Da numbers characterized by a non-oscillating BTC reveals that the establishment of the equilibrium concentration shows a distinct behavior, which can solely be attributed to rate limitation in liquid solid interactions (Figure 4.18 a). Especially at Da numbers smaller 1, a slow decrease in concentration is clearly visible after the oscillations have diminished. This is in perfect agreement to the observations made regarding the reactive tracer experiment with vanillic acid and the goethite/quartz medium with Da numbers around 0.1 (Figure 4.7). The direct interaction kinetics from within the porous medium is mirrored in the effluent since no other transport processes apparently influence the shape of the BTC. To investigate this feature without the strong interference of oscillations, the same experiments were simulated using $d_v = 0.7$ to increase the oscillation damping by the dilution in the mixing vessel. Then, the BTCs were compared to the development of concentration that is to be expected assuming the same sorption parameters

in a completely mixed batch reactor experiment, i.e. without transport (Figure 4.18 b). The result for different Da numbers show a nearly complete agreement of the simulated BTC with the prediction based on Equation (2.33) when the BTCs are shifted by one pore volume to emulate the time lag due to transport through the column.

As a result, it is possible to directly observe liquid solid interaction kinetics in an undisturbed porous medium when applying a closed-flow setup. Furthermore, as the sensitivity with respect to dispersion is negligible at $d_v = 0.7$, this observation is not connected to dispersion and therefore serves as a solid indicator of the interaction rate parameter. Consequently, the effect of other processes which imprint on the BTC is no longer masked by dispersion at a d_v value above 0.7. As highly parameterized inverse modeling approaches usually suffer from non-unique solutions, the near complete removal of the effect of dispersion and the strong indication of rate limitation in the BTCs are a significant improvement in experimental design.

4.5.6 Equifinality of Dispersion and Kinetic Interaction

The effect of dispersion on the breakthrough is often the same as that of non-equilibrium in open-flow experiments (Wehrer and Totsche 2003). Therefore, it is plausible to assume that the BTC of closed-flow experiments shows a similar interdependency with respect to the observed concentration gradients. As presented in the previous sections, a dispersion-like “smearing” of concentration gradients is observable at Da numbers between 1 and 10. However, the sensitivity analysis on the effect of dispersion showed a major improvement in parameter uncertainty for a mixing vessel volume corresponding to a d_v value of 0.1. As a result, a better determination of dispersion seems also likely in these situations. To investigate which of these opposing effects is dominant, another sensitivity analysis on the correlation between the Da number and the $Pé$ number was made at this particular d_v value in closed-flow experiments in comparison to an analogous open-flow setup. As reference, artificial data was produced for Da numbers of 1, 10 and 100 at a $Pé$ number of 100 and $R = 2$, disturbed with white noise showing a relative standard deviation of 1%. In this range of parameters, the correlation between dispersion and kinetics is pronounced to the largest extent (Wehrer and Totsche 2003) and thus, the sensitivity analysis reflects the performance of both experimental designs under the most unfavorable conditions. For each artificial BTC, the objective function was calculated scanning all parameter combinations from a tenth to the tenfold of the optimal parameter. The resulting two-dimensional “surface” of the objective function directly reveals the sensitivity and the correlation of parameters.

At a Da number of 1, closed-flow (Figure 4.19 a,b) and open-flow (Figure 4.19 c) designs perform similarly with respect to parameter correlation seen as one unique minimum in the surface of the objective function. However, this minimum is much more pronounced in

case of closed-flow experiments. As a result, the confidence intervals for the Pe number are decreased by an order of magnitude like already observed for the sole sensitivity with respect to the Pe number (Table 4.9). The uncertainty for the determination of the Da number did not show a similar trend and both experimental modes perform equally well.

At a Da number of 10, a strong parameter correlation is seen for closed-flow mode as well as for open-flow mode (Figure 4.19 d,e,f), rendering the described equifinality inherent in solute transport observed under these conditions. However, closed-flow BTCs measured either in the effluent or the mixing vessel produce a much narrower range of plausible parameters due to the increase in sensitivity to the Pe number. As a consequence, also the Da number is much more confined in this correlation and the resulting confidence intervals are lower for both, the Pe number and the Da number (Table 4.9). This is even more pronounced for a Da number of 100, where a tenfold decrease in uncertainty (Table 4.9) is achieved for both parameters when comparing the closed-flow with the open-flow effluent BTC (Figure 4.19 g,i). In accordance to previous results, the parameter uncertainty lies somewhere in between when using the mixing vessel BTC in closed-flow mode (Figure 4.19 h). Higher Da numbers approach equilibrium interaction and a correlation is no longer observable for both experimental designs (Figure 4.19 j,k,l). To sum up, the decrease of uncertainty in the determination of dispersion achieved for closed-flow experiments run under optimal boundary conditions also impacts the correlation to non-equilibrium. In this way, a decrease of around 90% in parameter uncertainty is found in situations where the strongest correlation appears.

Table 4.9: Fitted Pe numbers and Da numbers with 0.95-confidence interval from noisy artificial data at $Da = 1$, $Da = 10$, $Da = 100$ and $Pe = 100$ in open-flow effluent (OF), closed-flow effluent (CF) and closed-flow mixing vessel (CF_m) mode at $d_v = 0.1$.

Da	1		10		100	
	fitted Pe	fitted Da	fitted Pe	fitted Da	fitted Pe	fitted Da
OF	100 ± 2	1.000 ± 0.004	98 ± 11	10.0 ± 0.2	106 ± 31	91 ± 44
CF	100.1 ± 0.3	1.001 ± 0.002	98 ± 2	10.05 ± 0.04	102 ± 3	96 ± 5
CF _m	100.5 ± 0.6	1.001 ± 0.004	100 ± 4	10.0 ± 0.1	99 ± 5	102 ± 10

Table 4.10: Fitted Pe numbers and Da numbers with 0.95-confidence interval from noisy artificial data at $Da = 1$, $Da = 10$, $Da = 100$ and $Pe = 100$ in open-flow effluent (OF), closed-flow effluent (CF) and closed-flow mixing vessel (CF_m) mode at $d_v = 0.7$.

Da	1		10		100	
	fitted Pe	fitted Da	fitted Pe	fitted Da	fitted Pe	fitted Da
OF	100 ± 2	0.999 ± 0.005	99 ± 11	10.0 ± 0.2	103 ± 26	94 ± 42
CF	100 ± 2	0.996 ± 0.004	97 ± 6	10.1 ± 6.0	103 ± 15	94 ± 24
CF _m	99 ± 20	1.004 ± 0.008	90 ± 40	10 ± 1	135 ± 1723	64 ± 762

The investigation of the correlation at a d_v value of 0.7 (Figure 4.20) reveals a massive decrease in sensitivity for all closed-flow BTC modi (Table 4.10). This is caused by the fast equilibration and thus, only small observable effect of dispersion. Especially seen with a Da number of 1 and measurements in the mixing vessel (Figure 4.20 b). For Da numbers greater unity, the objective function is very flat for mixing vessel BTCs (Figure 4.20 e,h,k), which renders the mixing vessel BTC uninformative with respect to dispersion and kinetics. This is also imprinted on the very large confidence intervals found in the inverse determination of parameters (Table 4.10).

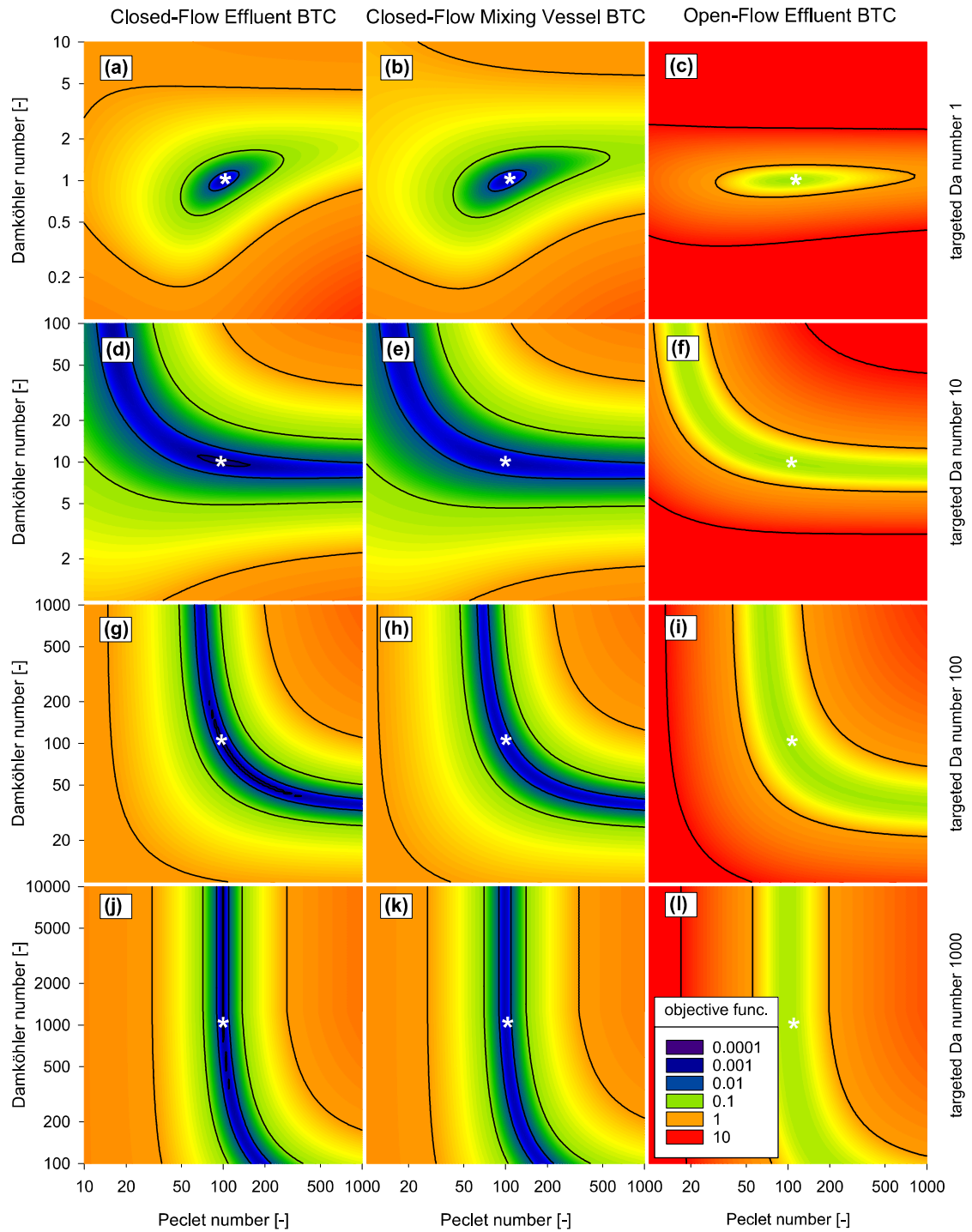


Figure 4.19: Surface of the objective function with respect to changes in the Da number and the $Pé$ number around the optimal value of $Pé = 100$ at $d_v = 0.1$. Each column represents a different mode of measurement (from left to right: closed-flow effluent, closed-flow mixing vessel, open-flow effluent). Each row represents a different optimal Da number (from top to bottom: $Da = 1$, $Da = 10$, $Da = 100$, $Da = 1000$).

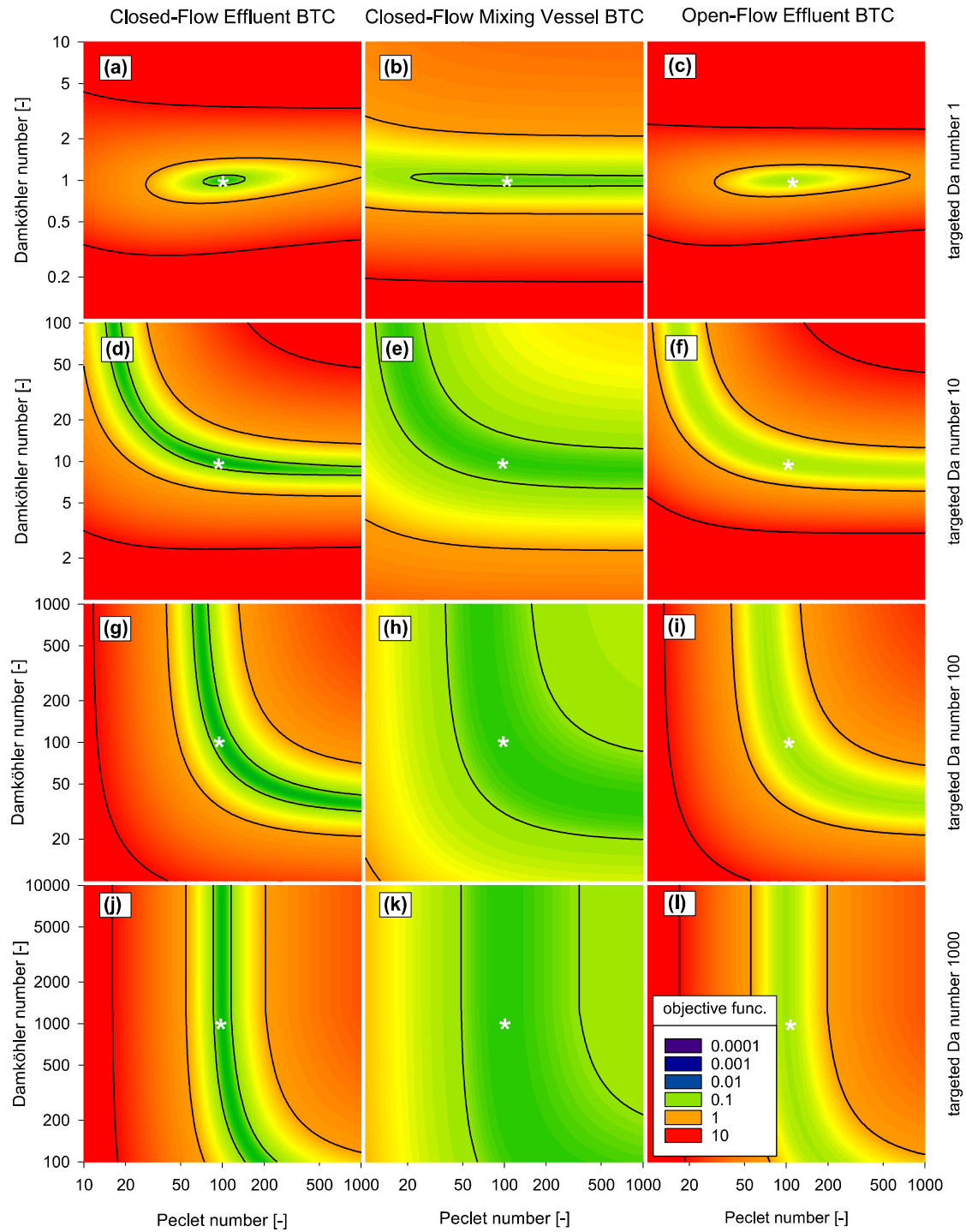


Figure 4.20: Surface of the objective function with respect to changes in the Da number and the $Pé$ number around the optimal value of $Pé = 100$ at $d_v = 0.7$. Each column represents a different mode of measurement (from left to right: closed-flow effluent, closed-flow mixing vessel, open-flow effluent). Each row represents a different optimal Da number (from top to bottom: $Da = 1$, $Da = 10$, $Da = 100$, $Da = 1000$).

4.6 Comparison to a Damped Harmonic Oscillator

4.6.1 Application to Experimental Results

An experiment was carried out to investigate if the presented model of a harmonic oscillator can be applied to closed-flow experiments. To suppress any liquid solid interactions as well as microbial interference, the substrate Qz was used in combination with the NaCl tracer. Details on the experimental setup as well as transport parameters are found in Table 4.11. The BTC was measured via electrical conductivity probes in the column effluent for comparability to BTCs obtained in classical column experiments. The numerical model solving the ADE was used to reconstruct the BTC by fitting the dispersion coefficient. All other model parameters were determined from the column geometry and gravimetric measurements during saturation and flow periods.

The measured BTC shows the typical oscillatory behavior of closed-flow experiments. The model describing damped harmonic oscillators applied to column experiments in Equation (2.88) was fitted to the BTC by using the Levenberg-Marquardt algorithm and was successful in reconstructing the overall shape of the oscillations (Figure 4.21 and Table 4.12). The oscillatory sinusoidal elementary function of the harmonic oscillator covers the BTC features connected to the closed loop, i.e. the wavelength, nearly perfectly (Figure 4.21). In addition, the damping observed in the decreased oscillation height is perfectly represented by the exponential damping described by the harmonic oscillator (Figure 4.21). However, the initial time from $t_{pv} = 0$ to the onset of the breakthrough, where the BTC is zero, could not be covered, since the harmonic oscillator always increases its amplitude in direction opposite to the damping causing an overshoot into negative or higher than 100% concentrations. A closer look at the first oscillation maximum reveals an asymmetry in the measured BTC that also can not be covered by the purely sinusoidal harmonic oscillator. Thus, the experimental data gives a mixed impression on the applicability of the model describing harmonic oscillators.

4.6.2 Application to Numerical Results

To systematically test the performance of the harmonic oscillator model, a series of BTC at the effluent of a closed-flow setup was simulated at a constant $Pé$ number of 100 covering

Table 4.11: Experimental boundary conditions used for measurement of the effluent BTC. The interval represents the 0.95 confidence interval from parameters fitting.

L [cm]	θ [-]	ρ [g cm ⁻³]	Q [$\mu\text{L min}^{-1}$]	D [cm ² h ⁻¹]	V_{mix} [mL]	d_v [-]
15	0.385	1.56	216	0.502 ± 0.003	20	0.216

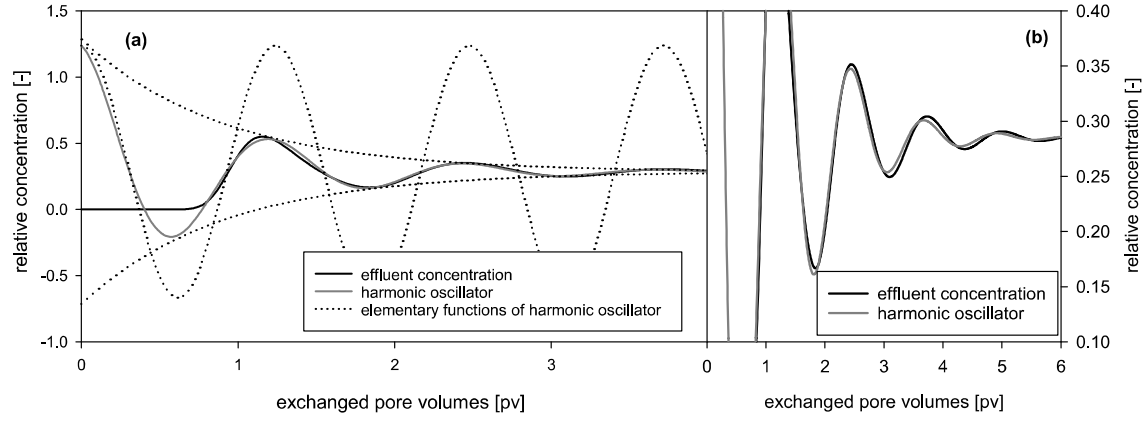


Figure 4.21: Reconstruction of the effluent BTC of a typical closed-flow experiment using the concept of a harmonic oscillator, the elementary functions causing the oscillation and the damping are shown separately.

d_v values from 0.01 to 0.6. For each d_v , the model for harmonic oscillators was fitted to the simulated BTC ($d_v = 0.1$, $d_v = 0.3$ and $d_v = 0.6$ are shown in Figure 4.22 a). An overview of resulting parameters is given in Table 4.13. With increasing d_v , all parameters besides the phase Φ show a systematic trend. The angular frequency ω_0 is slightly decreasing, the damping and the initial amplitude both are increasing strongly. As only the mixing vessel volume and thus, the damping caused by the mixing process was changed in the simulations, no direct correspondence of parameters from the harmonic oscillator model becomes evident. Rather, the mixing process is reflected in the combination of all parameters. Furthermore, the assumption of the angular frequency ω_0 as an indication of the transport velocity is only meaningful for small d_v , where a value near the optimum of 2π is obtained. This implies that with increasing mixing vessel volume, the passage of the center of mass through the mixing vessel needs more time, even with constant stirring, and a fundamental wavelength that is only dependent on the transport velocity is not found in closed-flow experiments.

To investigate the influence of dispersion on the parameters of the harmonic oscillator, a series of BTC at the effluent of a closed-flow experiment was simulated using a d_v of 0.1 and $Pé$ number from 1 to 1000. For each $Pé$ number, the model for harmonic oscillators was fitted to the simulated BTC (for $Pé = 30$ and $Pé = 1000$ shown in Figure 4.22 b). Comparable to the result from the previous simulation series, all parameters of the

Table 4.12: Parameters used for reconstruction of BTC data with the analytical solution of a harmonic oscillator.

ω_0 [-]	ζ [-]	Γ [-]	Φ [-]	R^2
5.190	0.214	0.953	1.587	0.98

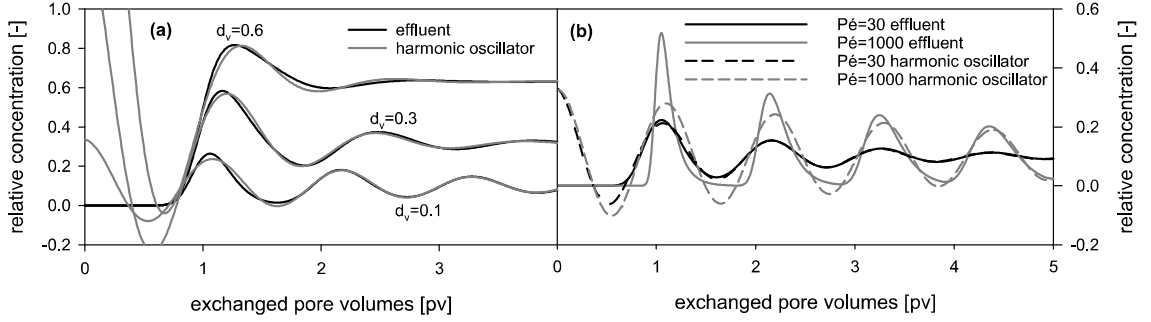


Figure 4.22: Reconstruction of the effluent BTC of simulated closed-flow experiments using the concept of a harmonic oscillator, left: $d_v = 0.1$, $d_v = 0.3$ and $d_v = 0.6$, right: $Pé = 30$ and $Pé = 1000$.

harmonic oscillator changed with varying $Pé$ number (Table 4.13). As expected, the damping decreases with increasing $Pé$ number, but also the angular frequency and the initial amplitude show a strong response. Therefore, also the damping caused by dispersion and diffusion is not solely covered by ζ . Interestingly, the model of harmonic oscillators was able to perfectly match the simulated BTC up to a $Pé$ number of 30 (Figure 4.22 b) as seen in the R^2 near unity. For increasing $Pé$ number, i.e. for advection dominated systems, the fit gets worse dramatically (e.g at $Pé = 1000$ in Figure 4.22 b). Hence, diffusion dominated systems behave more similar to a harmonic oscillator.

Table 4.13: Parameters used for reconstruction of numerical BTC data at different d_v and different $Pé$ numbers with the analytical solution of a harmonic oscillator.

	$d_v (Pé = 100)$						$Pé (d_v = 0.1)$						
	0.01	0.03	0.06	0.1	0.3	0.6	1	3	10	30	100	300	1000
ω_0 [-]	6.26	6.13	5.95	5.76	5.14	5.22	11.79	8.12	6.12	5.80	5.76	5.73	5.73
ζ [-]	0.066	0.067	0.073	0.087	0.241	0.383	0.919	0.754	0.438	0.188	0.087	0.049	0.036
Γ [-]	0.022	0.071	0.143	0.236	1.157	2.806	0.523	0.425	0.258	0.224	0.236	0.229	0.226
Φ [-]	1.60	1.57	1.56	1.56	1.61	1.06	3.21	2.85	2.41	1.82	1.56	1.53	1.52
R^2 [-]	0.95	0.95	0.95	0.96	0.98	1.00	1.00	1.00	1.00	0.99	0.96	0.87	0.77

4.7 Transfer Functions

The concept of transfer functions was applied to a series of simulated closed-flow BTCs with d_v ranging from 0.01 to 1 at a Pe number of 100. Specifically, the mixing vessel BTC was convolved with the travel-time PDF as stated in Equation (2.100) using exactly the parameters used in the simulation. In this way, the simulated effluent BTC was perfectly matched in all cases. As expected, the general concept of transfer function is still valid for closed-flow experiments. However, both the input signal represented by the influent concentration or the mixing vessel BTC and the response signal represented by the effluent BTC are experimental outcomes in closed-flow experiments, unlike in open-flow experiments, where the input signal is solely given by the experimenter. An identification of the parameters in the travel-time PDF would therefore require the measurement of the effluent BTC as well as the mixing vessel BTC. This represents an unhandy complication of the approach and the closed-flow experiment renders rather unsuited for the identification of the travel-time PDF.

The desired result would be achieved by finding a transfer function model that uses an input signal that is actually provided by the experimenter, i.e. the mixing vessel volume and its initial chemical composition. However, the convolution integral as stated in Equation (2.101) explicitly uses the development of influent concentration, which is not known a priori in closed-flow mode. In this sense, the general concept of transfer functions is not applicable in a beneficial way to closed-flow experiments

As shown in the previous section, the model of harmonic oscillators is not applicable as function to convert the experimental boundary condition to the expected experimental outcome in effluent or mixing vessel. However, a more thorough analysis of the circular coupling of the PDE describing transport given in Equation (2.25) and the mixing in the mixing vessel given in Equation (2.66) might reveal an appropriate approach.

4.8 Fourier Transform

To investigate the information potential of the Fourier transform, BTCs were modeled in the mixing vessel and the effluent at a $Pé$ number of 100 and d_v values of 0.7, 0.3 and 0.1 to cover experimental conditions with hardly any oscillation, medium oscillations and strong oscillations. In addition, BTCs were simulated at a d_v of 0.3 with a retardation of 1.5 and 2 to illustrate the effect of sorption on the wavelength of the oscillation. Of each BTC, the discrete Fourier transform was calculated according to Equation (2.124).

At a d_v value of 0.7, the Fourier transform of the mixing vessel BTC (Figure 4.23 a) shows a smooth distribution of different frequencies in the signal without a distinct peak indicating no dominant periodic signal in the BTC (Figure 4.23 b). This conclusion fully complies with the simulated BTC. In comparison, the effluent BTC shows a slight oscillation causing a broad peak of the discrete Fourier transform at low frequencies. Interestingly, a second peak emerges at around 1.4 pv^{-1} . This frequency is about twice the frequency supposedly caused by the mean transport velocity. The exact wavelength is depending on the mixing vessel volume and is consequently always longer than 1 pv. In case of $d_v = 0.7$, the slight oscillation shows an approximated wavelength of 1.4 pv, which results in the mentioned basic frequency of about 0.7 pv^{-1} . Consequently, the BTC deviates from a sinusoidal shape especially in the ascending and descending part of the oscillation, i.e. twice per main oscillation.

At $d_v = 0.3$, the oscillation is much more pronounced in both BTCs (Figure 4.23 c). In the Fourier transform, this results in a distinct peak at around 0.7 pv^{-1} (Figure 4.23 d). However, both BTCs produce a different peak position in the Fourier transform and therefore oscillate at a different frequency despite the same experimental conditions. This renders the oscillation frequency or wavelength only a vague indication of the mean transport velocity. This is in accordance to the different angular frequencies obtained for different d_v values in the reconstruction of the harmonic oscillator. Once again, a second peak is seen at double frequency.

At $d_v = 0.1$, the wavelength of both oscillations approach each other (Figure 4.23 e) resulting in a distinct peak in the Fourier transform at 0.9 pv^{-1} . Especially the Fourier transform of the mixing vessel BTC contains a continuum of higher frequency parts due to the initial decrease in the mixing vessel that is purely exponential. This conclusion is confirmed by the lack of higher frequencies in the Fourier transform of the effluent BTC.

Unsurprisingly, the main peak of the Fourier transform is shifted to lower frequencies in case of retarded transport (Figure 4.23 g-j). However, the general shape of the Fourier transform is unaffected and a retardation acts like a scaling of the frequency.

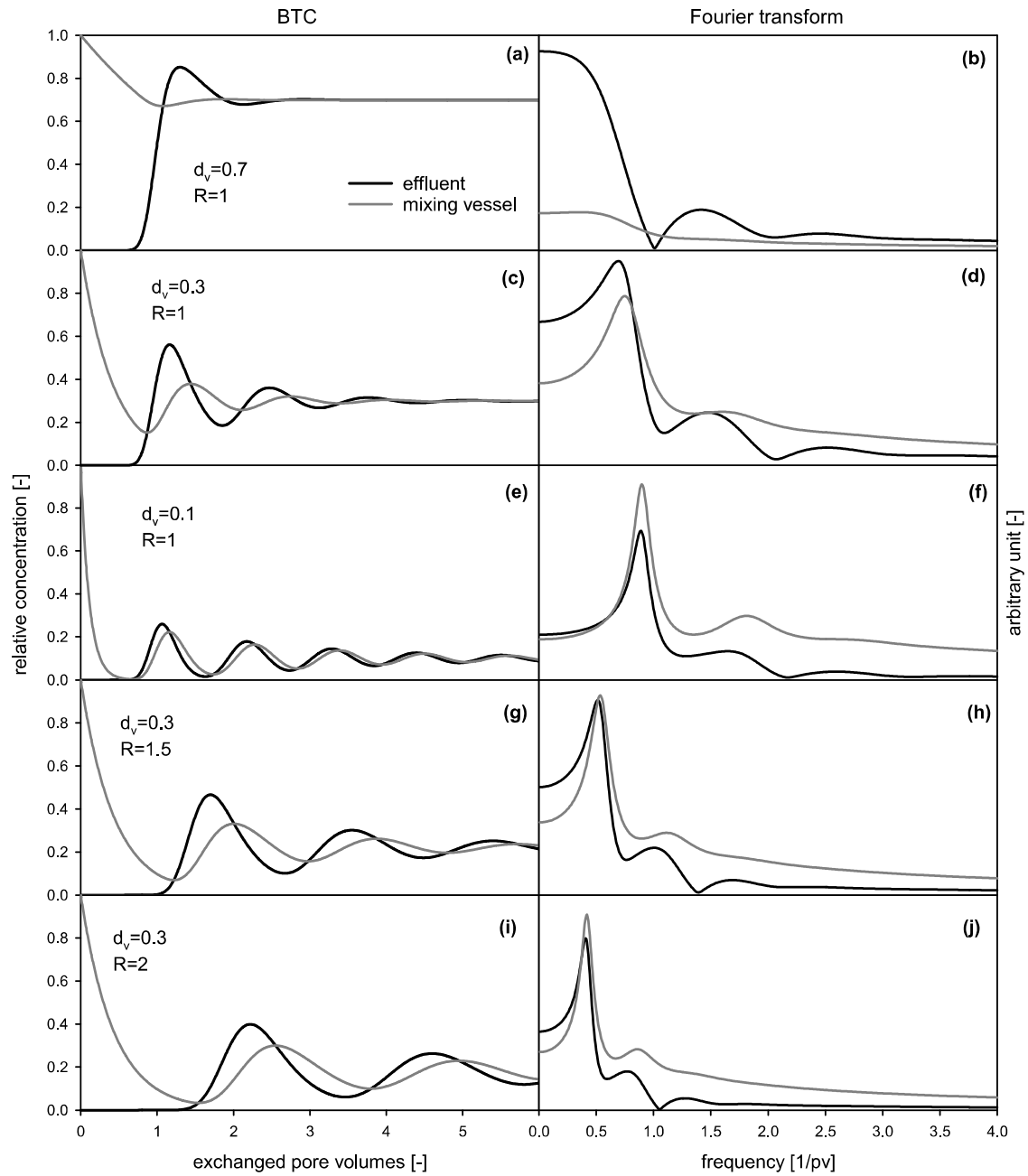


Figure 4.23: Fourier transform (right column) of BTCs (left column) at $d_v = 0.7$ (first row), $d_v = 0.3$ (second, fourth and fifth row) and $d_v = 0.1$ (third row), comparing conservative (first, second and third row) with reactive transport at $R = 1.5$ (fourth row) and $R = 2$ (fifth row).

5 Final Assessment of Hypotheses

Throughout this thesis, several hypothesis were built on theoretical considerations about specific boundary conditions and features of closed-flow experiments. With the presented experimental and numerical results, these hypotheses can be conclusively analyzed and accepted or rejected, simultaneously providing a focused summary of the results.

5.1 Minor Hypotheses

5.1.1 Hypotheses Emerging from the Mass Balance

1. The volumetric dilution factor describes the additional experimental condition needed to sufficiently describe closed-flow experiments and therefore serves as a feasible reference parameter to compare experimental setups.

As frequently shown in the experimental and numerical data, the boundary condition that is needed to describe the characteristics of a closed-flow experiment is the mixing vessel solute volume. Specifically, the relation of mixing vessel volume to the total volume decides on the appearance of concentration oscillations. Two closed-flow column experiments sharing this ratio show the same amount of oscillations. This ratio, throughout the thesis referred to as volumetric dilution factor, is therefore the most feasible dimensionless parameter that fully describes the closed-flow experimental setup. However, it is an additional parameter and the complete set of dimensionless parameters used to describe the characteristics of the column setup as known for open-flow experiments is needed as well.

To conclude, the hypothesis can be accepted.

2. The intrinsic determination of the water content from BTC data in closed-flow experiments is unique, robust and practicable.

The experimentally obtained BTCs showed a convergence to a stable equilibrium in case of conservative tracers. The relation of the equilibrium concentration in combination with the initial concentration, the column geometry and the mixing vessel volume was then used to reconstruct the water content that would explain the observed dilution. The results were in accordance to gravimetrically determined values and the procedure was applied repeatedly to the same column, each time giving a slightly different result.

This highlights the strength of the proposed method to also determine the water content within successive experiments in the same column. In open-flow mode, the reconstruction of the water content from the tracer travel time is strongly correlated to the pumping rate. In closed-flow mode, neither the pumping rate nor other transport process imprints on the equilibrium for conservative tracers and this observation can be attributed to the water content of the porous medium uniquely.

The hypothesis is therefore accepted in every detail.

3. The intrinsic determination of sorbed mass from BTC data in closed-flow experiments is unique, robust and practicable.

As shown in the numerical section, the newly introduced parameter S calculated according to Equation (2.60) represents an easy way to obtain the mass of a tracer sorbed to the porous medium from the observation of the equilibrium concentration established after the oscillations have diminished. Provided the water content of the porous medium, which is implicitly needed in Equation (2.60) as d_v , is known, this observation and the evaluation of sorbed mass is also unique and robust. However, if the interactions is kinetically limited as experimentally shown for the reaction of vanillic acid with a porous medium containing goethite, the equilibrium may not be established within the timeframe of the experiment and thus, the calculation of S is impeded or at least is strictly related to the sorbed mass at the particular point in time the “equilibrium” concentration is measured.

The hypothesis can therefore be accepted in case of interactions, which converge to an equilibrium in the timeframe of the experiment.

5.1.2 Hypotheses Emerging from the Mixing Process

1. Equation (2.66) fully describes the temporal course of concentration in the mixing vessel and therefore can serve as model for the inflow boundary condition.

The application of model simulations to the experimental data was very successful for all conservative tracer BTCs. The distinct change of the BTC observed for different mixing vessel volumes could be addressed completely by the consideration of Equation (2.66) as inflow boundary condition. The agreement of experimental data with solutions for Equation (2.66) for special boundary conditions also shows the validity of the assumptions made in the derivation of Equation (2.66). To conclude, Equation (2.66) is derived in a physically meaningful way and sufficiently describes the dynamic influent in closed-flow experiments.

Thus, the hypothesis is fully accepted.

2. *The solute volume of the mixing vessel decisively impacts the shape of the BTC, the establishment of equilibrium and the type of inflow boundary condition.*

Experimental as well as numerical data has shown that the mixing vessel volume, or, more precisely, the relation of mixing vessel volume to the total volume of the setup, decides on the appearance of concentration oscillations in the BTC. Large mixing vessel volumes suppress oscillations, whereas small mixing vessel volumes show a pronounced oscillation. Numerical reconstructions of the spatial solute profile inside the column revealed that large mixing vessel volumes provide a distribution comparable to those obtained in open-flow when applying a continuous-feed boundary condition, whereas a more and more pulse-like distribution is created with decreasing mixing vessel volume. Lastly, the equilibrium concentration is strongly influenced by the ratio of involved volumes and the resulting dilution.

Therefore, all claims made in this hypothesis can be accepted.

3. *The approximation of Equation (2.66) presented in order to derive the volumetric pumping rate Q is applicable.*

Several conservative experiments with different mixing vessel volumes and different pumping rates were analyzed with respect to the initial breakthrough behavior. The model resulting from the equation describing the mixing vessel perfectly resembles this shape permitting the reconstruction of the pumping rate. All results were in accordance to gravimetrically determined values and calculations from subsequent experiments showed a constant slight variation in the pumping rate, which indicates wear of tubing. As the BTC behaves exponentially in the observed range, the effluent solution is free of tracer and no other process interferes. The approximation of Equation (2.66) is therefore valid and the observation can be attributed to the pumping rate uniquely.

As a result, the hypothesis is accepted.

4. *The approximation of Equation (2.66) presented in order to derive the retardation R is applicable despite the neglect of dispersion.*

The BCM and thus, the retardation, was reconstructed by applying Equation (2.80) to experimental and numerical data. The observation of the first oscillation maximum has been used as a solid indication of the mean transport velocity. However, a shift in the oscillation maximum was observed, which could successfully be represented by the proposed derivation and the reconstructed retardations are similar to the expected values independent of the mixing vessel volume. Still, a systematic deviation towards higher values is pointing to the insufficient consideration of dispersion and diffusion.

To sum up, the proposed method gives a slightly biased, but solid estimation of the BCM and the hypothesis can be accepted.

5. *The BTC obtained from measurements in the mixing vessel contains the same information as the BTC measured in the effluent.*

The validity of the equation describing the course of concentration in the mixing vessel also proves that a BTC measured in the mixing vessel shares all information present in the effluent, since the effluent BTC can easily be calculated from the mixing vessel BTC. Furthermore, the mixing vessel BTC indicates the pumping rate in the initial part of the breakthrough, which is not observable in the effluent BTC.

The hypothesis is therefore verified and can be stated even stronger towards a higher information content in the mixing vessel BTC.

5.1.3 Hypotheses Emerging from the Harmonic Oscillator

1. *The model describing harmonic oscillators is applicable and allows the interpretation of experimental results in terms of the model.*

The promising similarity between closed-flow experiments and harmonic oscillators has been used to reconstruct measured and simulated BTC of closed-flow experiments with the model describing harmonic oscillators to a more or less satisfying degree. The most obvious aspect that closed-flow experiments and damped harmonic oscillators have in common, is the concept of a system that is out of equilibrium and relaxes in order to reach a stable state. However, the reason for a harmonic oscillator to overshoot is the inertia of a mass, and the proposed analogy to the transport inside a column is rather vague and does not allow for a strict projection of the physics behind inertia. For this reason, a perfect compliance of the model describing harmonic oscillators and the observed BTC in closed-flow experiments is neither observed in the presented experiment nor expected. Nonetheless, the main characteristics, i.e. the damping, the wavelength and the oscillation, which is sinusoidal in the measured BTC from $t_{pv} = 2$, are generally represented by the model of a harmonic oscillator. However, the analysis of relation between parameters of solute transport and harmonic oscillators provided no useful result rendering the comparison of these models a conceptual issue and the similarities in the graph a mere coincidence. To conclude, both systems can be compared conceptually and phenomenologically, but the mathematical description of harmonic oscillator is not applicable for closed-flow experiments as is.

As a consequence, the hypothesis has to be rejected, since no mechanistic relationship is evident.

2. *The damping of the harmonic oscillator is strongly related to the mixing in the mixing vessel and the dispersion.*

The numerical simulations have clearly shown that the damping parameter strongly correlates with the volume of the mixing vessel and the extent of dispersion/diffusion.

However, no functional connection is evident and no conclusion can be drawn from fitted damping parameters regarding transport parameters.

The hypothesis is therefore valid as stated, but no benefit from the determination of the damping parameter is obvious.

3. *There is a fundamental wavelength corresponding to the undamped angular frequency ω_0 that is solely dependent on the transport velocity and the differences in observed wavelength are a result of damping, which causes an effective damped angular frequency ω_d .*

As shown in subsection 4.6.2, the undamped angular frequency also varies with respect to mixing vessel volume and *Pé* number.

Consequently, the concept of a reduced damped frequency in harmonic oscillators is not able to explain the differences in the observed wavelength and this hypothesis has to be rejected.

5.1.4 Hypotheses Emerging from the BTC analysis

1. *The convolution of the travel-time PDF and input signal is still a valid representation of the processes in a closed-flow experiment.*

Based on a numerical investigation, the convolution of the input signal, i.e. the course of concentration in the mixing vessel, with the travel-time PDF always reproduced the effluent BTC. In that sense, the hypothesis can be considered valid. However, as the input signal is not known a priori as it is in open-flow experiments, this methodology is not able to predict the effluent BTC of a closed-flow experiment without measuring part of the outcome, i.e. the mixing vessel BTC. A function that is able to convert the actual input information, which is the mixing vessel volume and solute composition, would therefore be the ideal result. To the knowledge of the author, such a function is unavailable.

Thus, the hypothesis is accepted, but the application of transfer functions to closed-flow experiments is complicated for practical reasons as no clear distinction of input signal and response signal is possible.

2. *The Fourier transform of the BTC provides additional insights into the periodic behavior of closed-flow experiments.*

The simulated BTCs generally produced a main peak in the Fourier transform corresponding to the basic wavelength. Although the peak was correlated to the mean transport velocity, its exact position was influenced by the mixing vessel volume and the mode of acquisition of the BTC. In accordance to the results from the harmonic oscillator approach, the wavelength or frequency of the oscillation is apparently only a vague indication of the mean transport velocity and the retardation. No obvious

information gain is provided by the Fourier transform. The occurrence of harmonic overtones additionally underlines the difference of the oscillations in closed-flow experiments from pure sinusoidal waves. However, the similarity of closed-flow BTCs and waves suggests further informative potential that is still unrevealed.

This hypothesis is not conclusively examined and therefore an answer is left open.

5.2 Main Hypotheses

1. *Transport parameters are reflected in distinct closed-flow BTC features and can be extracted from measurements uniquely.*

The emerging features of the BTCs obtained in closed-flow mode correlate to distinct transport parameters with varying degree of sensitivity (Table 5.1). Some features are strongly indicative of the corresponding properties and parameters and permit their robust determination, while other features only allow for a qualitative assessment. Each feature was investigated experimentally and numerically throughout the thesis leading to the conclusion that the total information content of closed-flow BTCs is higher in comparison to those obtained in open-flow mode.

As a result, the hypothesis is accepted with the restriction that not all BTC features allow a solid, unique reconstruction.

2. *The appearance of concentration oscillations and thus, the sensitivity of the BTC to transport parameters that imprint on the oscillations is dependent on the mixing vessel and can therefore be controlled by the experimenter.*

As shown in the experimental results, the appearance of concentration oscillations can be controlled by adjusting d_v by selecting a corresponding mixing vessel volume. In this way, all transport processes that imprint on the oscillation can either be pronounced or suppressed. If the aim of the experiment is the determination of the water content, the equilibrium concentration, which is the desired observation, should be reached as fast as possible and oscillations would interfere. To achieve this, d_v should be set greater than 0.5 by choosing a sufficiently large mixing vessel volume. The same argument holds for the investigation of rate-limited interactions, which imprint on the BTC similarly to dispersion and therefore benefit from the suppression of the effect of dispersion at higher mixing vessel volumes. On the other hand, if the damping of the oscillations is used as an indication of dispersion, an oscillation of several pore volumes is preferable, which can be achieved by using a small mixing vessel volume. Theoretical considerations and

Table 5.1: Overview of BTC features and related transport processes.

BTC feature	process/property	sensitivity
initial exponential decrease	pumping rate	very high
oscillation wavelength	mean transport velocity, retardation	medium
oscillation damping	dispersion, diffusion, non-equilibrium	high
oscillation asymmetry	nonlinearity of interaction	medium
equilibrium concentration	water content, sorbed mass	very high

the numerical results provide the evidence, that the sensitivity of the BTC to these particular transport parameters is strongly dependent on the extent of oscillations. The proposed hypothesis is therefore accepted in every detail.

3. Transport parameters can be determined with higher sensitivity as compared to classical approaches.

An exhaustive numerical investigation was conducted to cover the sensitivity of BTCs obtained in closed-flow to selected transport parameters. Special focus was put on the effect of dispersion, which is one of the main parameters frequently determined with column experiments. A strong influence of dispersion on the damping of the oscillations was observed. As a result, closed-flow experiments forcing strong and enduring oscillations behave very sensitive with respect to dispersion. In the most optimal case, a decrease in uncertainty of one order of magnitude is achieved in comparison to open-flow experiments. This dramatic decrease is caused by the robustness of the inversion of experimental result of closed-flow experiments regarding noisy data. In closed-flow mode, dispersion imprints on the BTC over several pore volumes and therefore the inversion is not as susceptible to noise as it is in case of open-flow data. From another point of view, a closed-flow experiment can be considered an easy way of conducting consecutive breakthrough experiments since each travel of a solute pulse through the column produces information on dispersion. For that reason, a closed-flow experiment with pronounced oscillations shows a smaller uncertainty in parameter determination than an open-flow experiment. Another benefit regarding dispersion is the ability of the experimenter to actually decide on the sensitivity of the resulting BTC as he can decide on the appearance of oscillations by providing the desired mixing vessel volume. Furthermore, it could be shown conclusively that the decrease in uncertainty also reduces the equifinality between dispersion and rate-limited interaction, which produces a dispersion-like effect and therefore correlates with dispersion for a wide range of Da numbers. In correlated scenarios, a low d_v is mandatory to produce pronounced oscillations. Regarding retardation, a comparable situation is found and the uncertainty with respect to the retardation coefficient is decreased by the same degree.

The hypothesis is therefore accepted concerning dispersion, retardation and the interaction rate.

4. The kinetics of interactions can be studied directly under conditions of transport in a porous medium.

The closed-flow experiment with vanillic acid interacting with the porous medium containing goethite showed an oscillation that was superposed with a trend similar to an exponential decrease, which points to a first-order kinetic. Consequently, a

reconstruction of the observed BTC with the two-region model was very successful. A set of numerical simulations at Da numbers in the range of the observed Da showed that under conditions suppressing the appearance of oscillations, BTCs in the mixing vessel exactly behave like what is to be expected from the course of concentration in a completely mixed batch reactor experiment. This proves the assumption that closed-flow experiments can be considered equilibration experiments under transport conditions comparable to natural soils.

The hypothesis is therefore accepted.

6 Outlook and Implications

In closed-flow mode, the effluent BTC can be determined from the BTC in the mixing vessel if both the pumping rate and the mixing vessel volume can be regarded as constant. For this reason, both BTCs are equivalent with respect to the information “contained” in the breakthrough behavior. This implies that, compared to an open-flow approach, where the effluent concentration is measured, it is sufficient to record the BTC in the mixing vessel when a closed-flow setup is used. This avoids void volume in flow-through cells, which would be necessary to directly record the effluent concentration without using a fraction collector that necessarily only provides the integral information over a fixed time span. Concerning the apparent dispersion that is caused by void volumes, this is a beneficial simplification of the experimental design. Furthermore, the determination of the flow rate is not possible when only the effluent concentration is measured since the initial dilution, which is required for the evaluation of the flow rate, cannot be observed this way in closed-flow experiments. Thus, it is convenient to record the mixing vessel BTC in closed-flow experiments.

As the column effluent is collected by the mixing vessel, the total fluid volume, i.e. the sum of the fluid stored in the porous medium, the tubing and the mixing vessel, is constant at any moment of the experiment. To maintain the possibility of evaluating mass balances in closed-flow experiments, any measurements are therefore restricted to consume no or only small amounts. For ionic solutes (conservative tracers like Cl^- or Br^-), this can be achieved by using electrical conductivity probes. Spectroscopic methods (e.g. detection of UV/Vis absorption or fluorescence) can also be applied, e.g. for the detection of aromatic compounds as presented for the quantification of vanillic acid. In addition, the closed loop might be useful when working under sterile conditions.

As suggested by the reactive tracer breakthrough, the convergence of solute concentration to equilibrium or even zero might further allow for the study of slow release or transformation processes of the porous medium and slow chemical or physical processes as the repeated breakthrough of the solute through the column simulates longer residence time or a longer effective soil profile, respectively. In addition, the recirculation also inherently maintains feedbacks of interaction between the liquid and the solid phase under transport conditions found in natural soils and therefore less artifacts from the artificial chemical composition of the influent solution are expected in future experiments.

6.1 Application to Unsaturated Experiments

The results presented in this work were obtained exclusively from saturated experiments. Nonetheless, some extrapolation to the unsaturated case is allowed. There, the recirculation of effluent solution into the solution supply vessel would obviously also result in the conservation of the total solute volume. Consequently, all substances in solution are also conserved. However, the assumption of a constant mixing vessel volume is no longer valid as any change in saturation of the porous medium would directly result in a change of mixing vessel solute volume. This implies that a changing saturation can be tracked indirectly via the mixing vessel. The method that was derived in order to determine the water content of the porous medium by dilution of a conservative tracer is also applicable, but only represents the water content that is present at time of application of the tracer solution. The initial exponential decrease used for the reconstruction of the pumping rate is expected to also indicate the outflow rate, which usually differs from the pumping rate that is applied for the irrigation. By application of a small mixing vessel solute volume, also the appearance of concentration oscillations in the effluent and the mixing vessel is likely and a similar sensitivity of the BTC with respect to transport parameters is suggested from the results found in the saturated case.

To adapt the presented equations in order to be applicable for the unsaturated case, the mass balances presented in the theoretical section have to be reconsidered as the constant mixing vessel volume was a basic assumption in the saturated case.

In general, all advantages and limitations of the closed-flow approach that apply to the saturated case apply to unsaturated experiments as well and no aspect presented within this thesis implies that an experimenter should avoid a closed-flow approach in the unsaturated case. Quite the contrary, the information retrieval from BTC data is likely to be increased by the same degree as described for saturated experiments.

7 Conclusions

Column experiments run in closed-flow mode have shown to be an alternative to other approaches when studying solute transport in soils. The BTC shows specific characteristics with observable features, i.e. the initial exponential decrease, oscillation frequency, amplitude and damping as well as the equilibrium state. Each feature has a specific sensitivity to the transport parameters of the porous medium and allows for the reconstruction of transport parameters as known for classical column experiments. Under optimal boundary conditions, a decrease in uncertainty of fitted parameters by an order of magnitude can be achieved. The closed-flow design therefore renders highly sensitive.

The equilibrium reached after the oscillations have faded, allow for an interpretation of the mass balance in the closed system, which is the main feature besides the oscillation that this experimental design provides. This equilibrium can be used for the determination of the actual soil water content, but also allows for a consideration of further sinks, e.g. sorption and decay. The application is useful in particular, when gravimetric methods for the determination of the water content are prohibited for the named reasons. In closed-flow mode, virtually no preconditioning of the soils is necessary and undisturbed soil cores can be used as is. The closed-flow design therefore renders uncomplicated.

The appearance of concentration oscillations in effluent and mixing vessel can be controlled by the mixing vessel volume and therefore all processes that imprint in specific oscillation features can either be pronounced or suppressed. The usage of mixing vessel volumes much larger than the water-filled pore space of the porous medium results in a quick convergence to equilibrium and thus, the absence of oscillations. On the other hand, if a mixing vessel solute volume resulting in a d_v value of 0.1 is chosen, strong oscillation are provoked over several pore volumes. The closed-flow design therefore renders flexible.

Experiments with artificial soil have shown that one single conservative tracer experiment can be used to intrinsically determine the exact pumping rate and the water content from BTC data without numerical modeling. This extensive information retrieval reduces the experimental effort and provides control over decisive boundary conditions without loss of accuracy. The closed-flow design therefore renders informative.

As shown with the exponential decrease of the reactive tracer in the long term equilibration phase, the convergence of solute concentration to equilibrium also allows for the study of non-equilibrium. In agreement to model simulations, a general trend superimposes on the whole BTC and the mixing vessel solute concentration still decreases after the

oscillations have diminished. In addition, the recirculation allows for the investigation of feedbacks in the interaction between the liquid and the solid phase as seen in the change in pH value under transport conditions found in natural soils. In general, all responses of the porous medium to the application of a tracer solution can easily be observed since they are conserved in the closed loop. The closed-flow design therefore renders multifunctional.

Based on the presented characteristics, the closed-flow design can be considered an experimental design to study transport in porous media due the close relation to classical column experiments as well as an equilibration experiment due to the boundary condition comparable to a completely mixed batch reactor experiment. An overview of optimal experimental conditions for the investigation of specific transport processes is given in Table 7.1. The closed-flow design therefore renders innovative.

A numerical simulation of closed-flow experiments demands a mathematical description of the dynamics observed in the mixing vessel. By a consideration of mass balances under the assumption of ideal mixing, the governing equation that describes the temporal evolution of concentration in the mixing vessel could be derived. By discretization of this statement, it was possible to establish a connection to the numerical solution of the ADE. With this simple model, an excellent agreement between model and observation was possible. Therefore, it can be concluded that all processes that have to be considered in addition to classical approaches are covered by the model. In addition, the model implementation does not interfere with the solution of the ADE and thus, theoretically applies to all possible formulations and extensions of the ADE. The closed-flow design therefore renders easily accessible by physical and mathematical descriptions.

For many classical applications of column experiments, e.g. the quantification of retardation or the dispersion, the classical open-flow column outflow experiment is a well-established and reliable tool. However, the application of closed-flow mode experiments is very beneficial when feedbacks of liquid solid interactions are investigated and if gathered data is noisy or correlation between parameters interferes with their unique identification. As this situation frequently applies to studies with natural porous media, the drawn conclusions are of high practical relevance.

Table 7.1: Overview of suggested experimental boundary conditions to obtain an indicative closed-flow BTC.

research focus	desired observation	d_v [-]	Q [pv d ⁻¹]
dispersion/diffusion	strong oscillation with distinct damping	0.1 to 0.3	1 to 6
equilibrium sorption	wavelength, stable equilibrium	0.1 to 0.3	1 to 6
nonlinearity	strong oscillation with asymmetry	0.1 to 0.3	1 to 6
water content	no oscillation, stable equilibrium	≥ 0.7	fast
kinetics	establishment of equilibrium	≥ 0.7	slow, fast

References

- Ali, M. A., and D. A. Dzombak. 1996. Competitive sorption of simple organic acids and sulfate on goethite. *Environ. Sci. Technol.* 30 (4): 1061–1071.
- Allaire, G., and A. Craig. 2007. *Numerical analysis and optimization - An introduction to mathematical modelling and numerical simulation*. Oxford University Press, Oxford, UK.
- Allaire, S. E., S. Roulier, and A. J. Cessna. 2009. Quantifying preferential flow in soils: A review of different techniques. *J. Hydrol.* 378 (1-2): 179–204.
- Allen, L. H., E. Matijević, and L. Meites. 1971. Exchange of Na⁺ for the silanolic protons of silica. *J. Inorg. Nucl. Chem.* 33 (5): 1293–1299.
- Ander, P., K.-E. Eriksson, and H.-S. Yu. 1984. Metabolism of lignin-derived aromatic acids by wood-rotting fungi. *Microbiology* 130 (1): 63–68.
- Angle, J. T., M. L. Brusseau, W. L. Miller, and J. J. Delfino. 1992. Nonequilibrium sorption and aerobic biodegradation of dissolved alkylbenzenes during transport in aquifer material: column experiments and evaluation of a coupled-process model. *Environ. Sci. Technol.* 26 (7): 1404–1410.
- Aris, R. 1956. On the dispersion of a solute in a fluid flowing through a tube. *Proc. Roy. Soc.* 235 (1200): 67–77.
- Bach, E. M., and K. S. Hofmockel. 2014. Soil aggregate isolation method affects measures of intra-aggregate extracellular enzyme activity. *Soil Biol. Biochem.* 69: 54–62.
- Bahr, J. M., and J. Rubin. 1987. Direct comparison of kinetic and local equilibrium formulations for solute transport affected by surface reactions. *Water Resour. Res.* 23 (3): 438–452.
- Barry, D. A., J.-Y. Parlange, L. Li, H. Prommer, C. J. Cunningham, and F. Stagnitti. 2000. Analytical approximations for real values of the lambert w-function. *Math. Comp. Sim.* 53 (1-2): 95–103.
- Bartelmann, M., B. Feuerbacher, T. Krüger, D. Lüst, A. Rebhan, and A. Wipf. 2015. *Theoretische Physik*. Springer, Berlin, Germany.
- Baumann, T., and C. J. Werth. 2004. Visualization and modeling of polystyrol colloid transport in a silicon micromodel. *Vadose Zone J.* 3 (2): 434–443.
- Baveye, P. C. 2015. Grand challenges in the research on soil processes. *Front. Environ. Sci.* 3 (10).
- Bear, J. 1988. *Dynamics of fluids in porous media*. Dover Publications, New York, USA.
- Beatty, S. M., and J. E. Smith. 2013. Dynamic soil water repellency and infiltration in post-wildfire soils. *Geoderma* 192: 160–172.

- Beriro, D. J., C. H. Vane, M. R. Cave, and C. P. Nathanail. 2014. Effects of drying and comminution type on the quantification of polycyclic aromatic hydrocarbons (PAH) in a homogenised gasworks soil and the implications for human health risk assessment. *Chemosphere* 111: 396–404.
- Beulke, S., C. D. Brown, C. J. Fryer, and W. van Beinum. 2004. Influence of kinetic sorption and diffusion on pesticide movement through aggregated soils. *Chemosphere* 57 (6): 481–490.
- Blum, W. E. 2005. Functions of soil for society and the environment. *Rev. Environ. Sci. Biotechnol.* 4 (3): 75–79.
- Bottner, P. 1985. Response of microbial biomass to alternate moist and dry conditions in a soil incubated with ¹⁴C- and ¹⁵N-labelled plant material. *Soil Biol. Biochem.* 17 (3): 329–337.
- Box, G. E. P., and M. E. Muller. 1958. A note on the generation of random normal deviates. *Ann. Math. Statist.* 29 (2): 610–611.
- Bradford, S. A., J. Simunek, M. Bettahar, M. T. van Genuchten, and S. R. Yates. 2003. Modeling colloid attachment, straining, and exclusion in saturated porous media. *Environ. Sci. Technol.* 37 (10): 2242–2250.
- Bradford, S. A., and S. Torkzaban. 2008. Colloid transport and retention in unsaturated porous media: A review of interface-, collector-, and pore-scale processes and models. *Vadose Zone J.* 7 (2): 667–681.
- Bromly, M., C. Hinz, and L. A. G. Aylmore. 2007. Relation of dispersivity to properties of homogeneous saturated repacked soil columns. *Eur. J. Soil Sci.* 58 (1): 293–301.
- Brooks, R. H., and A. T. Corey. 1964. Hydraulic properties of porous media and their relation to drainage design. *Transact. ASAE* 7 (1): 26–0028.
- Brown, R. 1828. XXVII. A brief account of microscopical observations made in the months of June, July and August 1827, on the particles contained in the pollen of plants; and on the general existence of active molecules in organic and inorganic bodies. *Phil. Mag.* 2 4 (21): 161–173.
- Brunauer, S., P. Emmett, and E. Teller. 1938. Adsorption of gases in multimolecular layers. *J. Am. Chem. Soc.* 60 (2): 309–319.
- Brusseau, M. L., and P. S. C. Rao. 1990. Modeling solute transport in structured soils: A review. *Geoderma* 46 (1-3): 169–192.
- Brusseau, M. L. 1992. Nonequilibrium transport of organic chemicals: The impact of pore-water velocity. *J. Contam. Hydrol.* 9 (4): 353–368.
- Brusseau, M. L., R. E. Jessup, and P. S. C. Rao. 1991. Nonequilibrium sorption of organic chemicals: Elucidation of rate-limiting processes. *Environ. Sci. Technol.* 25 (1): 134–142.
- Brusseau, M. L., P. S. C. Rao, and R. W. Gillham. 1989. Sorption nonideality during organic contaminant transport in porous media. *Crit. Rev. Environ. Contr.* 19 (1): 33–99.
- Butcher, J. C. 2008. *Numerical methods for ordinary differential equations*. 2nd. John Wiley & Sons, Ltd, Chichester, UK.

- Camesano, T. A., and B. E. Logan. 1998. Influence of fluid velocity and cell concentration on the transport of motile and nonmotile bacteria in porous media. *Environ. Sci. Technol.* 32 (11): 1699–1708.
- Cheyns, K., J. Mertens, J. Diels, E. Smolders, and D. Springael. 2010. Monod kinetics rather than a first-order degradation model explains atrazine fate in soil mini-columns: Implications for pesticide fate modelling. *Environ. Pollut.* 158 (5): 1405–1411.
- Coats, K. H., and B. D. Smith. 1964. Dead-end pore volume and dispersion in porous media. *Soc. Pet. Eng. J.* 4 (1): 73–84.
- Corapcioglu, M. Y., and A. Haridas. 1984. Transport and fate of microorganisms in porous media: A theoretical investigation. *J. Hydrol.* 72 (1-2): 149–169.
- Cornell, R. M., and U. Schwertmann. 2003. *The Iron Oxides. Structure, Properties, Reactions, Occurrences and Uses.* Wiley-VCH, Weinheim, Germany.
- Crank, J., and P. Nicolson. 1996. A practical method for numerical evaluation of solutions of partial differential equations of the heat-conduction type. *Adv. Comp. Math.* 6 (1): 207–226.
- Daly, E., and A. Porporato. 2005. A review of soil moisture dynamics: From rainfall infiltration to ecosystem response. *Environ. Eng. Sci.* 22: 9–24.
- Damköhler, G. 1936. Einflüsse der Strömung, Diffusion und des Wärmeüberganges auf die Leistung von Reaktionsöfen.: I. Allgemeine Gesichtspunkte für die Übertragung eines chemischen Prozesses aus dem Kleinen ins Große. *Z. Elektrochem. ang. phys. Chem.* 42 (12): 846–862.
- Darcy, H. 1856. *Les Fontaines Publiques de la Ville de Dijon.* Dalmont, Paris, France.
- Das, B. S., L. S. Lee, P. S. C. Rao, and R. P. Hultgren. 2004. Sorption and degradation of steroid hormones in soils during transport - Column studies and model evaluation. *Environ. Sci. Technol.* 38 (5): 1460–1470.
- Dawson, G., S. Lee, and A. Juel. 2013. The trapping and release of bubbles from a linear pore. *J. Fluid Mech.* 722: 437–460.
- de Smedt, F., and P. J. Wierenga. 1979. Mass transfer in porous media with immobile water. *J. Hydrol.* 41 (1-2): 59–67.
- de Wilde, T., J. Mertens, P. Spanoghe, J. Ryckeboer, P. Jaeken, and D. Springael. 2008. Sorption kinetics and its effects on retention and leaching. *Chemosphere* 72 (3): 509–516.
- Deans, H. A. 1963. A mathematical model for dispersion in the direction of flow in porous media. *Soc. Pet. Eng. J.* 3 (1): 49–52.
- Dekker, L. W., S. H. Doerr, K. Oostindie, A. K. Ziogas, and C. J. Ritsema. 2001. Water repellency and critical soil water content in a dune sand. *Soil Sci. Soc. Am. J.* 65: 1667–1674.
- Duhamel, P., and M. Vetterli. 1990. Fast fourier transforms: A tutorial review and a state of the art. *Signal Proc.* 19 (4): 259–299.
- Dutt, A., and V. Rokhlin. 1993. Fast fourier transforms for nonequispaced data. *SIAM J. Sci. Comp.* 14 (6): 1368–1393.
- Dzombak, D. A., and F. M. Morel. 1990. *Surface complexation modeling: Hydrous ferric oxide.* John Wiley & Sons, New York, USA.

- Einstein, A. 1905. Über die von der molekularkinetischen Theorie der Wärme geforderte Bewegung von in ruhenden Flüssigkeiten suspendierten Teilchen. *Ann. Phys.* 322 (8): 549–560.
- Ellsworth, T. R., P. J. Shaouse, J. Jobes, J. Fargerlund, and T. H. Skaggs. 1996. Solute transport in unsaturated soil: Experimental design, parameter estimation, and model discrimination. *Soil Sci. Soc. Am. J.* 60 (3): 397–407.
- Evanko, C. R., and D. A. Dzombak. 1999. Surface complexation modeling of organic acid sorption to goethite. *J. Coll. Interf. Sci.* 214 (2): 189–206.
- Faybishenko, B. A. 1995. Hydraulic behavior of quasi-saturated soils in the presence of entrapped air: laboratory experiments. *Water Resour. Res.* 31 (10): 2421–2435.
- Fesch, C., W. Simon, S. B. Haderlein, P. Reichert, and R. P. Schwarzenbach. 1998. Nonlinear sorption and nonequilibrium solute transport in aggregated porous media: Experiments, process identification and modeling. *J. Contam. Hydrol.* 31 (3-4): 373–407.
- Fick, A. 1855. Über Diffusion. *Ann. Phys.* 170 (1): 59–86.
- Filius, J. D., T. Hiemstra, and W. H. V. Riemsdijk. 1997. Adsorption of small weak organic acids on goethite: Modeling of mechanisms. *J. Coll. Interf. Sci.* 195 (2): 368–380.
- Floudas, C., and C. Gounaris. 2009. A review of recent advances in global optimization. *J. Glob. Optim.* 45 (1): 3–38.
- Flury, M., H. Flübler, W. A. Jury, and J. Leuenberger. 1994. Susceptibility of soils to preferential flow of water: A field study. *Water Resour. Res.* 30 (7): 1945–1954.
- Franssen, H. H., A. Alcolea, M. Riva, M. Bakr, N. van der Wiel, F. Stauffer, and A. Guadagnini. 2009. A comparison of seven methods for the inverse modelling of ground-water flow. Application to the characterisation of well catchments. *Adv. Water Resour.* 32 (6): 851–872.
- Freundlich, H. 1907. Über die Adsorption in Lösungen. *Z. phys. Chem. A* 54: 385–457.
- Gidas, B. 1985. Nonstationary Markov chains and convergence of the annealing algorithm. *J. Stat. Phys.* 39 (1): 73–131.
- Giddings, J. C. 1963. Kinetic origin of tailing in chromatography. *Anal. Chem.* 35 (13): 1999–2002.
- Gilbert, W., and W. Nicholson. 2004. *Modern Algebra with Applications*. Pure and Applied Mathematics: A Wiley Series of Texts, Monographs and Tracts. John Wiley & Sons, Ltd, Chichester, UK.
- Giles, C. H., A. P. D’Silva, and I. A. Easton. 1974. A general treatment and classification of the solute adsorption isotherm part. II. Experimental interpretation. *J. Coll. Interf. Sci.* 47 (3): 766–778.
- Giles, C. H., D. Smith, and A. Huitson. 1974. A general treatment and classification of the solute adsorption isotherm. I. Theoretical. *J. Coll. Interf. Sci.* 47 (3): 755–765.
- Ginn, T. R., B. D. Wood, K. E. Nelson, T. D. Scheibe, E. M. Murphy, and T. P. Clement. 2002. Processes in microbial transport in the natural subsurface. *Adv. Water Resour.* 25: 1017–1042.
- Granville, V., M. Krivanek, and J.-P. Rasson. 1994. Simulated annealing: A proof of convergence. *IEEE Trans. Patt. Anal. Mach. Intell.* 16 (6): 652–656.

- Grolimund, D., M. Borkovec, P. Federer, and H. Sticher. 1995. Measurement of sorption isotherms with flow-through reactors. *Environ. Sci. Technol.* 29 (9): 2317–2321.
- Grolimund, D., M. Elimelech, M. Borkovec, K. Barmettler, R. Kretzschmar, and H. Sticher. 1998. Transport of in situ mobilized colloidal particles in packed soil columns. *Environ. Sci. Technol.* 32 (22): 3562–3569.
- Gutierrez, M., and H. R. Fuentes. 1993. Modeling adsorption in multicomponent systems using a Freundlich-type isotherm. *J. Contam. Hydrol.* 14 (3-4): 247–260.
- Harter, R. D., and D. E. Baker. 1977. Applications and misapplications of the Langmuir equation to soil adsorption phenomena. *Soil Sci. Soc. Am. J.* 41 (6): 1077–1080.
- Hashimoto, I., K. B. Deshpande, and H. C. Thomas. 1964. Peclet numbers and retardation factors for ion exchange columns. *Ind. Eng. Chem. Fundament.* 3 (3): 213–218.
- Hastings, W. K. 1970. Monte Carlo sampling methods using Markov chains and their applications. *Biometr.* 57 (1): 97–109.
- Hendrickx, J. M., and M. Flury. 2001. Uniform and preferential flow mechanisms in the vadose zone. In *Conceptual models of flow and transport in the fractured vadose zone*, 149–187. National Academic Press, Washington, DC, USA.
- Hiemstra, T., and W. H. V. Riemsdijk. 1999. Surface structural ion adsorption modeling of competitive binding of oxyanions by metal (hydr)oxides. *J. Coll. Interf. Sci.* 210 (1): 182–193.
- Hingston, F. J., A. M. Posner, and J. P. Quirk. 1972. Anion adsorption by goethite and gibbsite. *J. Soil Sci.* 23 (2): 177–192.
- Hinz, C. 2001. Description of sorption data with isotherm equations. *Geoderma* 99 (3-4): 225–243.
- Hofman, J., I. Hovorková, and K. T. Semple. 2014. The variability of standard artificial soils: Behaviour, extractability and bioavailability of organic pollutants. *J. Hazard. Mater.* 264: 514–520.
- Hogarth, W., B. Noye, J. Stagnitti, J. Parlange, and G. Bolt. 1990. A comparative study of finite difference methods for solving the one-dimensional transport equation with an initial-boundary value discontinuity. *Comp. Math. Appl.* 20 (11): 67–82.
- Holocher, J., F. Peeters, W. Aeschbach-Hertig, M. Hofer, M. Brennwald, W. Kinzelbach, and R. Kipfer. 2002. Experimental investigations on the formation of excess air in quasi-saturated porous media. *Geochim. Cosmochim. Acta* 66 (23): 4103–4117.
- Horn, R., H. Taubner, M. Wuttke, and T. Baumgartl. 1994. Soil physical properties related to soil structure. *Soil Till. Res.* 30 (2-4): 187–216.
- Horton, R. E. 1933. The role of infiltration in the hydrologic cycle. *Eos, Transact. Am. Geophys. Union* 14 (1): 446–460.
- Hougen, O. A., and W. R. Marshall. 1947. Adsorption from a fluid stream flow through a stationary granular bed. *Chem. Eng. Prog.* 43 (4): 197.
- Hu, Q., and M. L. Brusseau. 1994. The effect of solute size on diffusive-dispersive transport in porous media. *J. Hydrol.* 158 (3-4): 305–317.

- Huang, K., N. Toride, and M. T. Genuchten. 1995. Experimental investigation of solute transport in large, homogeneous and heterogeneous, saturated soil columns. *Transport Porous Med.* 18 (3): 283–302.
- Hubbard, S. S., J. Chen, J. Peterson, E. L. Majer, K. H. Williams, D. J. Swift, B. Mailloux, and Y. Rubin. 2001. Hydrogeological characterization of the south oyster bacterial transport site using geophysical data. *Water Resour. Res.* 37 (10): 2431–2456.
- Jaesche, P., K. U. Totsche, and I. Kögel-Knabner. 2006. Transport and anaerobic biodegradation of propylene glycol in gravel-rich soil materials. *J. Contam. Hydrol.* 85 (3-4): 271–286.
- Jury, W. A., and K. Roth. 1990. *Transfer functions and solute movement through soil: Theory and applications.* Birkhäuser, Basel, Switzerland.
- Kaiser, M., M. Kleber, and A. A. Berhe. 2015. How air-drying and rewetting modify soil organic matter characteristics: An assessment to improve data interpretation and inference. *Soil Biol. Biochem.* 80: 324–340.
- Kalkan, E. 2011. Impact of wetting-drying cycles on swelling behavior of clayey soils modified by silica fume. *Appl. Clay Sci.* 52 (4): 345–352.
- Kaluarachchi, J. J., and J. C. Parker. 1987. Effects of hysteresis with air entrapment on water flow in the unsaturated zone. *Water Resour. Res.* 23 (10): 1967–1976.
- Kamra, S., and B. Lennartz. 2005. Quantitative indices to characterize the extent of preferential flow in soils. *Environ. Modell. Software* 20 (7): 903–915.
- Kasteel, R., H.-J. Vogel, and K. Roth. 2000. From local hydraulic properties to effective transport in soil. *Eur. J. Soil Sci.* 51 (1): 81–91.
- Keesstra, S., V. Geissen, K. Mosse, S. Piirainen, E. Scudiero, M. Leistra, and L. van Schaik. 2012. Soil as a filter for groundwater quality. *Curr. Opinion Environ. Sustain.* 4 (5): 507–516.
- Khan, A. U.-H., and W. A. Jury. 1990. A laboratory study of the dispersion scale effect in column outflow experiments. *J. Contam. Hydrol.* 5 (2): 119–131.
- Kieft, T. L., E. soroker, and M. K. firestone. 1987. Microbial biomass response to a rapid increase in water potential when dry soil is wetted. *Soil Biol. Biochem.* 19 (2): 119–126.
- Kim, H., and H. Park. 2008. Nonnegative matrix factorization based on alternating nonnegativity constrained least squares and active set method. *SIAM J. Matrix Anal. Appl.* 30 (2): 713–730.
- Knabner, P., K. U. Totsche, and I. Kögel-Knabner. 1996. The modeling of reactive solute transport with sorption to mobile and immobile sorbents - Part I: Experimental evidence and model development. *Water Resour. Res.* 32 (6): 1611–1622.
- Knappenberger, T., M. Flury, E. D. Mattson, and J. B. Harsh. 2014. Does water content or flow rate control colloid transport in unsaturated porous media? *Environ. Sci. Technol.* 48 (7): 3791–3799.
- Koch, S., and H. Flühler. 1993. Non-reactive solute transport with micropore diffusion in aggregated porous media determined by a flow-interruption method. *J. Contam. Hydrol.* 14 (1): 39–54.

- Koestel, J. K., J. Moeys, and N. J. Jarvis. 2011. Evaluation of nonparametric shape measures for solute breakthrough curves. *Vadose Zone J.* 10 (4): 1261–1275.
- Kool, J. B., and J. C. Parker. 1987. Development and evaluation of closed-form expressions for hysteretic soil hydraulic properties. *Water Resour. Res.* 23 (1): 105–114.
- Kool, J., J. Parker, and M. van Genuchten. 1987. Parameter estimation for unsaturated flow and transport models - A review. *J. Hydrol.* 91 (3): 255–293.
- Koopmans, G. F., and J. E. Groenenberg. 2011. Effects of soil oven-drying on concentrations and speciation of trace metals and dissolved organic matter in soil solution extracts of sandy soils. *Geoderma* 161 (3-4): 147–158.
- Kosmulski, M. 2011. The pH-dependent surface charging and points of zero charge: V. Update. *J. Coll. Interf. Sci.* 353 (1): 1–15.
- Kosmulski, M. 2014. The pH dependent surface charging and points of zero charge. VI. Update. *J. Coll. Interf. Sci.* 426: 209–212.
- Kothawala, D., T. Moore, and W. Hendershot. 2008. Adsorption of dissolved organic carbon to mineral soils: A comparison of four isotherm approaches. *Geoderma* 148 (1): 43–50.
- Langmuir, I. 1916. The constitution and fundamental properties of solids and liquids. Part I. Solids. *J. Am. Chem. Soc.* 38 (11): 2221–2295.
- Lapidus, L., and N. R. Amundson. 1952. Mathematics of adsorption in beds. VI. The effect of longitudinal diffusion in ion exchange and chromatographic columns. *J. Phys. Chem.* 56 (8): 984–988.
- Leibundgut, C., P. Maloszewski, and C. Külls. 2009. *Tracers in hydrogeology*. John Wiley & Sons Ltd., New York, USA.
- Levenberg, K. 1944. A method for the solution of certain non-linear problems in least squares. *Quart. J. Appl. Math.* 2: 164–168.
- Lewis, J., and J. Sjöström. 2010. Optimizing the experimental design of soil columns in saturated and unsaturated transport experiments. *J. Contam. Hydrol.* 115 (1-4): 1–13.
- Li, Y., G. Flores, J. Xu, W.-Z. Yue, Y.-X. Wang, T.-G. Luan, and Q.-B. Gu. 2013. Residual air saturation changes during consecutive drainage-imbibition cycles in an air-water fine sandy medium. *J. Hydrol.* 503: 77–88.
- Li, Y., P. Wu, Z. Xia, Q. Yang, G. Flores, H. Jiang, M. Kamon, and B. Yu. 2014. Changes in residual air saturation after thorough drainage processes in an air-water fine sandy medium. *J. Hydrol.* 519, Part A: 271–283.
- Lide, D. R., ed. 2009. *CRC handbook of chemistry and physics*. 90th edition. CRC Press, Boca Raton, USA.
- Limousin, G., J.-P. Gaudet, L. Charlet, S. Szenknect, V. Barthès, and M. Krimissa. 2007. Sorption isotherms: A review on physical bases, modeling and measurement. *Appl. Geochem.* 22 (2): 249–275.
- Lindstrom, F. T., and L. Boermsma. 1973. A theory on the mass transport of previously distributed chemicals in a water-saturated sorbing porous medium: III. Exact solution for first-order kinetic sorption. *Soil Sci.* 115 (1): 5–10.
- Liu, H., T. Chen, and R. L. Frost. 2014. An overview of the role of goethite surfaces in the environment. *Chemosphere* 103: 1–11.

- Majdalani, S., E. Michel, L. Di-Pietro, and R. Angulo-Jaramillo. 2008. Effects of wetting and drying cycles on in situ soil particle mobilization. *Eur. J. Soil Sci.* 59 (2): 147–155.
- Marquardt, D. W. 1963. An algorithm for least-squares estimation of nonlinear parameters. *J. Soc. Ind. Appl. Math.* 11 (2): 431–441.
- McKenzie, R. M. 1980. The adsorption of lead and other heavy metals on oxides of manganese and iron. *Aust. J. Soil Res.* 18 (1).
- McKinley, J. P., and E. A. Jenne. 1991. Experimental investigation and review of the "solids concentration" effect in adsorption studies. *Environ. Sci. Technol.* 25 (12): 2082–2087.
- Metropolis, N., A. W. Rosenbluth, M. N. Rosenbluth, A. H. Teller, and E. Teller. 1953. Equation of state calculations by fast computing machines. *J. Chem. Phys.* 21 (6): 1087–1092.
- Metropolis, N., and S. M. Ulam. 1949. The Monte Carlo method. *J. Am. Stat. Assoc.* 44 (247): 335–341.
- Molz, F. J., M. A. Widdowson, and L. D. Benefield. 1986. Simulation of microbial growth dynamics coupled to nutrient and oxygen transport in porous media. *Water Resour. Res.* 22 (8): 1207–1216.
- Murphy, B. W. 2014. *Soil organic matter and soil function - Review of the literature and underlying data*. Australian Department of the Environment, Canberra, Australia.
- Nannipieri, P., J. Ascher, M. T. Ceccherini, L. Landi, G. Pietramellara, and G. Renella. 2003. Microbial diversity and soil functions. *Eur. J. Soil Sci.* 54 (4): 655–670.
- Nielsen, D. R., M. Th. Van Genuchten, and J. W. Biggar. 1986. Water flow and solute transport processes in the unsaturated zone. *Water Resour. Res.* 22 (9S): 89S–108S.
- Noye, J. 1987. Finite difference methods for solving the one-dimensional transport equation. In *Numerical modelling: applications to marine systems*, ed. by J. Noye, 145:231–256. North-Holland Publishing Company, Amsterdam, Netherlands.
- Noye, J. 1987. Numerical methods for solving the transport equation. In *Numerical modelling: applications to marine systems*, ed. by J. Noye, 145:195–229. North-Holland Publishing Company, Amsterdam, Netherlands.
- Olsen, P. A., A. Binley, S. Henry-Poulter, and W. Tych. 1999. Characterizing solute transport in undisturbed soil cores using electrical and X-ray tomographic methods. *Hydrol. Proc.* 13 (2): 211–221.
- Ouyang, Y., and X. Li. 2013. Recent research progress on soil microbial responses to drying-rewetting cycles. *Acta Ecol. Sinica* 33 (1): 1–6.
- Paatero, P., and U. Tapper. 1994. Positive matrix factorization: A non-negative factor model with optimal utilization of error estimates of data values. *Environmetr.* 5 (2): 111–126.
- Parfitt, R. 1979. Anion adsorption by soils and soil materials, ed. by N. Brady, 30:1–50. *Advances in Agronomy*. Academic Press, Amsterdam, Netherlands.
- Parker, J. C., and R. J. Lenhard. 1987. A model for hysteretic constitutive relations governing multiphase flow: 1. Saturation-pressure relations. *Water Resour. Res.* 23 (12): 2187–2196.

- Péclet, J. C. E. 1830. *Über die Wärme und deren Verwendung in den Künsten und Gewerben: ein vollständiges und nöthiges Handbuch für Physiker, Technologen, Fabrikanten, Mechaniker, Architekten, Forst- und Hüttenmänner*. Ed. by C. F. A. Hartmann. Vieweg, Braunschweig.
- Peng, X., R. Horn, and P. Hallett. 2015. Soil structure and its functions in ecosystems: Phase matter & scale matter. *Soil Till. Res.* 146, Part A: 1–3.
- Persson, L., and L. Bergström. 1991. Drilling method for collection of undisturbed soil monoliths. *Soil Sci. Soc. Am. J.* 55 (1): 285–287.
- Porro, I., P. J. Wierenga, and R. G. Hills. 1993. Solute transport through large uniform and layered soil columns. *Water Resour. Res.* 29 (4): 1321–1330.
- Porro, I., M. E. Newman, and F. M. Dunnivant. 2000. Comparison of batch and column methods for determining strontium distribution coefficients for unsaturated transport in basalt. *Environ. Sci. Technol.* 34 (9): 1679–1686.
- Press, W. H., S. A. Teukolsky, W. T. Vetterling, and B. P. Flannery. 2007. *Numerical recipes 3rd edition: The art of scientific computing*. 3rd ed. Cambridge University Press, New York, USA.
- Pronk, G. J., K. Heister, G.-C. Ding, K. Smalla, and I. Kögel-Knabner. 2012. Development of biogeochemical interfaces in an artificial soil incubation experiment; Aggregation and formation of organo-mineral associations. *Geoderma* 189-190: 585–594.
- Radcliffe, D., and J. Šimůnek. 2010. *Soil physics with HYDRUS: Modeling and applications*. CRC Press, Taylor / Francis Group, Boca Raton, USA.
- Rehmann, L. C., C. Welty, and R. Harvey. 1999. Stochastic analysis of virus transport in aquifers. *Water Resour. Res.* 35 (7): 1987–2006.
- Richards, L. A. 1931. Capillary conduction of liquids through porous mediums. *J. Appl. Phys.* 1 (5): 318–333.
- Ritschel, T. 2011. Parametrisierung der Sorption (Ausmaß, Typ, Geschwindigkeit) eines ausgewählten Modellsorbat-Sorbenten-Systems mittels Kreislauf-Durchbruch-Experimenten. Master's Thesis, Friedrich Schiller Universität Jena.
- Ritschel, T., and K. U. Totsche. 2016. Closed-flow column experiments: A numerical sensitivity analysis of solute adsorption and parameter uncertainty. *Water Resour. Res.* 52 (8): 6094–6110.
- Ritschel, T., and K. U. Totsche. 2016. Closed-flow column experiments—Insights into solute transport provided by a damped oscillating breakthrough behavior. *Water Resour. Res.* 52 (3): 2206–2221.
- Ruiz-Dueñas, F. J., and Á. T. Martínez. 2009. Microbial degradation of lignin: How a bulky recalcitrant polymer is efficiently recycled in nature and how we can take advantage of this. *Microb. Biotechnol.* 2 (2): 164–177.
- Saad, Y. 2000. *Iterative methods for sparse linear systems*. SIAM Society for Industrial & Applied Mathematics, Philadelphia, USA.
- Samouëlian, A., H.-J. Vogel, and O. Ippisch. 2007. Upscaling hydraulic conductivity based on the topology of the sub-scale structure. *Adv. Water Resour.* 30 (5): 1179–1189.

- Sardin, M., D. Schweich, F. J. Leij, and M. T. van Genuchten. 1991. Modelling the nonequilibrium transport of linearly interacting solutes in porous media: A review. *Water Resour. Res.* 27 (9): 2287–2307.
- Saygin, S. D., W. M. Cornelis, G. Erpul, and D. Gabriels. 2012. Comparison of different aggregate stability approaches for loamy sand soils. *Appl. Soil Ecol.* 54: 1–6.
- Schaffer, M., and T. Licha. 2015. A framework for assessing the retardation of organic molecules in groundwater: implications of the species distribution for the sorption-influenced transport. *Sci. Total Environ.* 524-525: 187–194.
- Schmidt, R. 2010. Optimierung von Kreislauf-Säulen-Experimenten zum Studium der Sorption organischer Modellsorbate an mineralischen Oberflächen. Diploma Thesis, Friedrich Schiller Universität Jena.
- Schweich, D., and M. Sardin. 1981. Adsorption, partition, ion exchange and chemical reaction in batch reactors or in columns - A review. *J. Hydrol.* 50: 1–33.
- Šimůnek, J., M. Šejna, H. Saito, M. Sakai, and M. T. van Genuchten. 2013. *The Hydrus-1D software package for simulating the movement of water, heat, and multiple solutes in variably saturated media*. Version 4.16, HYDRUS Software Series 3. 340. Department of Environmental Sciences, University of California Riverside, Riverside, California, USA.
- Šimůnek, J., N. J. Jarvis, M. T. van Genuchten, and A. Gärdenäs. 2003. Review and comparison of models for describing non-equilibrium and preferential flow and transport in the vadose zone. *J. Hydrol.* 272 (1-4): 14–35.
- Smoluchowski, M. V. 1916. Über Brownsche Molekularbewegung unter Einwirkung äußerer Kräfte und deren Zusammenhang mit der verallgemeinerten Diffusionsgleichung. *Ann. Phys.* 353 (24): 1103–1112.
- Sposito, G. 1979. Derivation of the Langmuir equation for ion exchange reactions in soils. *Soil Sci. Soc. Am. J.* 43 (1): 197–198.
- Sposito, G. 1980. Derivation of the Freundlich equation for ion exchange reactions in soils. *Soil Sci. Soc. Am. J.* 44: 652–654.
- Sposito, G. 1987. Distinguishing adsorption from surface precipitation. In *Geochemical processes at mineral surfaces*, 217–228.
- Sullivan, L. A. 1990. Soil organic matter, air encapsulation and water-stable aggregation. *J. Soil Sci.* 41 (3): 529–534.
- Sweby, P. K. 1984. High resolution schemes using flux limiters for hyperbolic conservation laws. *SIAM J. Num. Anal.* 21 (5): 995–1011.
- Syngouna, V. I., and C. V. Chrysikopoulos. 2012. Transport of biocolloids in water saturated columns packed with sand: effect of grain size and pore water velocity. Sorption and Transport Processes Affecting the Fate of Environmental Pollutants in the Subsurface, *J. Contam. Hydrol.* 129-130: 11–24.
- Tadmor, E. 2012. A review of numerical methods for nonlinear partial differential equations. *Bulletin Am. Math. Soc.* 49 (4): 507–554.
- Tang, G., M. A. Mayes, J. C. Parker, X. L. Yin, D. B. Watson, and P. M. Jardine. 2009. Improving parameter estimation for column experiments by multi-model evaluation and comparison. *J. Hydrol.* 376 (3-4): 567–578.

- Taylor, G. 1953. Dispersion of soluble matter in solvent flowing slowly through a tube. *Proc. Roy. Soc.* 219 (1137): 186–203.
- ter Laak, T. L., A. Barendregt, and J. L. Hermens. 2007. Grinding and sieving soil affects the availability of organic contaminants: A kinetic analysis. *Chemosphere* 69 (4): 613–620.
- Thomson, B. C., N. J. Ostle, N. P. McNamara, A. S. Whiteley, and R. I. Griffiths. 2010. Effects of sieving, drying and rewetting upon soil bacterial community structure and respiration rates. *J. Microbiol. Methods* 83 (1): 69–73.
- Toride, N., F. J. Leij, and M. T. van Genuchten. 1993. A comprehensive set of analytical solutions for nonequilibrium solute transport with first-order decay and zero-order production. *Water Resour. Res.* 29 (7): 2167–2182.
- Totsche, K. U. 2001. *Reaktiver Stofftransport in Böden: Optimierte Experimentdesigns zur Prozessidentifikation*. 75th ed. Bayreuther Bodenkundliche Ber., Bayreuth, Germany.
- Totsche, K. U., P. Knabner, and I. Kögel-Knabner. 1996. The modeling of reactive solute transport with sorption to mobile and immobile sorbents - Part II: Model discussion and numerical simulation. *Water Resour. Res.* 32 (6): 1623–1634.
- Totsche, K. U., T. Rennert, M. H. Gerzabek, I. Kögel-Knabner, K. Smalla, M. Spiteller, and H.-J. Vogel. 2010. Biogeochemical interfaces in soil: The interdisciplinary challenge for soil science. *J. Plant Nutr. Soil Sci.* 173 (1): 88–99.
- Tufenkji, N. 2007. Modeling microbial transport in porous media: Traditional approaches and recent developments. *Adv. Water Resour.* 30 (6-7): 1455–1469.
- United Nations General Assembly. 2013. *Resolution 68/232. World Soil Day and International Year of Soils*.
- van Genuchten, M. T. 1980. A closed-form equation for predicting the hydraulic conductivity of unsaturated soils. *Soil Sci. Soc. Am. J.* 44 (5): 892–898.
- van Genuchten, M. T. 1981. Analytical solution for chemical transport with simultaneous adsorption, zero-order production and first-order decay. *J. Hydrol.* 49: 213–233.
- van Genuchten, M. T., J. M. Davidson, and P. J. Wierenga. 1974. An evaluation of kinetic and equilibrium equations for the prediction of pesticide movement through porous media. *Soil Sci. Soc. Am. J.* 38 (1): 29–35.
- van Genuchten, M. T., and R. J. Wagenet. 1989. Two-site/two-region models for pesticide transport and degradation: Theoretical development and analytical solutions. *Soil Sci. Soc. Am. J.* 53 (5): 1303–1310.
- van Genuchten, M. T., and P. J. Wierenga. 1976. Mass transfer studies in sorbing porous media I. Analytical solutions. *Soil Sci. Soc. Am. J.* 40 (4): 473–480.
- van Genuchten, M. T. 1981. *Non-equilibrium transport parameters from miscible displacement experiments*. United States Department of Agriculture, U.S. Salinity Laboratory, Riverside, California, USA.
- Vanderborght, J., and H. Vereecken. 2002. Estimation of local scale dispersion from local breakthrough curves during a tracer test in a heterogeneous aquifer: The Lagrangian approach. *J. Contam. Hydrol.* 54 (1-2): 141–171.
- Veith, J. A., and G. Sposito. 1977. On the use of the Langmuir equation in the interpretation of “Adsorption” phenomena. *Soil Sci. Soc. Am. J.* 41 (4): 697–702.

- Vereecken, H., U. Jaekel, and H. Schwarze. 2002. Analysis of the long-term behavior of solute transport with nonlinear equilibrium sorption using breakthrough curves and temporal moments. *J. Contam. Hydrol.* 56 (3-4): 271–294.
- Vereecken, H., J. Vanderborght, R. Kasteel, M. Spiteller, A. Schäffer, and M. Close. 2011. Do lab-derived distribution coefficient values of pesticides match distribution coefficient values determined from column and field-scale experiments? A critical analysis of relevant literature. *J. Environ. Qual.* 40 (3): 879–898.
- Vidal, M., M. J. Santos, T. Abrão, J. Rodríguez, and A. Rigol. 2009. Modeling competitive metal sorption in a mineral soil. *Geoderma* 149 (3-4): 189–198.
- Vogel, C., D. Babin, G. J. Pronk, K. Heister, K. Smalla, and I. Kögel-Knabner. 2014. Establishment of macro-aggregates and organic matter turnover by microbial communities in long-term incubated artificial soils. *Soil Biol. Biochem.* 79: 57–67.
- Vogelmann, E., J. Reichert, J. Prevedello, C. Consensa, A. É. Oliveira, G. Awe, and J. Mataix-Solera. 2013. Threshold water content beyond which hydrophobic soils become hydrophilic: The role of soil texture and organic matter content. *Geoderma* 209-210: 177–187.
- Voice, T. C., and W. J. Weber. 1985. Sorbent concentration effects in liquid/solid partitioning. *Environ. Sci. Technol.* 19 (9): 789–796.
- Wander, M. 2004. Soil organic matter in sustainable agriculture. Chap. Soil Organic Matter Fractions and Their Relevance to Soil Function, ed. by F. Magdoff and R. R. Weil, 68–90. CRC Press, Boca Raton, USA.
- Wang, T.-H., M.-H. Li, and S.-P. Teng. 2009. Bridging the gap between batch and column experiments: a case study of cs adsorption on granite. *J. Hazard. Mater.* 161 (1): 409–415.
- Wang, Z., J. Feyen, D. R. Nielsen, and M. T. van Genuchten. 1997. Two-phase flow infiltration equations accounting for air entrapment effects. *Water Resour. Res.* 33 (12): 2759–2767.
- Wehrer, M., and K. U. Totsche. 2005. Determination of effective release rates of polycyclic aromatic hydrocarbons and dissolved organic carbon by column outflow experiments. *Eur. J. Soil Sci.* 56 (6): 803–813.
- Wehrer, M., P. Jaesche, and K. U. Totsche. 2012. Modeling the kinetics of microbial degradation of deicing chemicals in porous media under flow conditions. *Environ. Pollut.* 168: 96–106.
- Wehrer, M., and L. D. Slater. 2015. Characterization of water content dynamics and tracer breakthrough by 3-D electrical resistivity tomography (ERT) under transient unsaturated conditions. *Water Resour. Res.* 51 (1): 97–124.
- Wehrer, M., and K. U. Totsche. 2003. Detection of non-equilibrium contaminant release in soil columns: Delineation of experimental conditions by numerical simulations. *J. Plant Nutr. Soil Sci.* 166 (4): 475–483.
- Wehrer, M., and K. U. Totsche. 2008. Effective rates of heavy metal release from alkaline wastes - Quantified by column outflow experiments and inverse simulations. *J. Contam. Hydrol.* 101 (1-4): 53–66.

- Weigand, H., K. U. Totsche, I. Kögel-Knabner, E. Annweiler, H. H. Richnow, and W. Michaelis. 2002. Fate of anthracene in contaminated soil transport and biochemical transformation under unsaturated flow conditions. *Eur. J. Soil Sci.* 53 (1): 71–81.
- Weisstein, E. 2015. Attractor. From MathWorld—A Wolfram Web Resource. Visited on 01/16/2015. <http://mathworld.wolfram.com/Attractor.html>.
- Whitaker, S. 1986. Flow in porous media I: A theoretical derivation of Darcy's law. *Transport Porous Med.* 1 (1): 3–25.
- Wierenga, P. J., and M. T. van Genuchten. 1989. Solute transport through small and large unsaturated soil columns. *Ground Wat.* 27 (1): 35–42.
- Winter, T. C., J. W. Harvey, O. L. Franke, and W. M. Alley. 1998. *Ground water and surface water. A single resource*. U.S. Geological Survey Circular. U.S. Geological Survey, Denver, USA.
- Wise, W. R. 1993. Effects of laboratory-scale variability upon batch and column determinations of nonlinearly sorptive behavior in porous media. *Water Resour. Res.* 29 (9): 2983–2992.
- Wu, C.-H., C.-Y. Kuo, C.-F. Lin, and S.-L. Lo. 2002. Modeling competitive adsorption of molybdate, sulfate, selenate, and selenite using a Freundlich-type multi-component isotherm. *Chemosphere* 47 (3): 283–292.
- Young, D. F., and W. P. Ball. 2000. Column experimental design requirements for estimating model parameters from temporal moments under nonequilibrium conditions. *Adv. Water Resour.* 23 (5): 449–460.
- Yu, M.-C., and S. Middleman. 1993. Air entrapment during liquid infiltration of porous media. *Chem. Eng. Communic.* 123 (1): 61–69.
- Zhou, H., J. J. Gómez-Hernández, and L. Li. 2014. Inverse methods in hydrogeology: Evolution and recent trends. *Adv. Water Resour.* 63: 22–37.

Acknowledgment

At first, I want to thank my supervisor Kai Uwe Totsche, who gave me the opportunity to dwell on the subject in a way that tremendously quickened my interest and creativity. Beneath providing a financially safe background, his ideas were always inspiring and motivating to an extent that made the enduring engagement into this topic possible in the first place.

I thank all people involved in instrumental analytics, especially Thomas Wach for the SEM imaging of the artificial soil components and Tom Guhra for his preliminary work on appropriate reactive tracers. I furthermore thank Anja Grawunder, Andreas Fritzsche and Matthias Händel for the numerous discussions on related and completely unrelated topics. I thank all the people at the Wöllnitzer Straße for the pleasant atmosphere in and around my office.

A thankful greeting goes to Markus Wehrer, who critically commented on a draft version of this thesis and thereby tremendously helped me in finalizing by providing another point of view to some aspects.

Special thanks go to the developers of PureBasic for the creation of the most comprehensive and easy-to-use, yet powerful, fast and reliable programming language I have ever come across. The vast modeling presented within this thesis would not have been possible without PureBasic and I probably would not have had such a delightful time with modeling.

As a fun evening recovers mental stamina, I thank all people that occasionally joined me for some drink.

I am deeply grateful to my family that allowed me to grow up in a way that raised my awareness to many aspects of nature and life and always supported me with the decisions I made.

And last, I thank Maria for everything.

Tabellarischer Lebenslauf

Persönliche Daten

Name: Thomas Ritschel
Geburtsdatum: 02.08.1984
Geburtsort: Neuhaus am Rennweg

Berufspraxis

2009 - 2011 Studentische Hilfskraft am Institut für Geowissenschaften
2011 - 2014 Wissenschaftlicher Mitarbeiter am Insitut für Geowissenschaften
Koordination des Joint Experiments "Hierarchical Structure of Biogeochemical Interfaces in Soil to Predict the Transport of Reactive Chemicals" im Rahmen des Schwerpunktprogramms 1315 der DFG
2014 - heute Wissenschaftlicher Mitarbeiter am Insitut für Geowissenschaften

Ausbildung

1995 - 2003 Besuch des staatlichen Gymnasiums Neuhaus am Rennweg
Abschluss: allgemeine Hochschulreife (Note: 1,2)
2003 - 2004 Wehrersatzdienst an der Gemeinde Lichte im Bereich Umwelt- und Landschaftspflege
2004 - 2006 Studium an der Friedrich-Schiller-Universität in Jena
Studiengang: Chemie Diplom (kein Abschluss)
2006 - 2009 Studium an der Friedrich-Schiller-Universität in Jena
Studiengang: Biogeowissenschaften Bachelor of Science (Note: 1,9)
2009 - 2011 Studium an der Friedrich-Schiller-Universität in Jena
Studiengang: Biogeowissenschaften Master of Science (Note: 1,4)

.....
Ort, Datum

.....
Thomas Ritschel

Selbstständigkeitserklärung

Ich erkläre, dass ich die vorliegende Arbeit selbstständig und unter Verwendung der angegebenen Hilfsmittel, persönlichen Mitteilungen und Quellen angefertigt habe.

.....
Ort, Datum

.....
Unterschrift des Verfassers